

Spring 2018

Understanding the Mechanical Behavior of Costal Cartilage at Their Curved Exterior Surface Via a Tactile Sensor with a Built-In Probe for Distributed-Deflection Detection

Jiayue Shen
Old Dominion University

Follow this and additional works at: https://digitalcommons.odu.edu/mae_etds

 Part of the [Biomechanical Engineering Commons](#), and the [Biomedical Engineering and Bioengineering Commons](#)

Recommended Citation

Shen, Jiayue. "Understanding the Mechanical Behavior of Costal Cartilage at Their Curved Exterior Surface Via a Tactile Sensor with a Built-In Probe for Distributed-Deflection Detection" (2018). Doctor of Philosophy (PhD), dissertation, Mechanical Engineering, Old Dominion University, DOI: 10.25777/6kpz-dt64
https://digitalcommons.odu.edu/mae_etds/34

This Dissertation is brought to you for free and open access by the Mechanical & Aerospace Engineering at ODU Digital Commons. It has been accepted for inclusion in Mechanical & Aerospace Engineering Theses & Dissertations by an authorized administrator of ODU Digital Commons. For more information, please contact digitalcommons@odu.edu.

UNDERSTANDING THE MECHANICAL BEHAVIOR OF COSTAL CARTILAGE AT
THEIR CURVED EXTERIOR SURFACE VIA A TACTILE SENSOR WITH A BUILT-IN
PROBE FOR DISTRIBUTED-DEFLECTION DETECTION

by

Jiayue Shen
B.S. July 2005, Zhejiang University, China
M.S. July 2009, Lanzhou University of Technology, China

A Dissertation Submitted to the Faculty of
Old Dominion University in Partial Fulfillment of the
Requirements for the Degree of

DOCTOR OF PHILOSOPHY

MECHANICAL ENGINEERING

OLD DOMINION UNIVERSITY

December 2017

Approved by:

Zhili Hao (Director)

Helmut Baumgart (Member)

Michael Stacey (Member)

Dipankar Ghosh (Member)

ABSTRACT

UNDERSTANDING THE MECHANICAL BEHAVIOR OF COSTAL CARTILAGE AT THEIR CURVED EXTERIOR SURFACE VIA A TACTILE SENSOR WITH A BUILT-IN PROBE FOR DISTRIBUTED-DEFLECTION DETECTION

Jiayue Shen
Old Dominion University, 2017
Director: Dr. Zhili Hao

This dissertation is aimed to determine the mechanical properties at the exterior surface of costal cartilages (CC) and examine how they vary with the cartilage length and the anatomical sites of CC in the ribcage via conformal indentation testing which is built upon a tactile sensor for distributed-deflection detection. The sensor entails a rectangular Polydimethylsiloxane (PDMS) microstructure sensing-plate integrated with a 5×1 transducer array with 0.75mm spatial resolution underneath and a built-in probe of 0.5mm \times 5mm \times 3mm above. By pressing the sensor against the exterior surface of a CC tissue with a pre-defined indentation pattern, the sensor conforms to the curved tissue surface via the built-in probe first, and then the mechanical properties of the tissue translate to the spatially distributed deflection in the sensor and register as resistance changes by the transducer array. As a load-bearing and non-stop deforming tissue from respiration, the mechanical properties of CC are critical for maintaining their structural health and delivering their function. CC have been used as a viable source of graft tissue for many autologous therapies and as a cell source for engineered articular cartilage (AC) due to its abundance and surgical accessibility. However, the mechanical properties of CC are not well understood yet. Chest wall deformities, such as Pectus Carinatum (PC), are known to arise from the disorder of CC, but their pathogenesis remains unknown and their surgical outcomes are unpredictable. The mechanical properties of the CC exterior surface influence diffusion of oxygen and nutrients and thus are intrinsic to maintaining their structural

characteristics. However, very limited knowledge exists on the mechanical properties of peripheral CC due to their highly irregular geometries. In this dissertation, a novel testing method, conformal indentation, was used to measure the mechanical properties at the CC curved exterior surface, where the structural integrity of CC is retained.

Conformal indentation was conducted at the anterior/posterior surfaces of whole porcine 5th -12th CC segments and the anterior/posterior surfaces and the superior/inferior borders of five human PC CC segments from the 7th ~10th ribs along the cartilage length to record their time-dependent response to a multi-step indentation-relaxation testing protocol. The instant indentation modulus and normalized relaxation of the CC segments were derived from the recorded data to quantify their elasticity and viscosity, respectively. The instant indentation modulus at the porcine CC and PC CC exterior surface are in the range of 130kPa ~500kPa and 98kPa~1173kPa, respectively, which are well below their counterpart at the CC transverse cross-sections. The normalized relaxation at the CC exterior surface is relatively high with low applied stress but becomes constant with high applied stress. The constant normalized relaxation at the porcine and PC CC exterior surfaces are in the range of 25%~40% and 5%~25%, respectively. The human CC have higher elasticity and lower viscosity than the porcine CC. Overall, the measured mechanical properties of CC vary with their anatomical sites and thus indicate the adaptation of CC to their local biomechanical environment in the ribcage.

Copyright, 2018, by Jiayue Shen, All Rights Reserved.

This dissertation is dedicated to my family, director, and research group.

ACKNOWLEDGMENTS

It has been a great experience to pursue my Ph.D. degree in the Department of Mechanical and Aerospace Engineering at Old Dominion University for the past five years. It was a tough long journey, and I could not make it through without the help and love from my advisor, mentors, family, colleagues, and friends.

First and foremost, I would like to thank my academic and research advisor, Dr. Zhili Hao, for her valuable guidance and encouragement. This work is made possible by her sagacious perception and profound knowledge. She is an extraordinary mentor and scientist. She is super kind and always available for questions. She encourages me to explore different things. She teaches me everything from work ethic, to critical thinking, to problem-solving. Without her guidance and persistent help, this dissertation would not have been possible.

I would also like to thank my research collaborator, Dr. Michael Stacey. During the past four years of collaboration, he provided a valuable guidance from a biological perspective towards my research. I appreciate these great research collaboration opportunities provided by Dr. Michael Stacey, which broadened my mind and shed light on my future career path. I would like to express my gratitude to Dr. Helmut Baumgart and Dr. Dipankar Ghosh for taking an interest in my work and serving on my Ph.D. dissertation committee. I learned what a scholar should be from these professors who I will always look up to.

I would like to express my appreciation to all the professors, classmates, and staff who have accompanied me during my Ph.D. study. They widened my horizon and impressed me with their profound knowledge and generosity in helping others. I want to thank my department and Old Dominion University, for providing an excellent and friendly study environment. I would

like to give my sincere gratitude to the department chair Dr. Sebastian Bawab GPD, Dr. Han Bao, Dr. Miltos Kotinis, and acting GPD Dr. Gene Hou. I also want to thank our program support staff, Ms. Diane Mitchell and Ms. June Blount, for always being elegant and patient. My thanks also go to my entire research group, Dr. Peng Cheng, Dr. Wenting Gu, Mr. Yichao Yang, Ms. Dan Wang and Mr. Siqin Dong for sharing thoughts and offering a friendly and stimulating atmosphere in research, and for providing me the training on COMSOL multiphysics simulation and sensor fabrication. I would also like to thank Dr. Steve C. Hsiung for his training on circuit design, and Mr. Xavier-Lewis Palmer for his assistance on sample preparation. Additionally, I also appreciate the porcine CC provider, Pendulum Fine Meats. I particularly want to thank the dedicated work of the butcher, so that I had plenty of fresh samples for experiments and supportive information for data explanation.

Last but not the least; I would like to express my gratitude to my family. I want to thank my husband and son for their enormous patience, full support, and for believing in me and cheering me up when I have doubts about myself. I want to thank my parents for indulging me in fulfilling my academic pursuit in a country far away from them, for respecting every decision I made for myself, and for giving me their unconditional love. I want also to thank my parents-in-law, for helping to take good care of my son and providing full support throughout the completion of my Ph. D degree. I also thank my spiritual mentors, Dr. James Yuan and Mrs. Nancy Yuan for treating me as a family member over all these years, making me feel at home and being an excellent model of a confident and successful professional scholar in the U.S. I also want to thank Mr. Yuming Geng, Dr. Kurnia Foe and Dr. Cheng Lin for always being there with me during my hard times. Most importantly, I would like to acknowledge the financial support

during my Ph.D. research provided by the National Science Foundation, CMMI, under Grant No. 1265785 and the teaching assistantship offered by Old Dominion University.

TABLE OF CONTENTS

	Page
LIST OF TABLES	XXI
LIST OF FIGURES	XIV
CHAPTER 1 INTRODUCTION.....	1
1.1. Biological Background.....	1
1.2. Experimental Studies of Costal Cartilage	6
1.3. Motivation	27
1.4. Objective	28
1.5. Dissertation Layout	29
CHAPTER 2 A POLYMER-BASED TACTILE SENSOR WITH A BUILT-IN PROBE FOR DISTRIBUTED-DEFLECTION DETECTION.....	30
2.1. Work Principle	30
2.2. Fabrication Process.....	34
2.3. Performance Characterization	38
2.4. Technical Issues Encountered	48
2.5. Discussion	52
2.6. Conclusion.....	53
CHAPTER 3 NUMERICAL AND EXPERIMENTAL STUDY ON A BUILT-IN PROBE ON THE TACTILE SENSOR FOR CURVED SURFACE.....	55
3.1. Configuration and Rationale	55
3.2. Theoretical Analysis.....	56
3.3. Performance Characterization	66
3.4. Conclusion.....	88

CHAPTER 4 MEASURED MECHANICAL PROPERTIES OF PORCINE

COSTAL CARTILAGE.....	91
4.1. Sample Preparation.....	91
4.2. Experiment Method.....	94
4.3. Data Analysis	95
4.4. Results	96
4.5. Discussion	102
4.6. Conclusions	107

CHAPTER 5 MEASURED MECHANICAL PROPERTIES OF HUMAN

PECTUS CARINATUM COSTAL CARTILAGE.....	109
5.1. Sample Preparation.....	109
5.2. Results	111
5.3. Discussion	117
5.4. Conclusions	120

CHAPTER 6 CONCLUSIONS AND RECOMMENDATIONS

6.1. Major Findings and Important Conclusions.....	122
6.2. Future Work	127

REFERENCES

REFERENCES	129
------------------	-----

APPENDICES

A LABVIEW PROGRAM FOR INSTRUMENT CONTROL AND DATA ACQUISITION.....	133
B MEASURED MECHANICAL PROPERTIES OF FIVE HUMAN PC CC SEGMENTS AT FOUR ANATOMICAL SITES OF ALL MEASURED LOCATIONS.....	137
VITA.....	145

LIST OF TABLES

Table	Page
2.1 Key design parameters of the polymer-based microfluidic tactile sensor.....	32
3.1 The key design parameters and their values of the sensor and the built-in probe for mechanical measurement of costal cartilage tissues.....	62
3.2 Material properties used in the simulation.....	75
3.3 Measured mechanical properties of CC #2 and CC #3.....	87
4.1 The geometrical parameters and their values of the whole porcine 5 th ~12 th CC.....	93
4.2 Summary of the measured average instant indentation modulus and average normalized relaxation (a) among the atomically sites and (b) along the cartilage length of the CC segments at their exterior surface.	101
4.3 Measured mechanical properties of porcine CC tissues reported in the literature.	104
5.1 Key dimensions of tested human PC costal cartilage segments.	111
5.2 Summary of the average instant indentation modulus and average normalized relaxation and their deviation (a) among the atomically sites and (b) along the cartilage length of the CC segments at their exterior surface	114
5.3 Comparison (a) among the atomically sites and (b) along the cartilage length of the CC segments at their exterior surface	117
5.4 Measured mechanical properties of human CC tissues reported in the literature.....	119
B.1 Summary of the measured instant indentation modulus and normalized relaxation modulus and their measurement errors along the length of the CC samples at their anterior/posterior surfaces, superior/inferior borders and the average of the four positions (a) CC #A (b) CC #B (c) CC #C (d) CC #D (e) CC #E.....	143

LIST OF FIGURES

Figure	Page
1.1 The structure of thoracic cage: (a) in porcine[12]; (b) in human [13].	2
1.2 Basic biomechanical environment of CC in the ribcage (a) along the cartilage length and (b) transverse cross-section	4
1.3 Illustration of the pectus bar passed behind the sternum before and after it is turned over. The insert shows the proper technique for fixation of the pectus bar against the lateral chest wall musculature.[20]	6
1.4 Schematic of confined compression testing apparatus[21]	9
1.5 Schematic of unconfined compression testing apparatus	9
1.6 (a) Dumbbell-shaped specimen used in a tensile test is extended at a constant rate while the load is measured. (b) Equilibrium and dynamic tensile testing. Force and displacement are normalized to cross-sectional area and gage length at 0% strain, respectively, to give stress and strain. The strength, or failure stress, and failure strain is obtained from the dynamic stress–strain data. The ramp modulus is calculated as the slope of the best-fit line between 25 and 75% of the maximum stress. The equilibrium tensile modulus can be obtained from the best-fit line between the three equilibrium data points.	11
1.7 Schematic of tension test apparatus [3]	12
1.8 Experimental setup for (a) three-point bend test [23] ; (b) four-point ben test[24].	15
1.9 Measuring arrangement of three-point bend flexure test for determination of bending properties in W. Grellmann’s group [22].	15
1.10 Depiction of three-point bend setup in Rani Roy’s paper [25]. Samples were tested in three-point bending where the thickness was measured for each sample. The samples were placed between two grips a distance, ranging from 0.5–1.0 cm apart. Deflections were applied and resultant loads were measured.	16
1.11 (a) Cross-section schematic of indentation testing using a sphere-ended tip r and a displacement-controlled protocol (b) Applied displacement or resultant load are illustrated[26].	17

Figure	Page
1.12 (a) A schematic illustration of CC cross section preparation. Multiple cross sections were cut in the cartilage between the sternum and rib bone, using a parallel-blade device such that each section was separated by a thin slice of discarded tissue. (b) A section of CC during the indentation test. Cartilage is held by a custom holder inside a Petri dish filled with 0.9% saline solution.	19
1.13 Pictures of indentation testing. (a) A cross-sectional CC specimen prepared and potted in fast-cast. (b) A specimen being subjected to an indentation test[27].	20
1.14 Schematic illustration of the CDI instrument used for experiments in JM Mattice's study [20].	21
1.15 Schematic illustration of the CC indentation testing procedure developed in M.L. Oyen's work[29]. CC is sectioned and cross-sections are indented in the cartilage mid-substance using a CDI instrument.	22
1.16 (a) Schematic of a nanoindenter system; (b) the indentation process P_{max} =maximum load, h_{max} =penetration depth, h_c =contact depth (the height of the contact between the tip and the sample); h_f =final depth; S = unloading stiffness. [30]	23
1.17 Schematic of a typical load-displacement curve. [30]	23
1.18 Sections of the CC. C_1 is closest to the costochondral joint and C_5 is the farthest. The modulus decreased from C_1 to C_5	25
1.19 Schematic of the experimental setup for nanoindentation of porcine CC [37].	26
2.1 Schematic of the experimental setup for nanoindentation of porcine costal cartilage.	31
2.2 Working principle of the tactile sensor.	32
2.3 Key design parameters of the polymer-based microfluidic tactile sensor: (a) top view; (b) side view.	32
2.4 Key dimensions of a rigid cylindrical probe for sensor characterization	34
2.5 Mask design for (a) the microchannel and (b) the patterned electrodes.	34
2.6 Fabrication process for patterning electrodes on Pyrex substrate: (a) Pyrex cleaning; (b) Photoresist spin coating; (c) UV light patterning with Mask 1; (d) Pyrex with patterned photoresist; (e) Photoresist development in MF-24; (f) Au/Cr deposition; (g) Succeed Au/Cr electrodes.	36

Figure	Page
2.7 Soft lithography on PDMS microstructure: (a) SU8 mold creation by microchannel shape mask; (b) PDMS microstructure formation; (c) PDMS microstructure detach; (d) Holes punching.....	37
2.8 Fabricated microfluidic tactile sensor with electrolyte in the microchannel. The transducers are labeled by numbers.	38
2.9 Experiment setup for sensor without a built-in probe characterization.	39
2.10 Key parameters for the patterns of indentation depth in sensor characterization.	41
2.11 Pictures of human PC CC#1 sample with measured locations (Black blocks and arrows on the cross sections of the samples indicate the locations of the probe in measurement; and left side: toward rib, right side: toward sternum.).....	42
2.12 Experiment setup for sensor performance on CC measurement.....	43
2.13 Force-deflection relation of the tactile sensor characterization with a rigid probe. Here, F means the force exerted on the polymer structure; k_s is the sensor stiffness; z_s is the top deflection of the tactile sensor. Measurement represents the three repeated indentation measurement.	47
2.14 Relation of average resistance change ΔR and average top deflection of the tactile sensor, z_s of three identical measurements. (1-5: sensor deflections at transducer 1-5). The standard deviation denotes to the robust feature of the tactile sensor.	47
2.15. The spatially distributed sensor deflection, z_s as a function of indentation depth z_{in} on CC #1 using the tactile sensor (solid line: instant values; dashed line: relaxed values) (a) anterior surface (b) posterior surface (1-5: sensor deflections at transducer 1-5).....	48
2.16. Schematic of the misalignment about the x-axis (x-z side view)	50
2.17. Schematic of the z-direction misalignment (y-z side view).....	50
2.18. Schematic of the x-y in-plane misalignment (x-y top view).....	51
2.19. Interaction between the tactile sensor and a CC tissue at its exterior surface (dashed line: before indentation; solid line: after indentation).....	52
3.1. Schematics of a tactile sensor with a built-in probe: (a) 3D configuration; (b) Top view with key dimensions.....	56

Figure	Page
3.2. Interaction between the tactile sensor with a built-in probe and a CC tissue at its exterior surface (dashed line: before indentation; solid line: after indentation).....	58
3.3. A tactile sensor with a built-in probe for measuring mechanical properties of a soft tissue with non-flat surface (drawn not to scale for clear illustration): (a) rationale (the transducers are color coded for clear illustration of resistance changes caused by sensor deflection), (b) three springs lumped-model and (c) two springs lumped-model (sensor with built-in probe is considered as one equilibrium spring)of PDMS microstructure, built-in probe and tissue region for the tissue-sensor interaction.	60
3.4. Three sets of design parameters involved in mechanical measurement of a costal cartilage tissue with curved surface (cartilage axial direction): i) Tissue parameters: tissue baseline thickness, h_t , tissue elasticity, E_t , and the highest thickness, δ_t , above the baseline thickness; ii) Sensor parameters: sensor stiffness, k_s , and sensor linear deflection range, $(0, z_{s_linear})$ (Solid line: before indentation depth; Dash line: after indentation depth); iii) Built-in probe parameters: probe elasticity, E_p , and probe thickness, h_p	63
3.5. Pictures of human PC costal cartilage samples with measured locations (a) CC #2 (b) CC #3 (Blue color on CC #2 and CC #3 came from the marker for marking locations; black blocks and arrows on the cross sections of the samples indicate the locations of the probe in measurement; and left side: toward rib, right side: toward sternum).	67
3.6. Experimental setup (a) schematic (b) the sensor with a built-in probe aligned on CC.	69
3.7. Performance characterization of the tactile sensor with a built-in probe: resistance changes, ΔR , of the five transducers (1~5) and overall reaction force, F , as a function of the sensor deflection, z_s	69
3.8. Conformal mechanical measurement of costal cartilage at its exterior surface using the tactile sensor with a built-in probe (a) definition of the deflection-depth slope (here, $\hat{z}' = \hat{z}'_{instant}$) (b) definition of parameters related to normalized relaxation.....	72
3.9. The z-displacement distributions of the tissue-sensor interaction in the indentation-relaxation test with a 0.64 mm indentation depth applied on the sensor bottom: (a) 3D view; (b) side view of x-z plane.....	75

Figure	Page
3.10. Simulation results of (a) the tissue strain at the tissue-sensor interaction surface across x-y plane; the z-displacement distribution with an indentation depth input of 0.64mm occurring at (b) the tissue-probe interaction surface on the costal cartilage exterior surface across the x-y plane, and (c) top surface of the transducer array below the built-in probe across x-y plane.....	77
3.11 Simulation results of (a) simulated CC elasticity, which are equivalent to the measured CC elasticity, as a function of CC diameter in the range of 3mm-14mm (100-7000: pre-set CC elasticity,kPa), and compensation coefficient, γ , as a function of (b) pre-set CC elasticity in the range of 100kPa-7000kPa (3-14: CC diameter, mm) at different CC diameters , and (c) CC diameter (h_i : 3mm-14mm) at different pre-set CC elasticity (E_i : 100kPa-7000kPa). (100-7000: pre-set CC elasticity, kPa).....	80
3.12. Original recorded data in a mechanical measurement: sensor deflection at the locations of the five transducers (1~5) as a function of time, in response to the pre-defined indentation depth input (a) CC #1 Anterior (b) CC #2 Anterior (1-5: sensor deflections for first measurement at transducer 1-5).....	81
3.13.The spatially distributed sensor deflection as a function of the indentation depth measured using the sensor with a built-in probe (solid line: instant values; dashed line: relaxed values) (a) anterior surface (b) posterior surface (c) superior border (d) inferior border of CC #2 (1-5: sensor deflections for first measurement at transducer 1-5)	82
3.14.Sensor deflection versus the indentation depth (solid line: instant values; dashed line: relaxed values) (a) CC #2 (b) CC #3 (A: Anterior; P: Posterior; S: Superior; I: Inferior)	85
3.15.Compressive stress as a function of time (a) CC #2 (b) CC #3 (A: Anterior; P: Posterior; S: Superior; I: Inferior).....	86
3.16.Normalized relaxation as a function of the indentation depth (a) CC #2 (b) CC #3 (A: anterior, P: posterior, S: superior, I: inferior)	86
4.1 Pictures of (a) the whole porcine 5 th ~ 12 th CC segments of right ribcage from an 18-month-old female pig with the locations for measurement being marked in blue or red at their exterior surface and with dash lines in the pictures (b) CC transverse cross-sections (5 th CC: Location 3) with the definition of depth and width.	92

Figure	Page
4.2 The measured compressive stress of CC as a function of time, in response to the multi-step indentation-relaxation testing protocol with $z=80\mu\text{m}$, $\dot{x}=0.2\text{mm}\cdot\text{s}^{-1}$ and $t_{\text{hold}}=40\text{s}$ (a) posterior surface of the 5 th CC segment at Location 1 (the stiffest location) (b) anterior surface the 9 th CC at Location 3 (the softest location).....	96
4.3 Measured instant indentation modulus at the anterior and posterior surfaces and their average at different locations along the cartilage length (from rib to sternum) of the CC segments (a) 5 th CC (b) 6 th CC (c) 7 th CC (d) 8 th CC(e) 9 th CC (f) 10 th CC (g) 11 th CC (h) 12 th CC.	98
4.4 Measured normalized relaxation as a function of the indentation depth (a) 7 th CC: Location 2 (b) 8 th CC: Location 6 (c) 9 th CC: Location 2 (d) 10 th CC: Location 3.	99
4.5 Average normalized relaxation of the anterior and posterior surface at each measured location as a function of the indentation depth (a) 5 th CC (b) 6 th CC (c) 7 th CC (d) 8 th CC (e) 9 th CC (f) 10 th CC (g) 11 th CC (h) 12 th CC.	99
4.6 Measured normalized relaxation along the cartilage length (from rib to sternum) of the CC segments (a) 5 th CC (b) 6 th CC (c) 7 th CC (d) 8 th CC(e) 9 th CC (f) 10 th CC(g) 11 th CC (h) 12 th CC.	100
4.7. (a) Instant indentation modulus at the anterior and posterior surfaces and their average of a whole CC segment (b) normalized relaxation at the anterior and posterior surfaces and their average of a whole CC segment.....	101
5.1 Pictures and schematics of human PC costal cartilage segments and the locations for measurement (a) CC #A (b) CC #B (c) CC #C (d) CC #D (e) CC #E	110
5.2 Measured normalized relaxation as a function of indentation depth of CC segment (a) CC#A (b) CC#B (c) CC#C (d) CC#D (e) CC#E (The color coded numbers indicate the measured locations)	111
5.3 Measured mechanical properties along the length (from rib to sternum) of CC at its anterior/posterior surfaces, superior/inferior borders and the average of the four positions (a) instant indentation modulus of CC#A-E (b) normalized relaxation of CC#A-E (A: Anterior; P: Posterior; S: Superior; I: Inferior; Average: Average values of four surfaces)	113

Figure	Page
5.4 Measured average viscoelastic properties of the CC samples at their anterior/posterior surfaces, superior/inferior borders and the average of the four positions (a) average instant indentation modulus (b) average normalized relaxation(A: Anterior; P: Posterior; S: Superior; I: Inferior; Average: Average values of four surfaces).....	114
A.1 LabVIEW front panel for manually control the micromanipular to apply x-direction, y-direction, z-direction displacement with a different ramp speed.....	133
A.2 LabVIEW block diagram for manually control the micromanipular to apply x-direction, y-direction, z-direction displacement with a different ramp speed.....	134
A.3 LabVIEW block diagram for (a) automatically control the micromanipular to apply x-direction, y-direction, z-direction displacement with a different ramp speed,(b) data collection, and (c) automatically screenshot the front panel after data collection.....	136
B.1 Measured normalized relaxation as a function of indentation depth of CC #A at (a) location 1 (b) location 2(c) location 3(d) location 4 (e) location 5. (Red line: sensor was deformed before the measurements).....	137
B.2 Measured normalized relaxation as a function of indentation depth of CC #B at (a) location 1 (b) location 2(c) location 3(d) location 4 (e) location 5 (f) location 6.(Red line: sensor was deformed before the measurements)	138
B.3 Measured normalized relaxation as a function of indentation depth of CC #C at (a) location 1 (b) location 2(c) location 3(d) location 4.(Red line: sensor was deformed before the measurements)	139
B.4 Measured normalized relaxation as a function of indentation depth of CC #D at (a) location 1 (b) location 2(c) location 3(d) location 4.(Red line: sensor was deformed before the measurements)	140
B.5 Measured normalized relaxation as a function of indentation depth of CC #E at (a) location 1 (b) location 2(c) location 3(d) location 4(e) location 5	141
B.6 Compressive stress as a function of time of CC # B at Location 3 (a) anterior surface (b) posterior surface (c) Superior border (d) inferior border	142

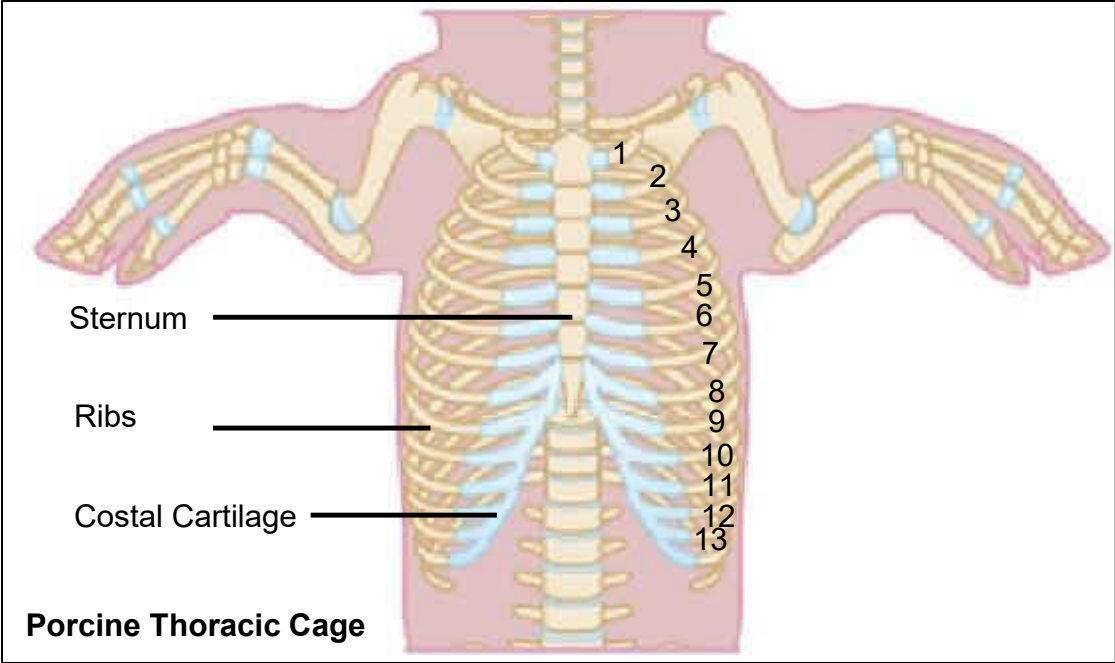
CHAPTER 1

INTRODUCTION

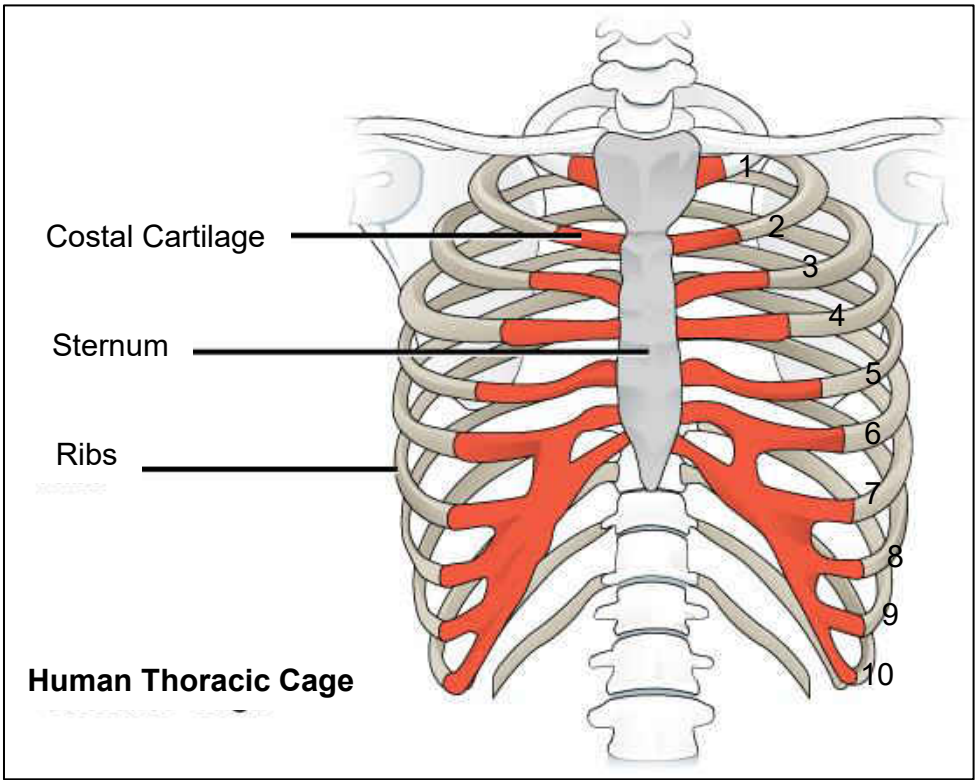
1.1. Biological Background

1.1.1. Biological Significance

CC are bars of hyaline cartilage that serve to extend the ribs forward, contribute to the elasticity of the wall of the thorax (Figure 1.1), articulate the anterior end of the ribs with the sternum (for ribs 1-7 in human, 1-8 in porcine) or costal arch (for ribs 8-12 in human, 9-13 in porcine) [1, 2], and protect the lungs and heart while respiration. As a load-bearing and non-stop deforming tissue from respiration, CC exhibit inherently heterogeneous mechanical properties at the microscopic-level, due to their heterogeneous anatomical microstructures [1, 3-6]. Thus, the mechanical properties of CC are critical for maintaining their structural health and delivering their function [7]. It has been well established that a change in the heterogeneous mechanical properties of CC may indicate the effects of disease on them [8, 9]. As such, acquiring the heterogeneous mechanical properties of cartilage tissues could not only aid in better revealing their physiological process and functionality, but also further assist in the analysis of tissue diseases, as well as their origin and progression[10]. Moreover, in cell-based tissue engineering, measuring the heterogeneous mechanical properties of cell-seeded engineering scaffolds allows quantifying the effect of specific growth factors on the distinguishing functions of the varying heterogeneous structures of such scaffolds at different growth stages and consequently their integrated mechanical function as a whole, and ultimately aids in regenerating CC tissue constructs with characteristics similar to native CC tissues for restoring physiological function[11].



(a)



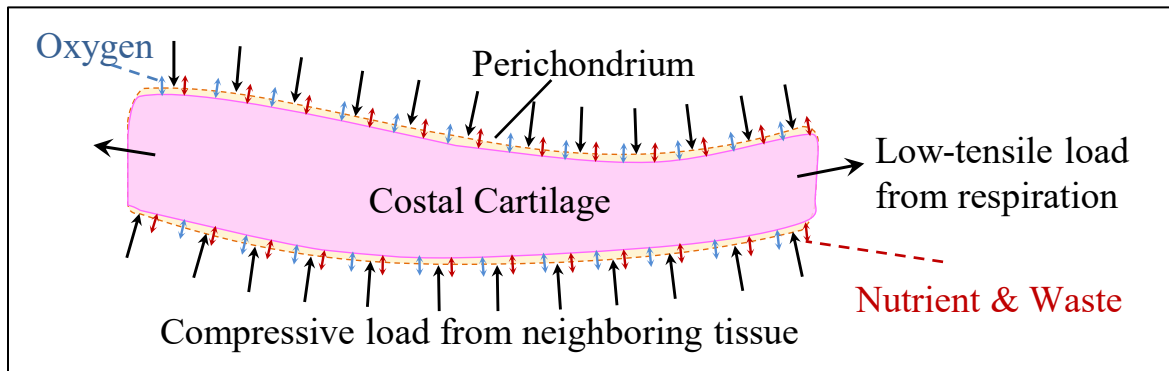
(b)

Figure 1.1 The structure of thoracic cage: (a) in porcine[12]; (b) in human [13].

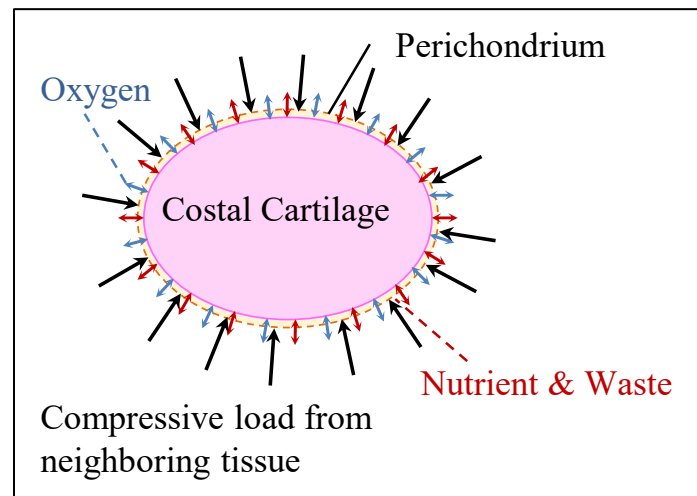
The structural characteristics of CC have been studied at the tissue-level, ultrastructural-level and molecular-level: content/organization of collagen and aggrecan, key regulators (Small Leucine Rich Proteoglycans SLRPs; e.g., biglycan and decorin) in collagen fibrillogenesis and organization, gene expressions, collagen fibril size/shape, and chondrocytes. Now, the basic structural characteristics of healthy CC are well established. In contrast to AC, CC are densely populated with chondrocytes. Like AC, CC contain high amounts of collagen and aggrecan in the Extracellular Matrix (ECM), but does not form layered structures as AC does. Instead, the collagen fibers in the ECM appear to form “straw-like” structures running longitudinally along the cartilage length, most likely for bearing low-tensile loading from respiration. Since decorin binds to and holds together individual collagen fibers, high levels of decorin expression in CC are likely associated with the large tubular structures (from the straw-like structure) running through the cartilage length.

For better serving as grafts and helping with tissue reconstruction, it is desirable to study the structural-function relations of CC, by analyzing their heterogeneous mechanical properties. As shown in Figure 1.2, CC experience low-tensile loading along the cartilage length for thoracic expansion and contraction, and low-compressive loading at their exterior surface along the transverse direction so as to obtain oxygen and exchange nutrient and waste for growth and assembly from a perichondrium. As such, the mechanical properties of CC at their exterior surface are intrinsic to maintaining their structural characteristics. Meanwhile, with the aid of compressive loading at the CC exterior surface, diffusion of oxygen and nutrients from the perichondrium can only penetrate a very short distance into CC and therefore the CC interior region lacks oxygen and nutrients and becomes hypoxic. Higher levels of aggrecan in the interior region over the peripheral region likely arise from the gradient of oxygen from peripheral to

interior, because aggrecan is more highly expressed under hypoxia. As such, the peripheral region differs in structure and functions from the interior region, and the mechanical properties at the CC exterior surface influence diffusion of oxygen and nutrients and thus are intrinsic to maintaining their structural characteristics.



(a)



(b)

Figure 1.2 Basic biomechanical environment of CC in the ribcage (a) along the cartilage length and (b) transverse cross-section.

1.1.2. Clinical Significance

Owing to its abundance and surgical accessibility, CC are used as graft tissue in autologous therapies, such as craniofacial surgeries and tracheoplasty, and cosmetic surgeries,

and as a cell source for engineered AC. Chest wall deformities of the sunken chest (pectus excavatum, PE) and the pigeon chest (PC), an incidence of 6/1000 to 0.97/1000 live births[14], are known to arise from the disorder of CC. Basically, PE is a prominent posterior intrusion of the anterior thorax wall caused when the sternum, lower CC, and the third to seventh ribs are abnormally pushed inward. It represents 90% of all chest deformity cases [15, 16], usually evident at birth or not developed until puberty and can be mild or severe if left untreated, including the derivation of cardiopulmonary function and spine deformities[15, 17]. In contrast, PC is an anterior intrusion of the posterior thorax wall caused when the sternum, the lower CC, and the second to ninth ribs are pushed outward and has not attracted as much interest from clinicians, pediatricians, orthopedists, and pediatric surgeons, and not even from thoracic surgeons, as has PE. Moreover, the impacts of thoracic deformities on patients are not only physiological, but also psychological [18]. Thus, in the past decades, the clinical research emphasizes more on the improvement of surgery operations to help with the patients and obtain excellent achievements [19]. For instance, one common minimal invasive technique for correction of PE is passing a pectus bar behind the sternum and then turning it over for pushing the chest forward. Figure 1.3 shows the proper technique for fixation of the pectus bar against the lateral chest wall musculature. However, compared to the significant achievements of operation, the exact cause of CC deformity still has not been well understood. Basically, the main leading hypothesis for the pathogenesis is a biomechanical weakness caused by a developmental disorder [15, 17] which may be caused by the insufficiency of collagen and PGs [4]. Therefore, in order to reveal the exact cause of CC deformity, it is reasonable to analyze and compare the heterogeneous mechanical properties and biological structure of the CC from the patients with abnormal CC deformity, such as PC patients.

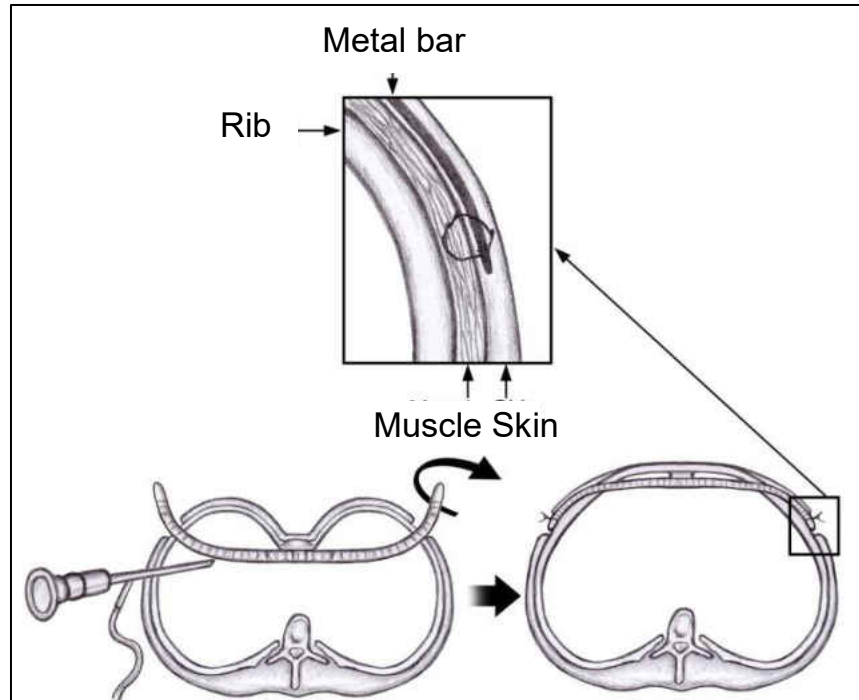


Figure 1.3 Illustration of the pectus bar passed behind the sternum before and after it is turned over. The insert shows the proper technique for fixation of the pectus bar against the lateral chest wall musculature[20].

1.2. Experimental Studies of Costal Cartilage

CC function as a low-friction, wear-resistant, load-bearing tissue. The mechanical properties of normal (developing or mature), diseased, and repaired CC are very important indicators of their level of structure and function for restoration and replacement of themselves and designing and fabrication of implants. Thus, some of the major methods used to assess the mechanical properties of CC are discussed in this section. The conventional modes of testing at a macroscopic-level for cartilage mechanical properties include compression, tensile, flexure and macro-scale indentation. As compared to multiple choice of the testing at macroscopic-level at microscopic-level, the most common method for testing cartilage mechanical properties is nanoindentation.

A typical mechanical test of CC requires mechanical test instrumentation, or a mechanical spectrometer, that applies displacement (or load) and measures the load (or displacement) response over time. Data should be stored for later reduction and analysis. Data storage typically consists of the conversion of analog signals, such as voltages from a load cell or displacement transducer, to digital format by an analog-to-digital converter (A/D converter). During this process, the recorded signal may be erroneous if the sampling rate is not high enough. As such, in practice, sampling rates of two to five times the minimum sampling interval (half of the highest frequency) are used. Meanwhile, for measurements intended to reflect cartilage in its normal state, a physiological solution is typically used, and testing samples under conditions that cause evaporation and dehydration, or conversely, swelling, should be avoided. Thus, the conventional mechanical measurements of CC should be conducted with the samples bathed in a defined solution, such as Phosphate-buffered saline (PBS) supplemented with proteinase inhibitors at physiological pH. Such inhibitors retard the breakdown of cell and matrix components by enzymes that may be active or become activated during the course of the testing procedure.

1.2.1. Compression Tests

A common method to assess the compressive properties of cartilage is compression tests including the uniaxial confined and unconfined test. Particularly, unconfined compression test is most adopted for characterizing the CC. In the meantime, compression tests require large enough tissue for making the test samples. In the uniaxial confined compression test, typically, cartilage is compressed in a radially confined chamber, usually with a solid impermeable bottom surface and a water permeable porous loading platen covering the top surface as shown in Figure 1.4 [21]. Relative motion between the platen and bottom surface causes fluid movement, ideally

only through the porous platen, with resultant intratissue dynamics being in one dimension. Since the stiffness of the platen is high compared with the tissue, and the fluid is virtually incompressible, the major mechanism by which the tissue deforms is by exudation of the fluid through the surface that is in contact with the porous platen. In the unconfined compression test, a cartilage sample is placed between two flat, impermeable platens that are ideally rigid and frictionless as depicted in Figure 1.5. The sample is compressed and allowed to expand laterally in the radial direction. Since the resulting motion is both axial and radial, more complex theoretical models are needed.

Moreover, the compression test can be performed with control of either load, F , or displacement, u . Under load control, the tissue undergoes creep displacement, gradually achieving equilibrium. Under displacement, the load dissipates over time (stress-relaxation), also leading to equilibrium [21]. The modulus of the tissue can be computed from equilibrium values. From time-varying displacement and load, the permeability of the tissue can be determined by fitting the data to a theoretical model. There are certain advantages to performing a test in displacement control rather than load control. Displacement control allows testing a sample from a true “zero” displacement, which is straightforward to determine. In contrast, load control typically requires the application of a nonzero load (and displacement) to initiate a test, and this alteration of sample thickness needs to be considered in reducing data to structural or material properties. Often in load control, only the change in sample thickness relative to an initial state is measured, with the initial state assumed to represent the free swelling state. However, tare loads can impart significant distortion to the tissue and make this assumption erroneous.

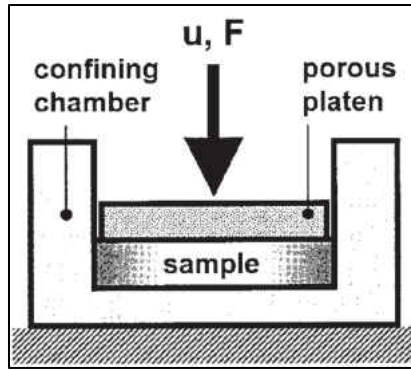


Figure 1.4 Schematic of confined compression testing apparatus[21].

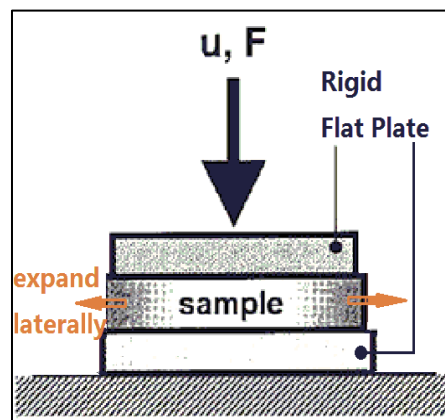


Figure 1.5 Schematic of unconfined compression testing apparatus[21].

Jiexiong Feng et al.[17] applied uniaxial unconfined compression test in the direction parallel to the cartilage surface on fourteen samples of the 6th PE CC (aged from 3 to 6 years; mean, 4.2 years) and ten samples of the healthy CC (aged from 3 to 6 years; mean, 4.4 years) which are trimmed to 3cm ×0.8cm cylinder shape and stored in Ringer's solution at 4°C for 2 hours before testing. The test was carried out on a material testing machine (Shimadzu Model AG-10TA, Tokyo, Japan) with the cross-head set to move at 5 mm·min⁻¹. During the test, the specimen was kept in buffered saline, and the environmental temperature was maintained at 25°C. By transforming the relation curve of load-deformation to the relation curve of stress-strain relation, Jiexiong Feng's group found that the average compression strength of healthy CC is 8.29±0.23MPa, which is significantly higher than the 1.33±0.22MPa in PE CC.

W. Grellmann et al[22] punched out cylinder shape CC samples from the 6th and 9th ribs (both male and female, age 37-86 years) with both a length and a diameter of 6mm. The production of the plane-parallel test specimen was carried out using a friction sawing device of Exact Norderstedt under permanent cooling with Ringer's solution. The test is carried out in a Zweick universal testing machine. These samples were fixed between rigid high stiffness plates, and the lower plate was raised at a rate of $1 \text{ mm} \cdot \text{min}^{-1}$ to produce a compression load. As a result, the measured modulus of elasticity in compression is extremely high, $103.4 \pm 30.1 \text{ MPa}$. The measured compression strength is $7.6 \pm 1.8 \text{ MPa}$.

1.2.2. Tensile Tests

Tensile tests performed on CC are using either a commercial or customized test system. Furthermore, for better holding in the fixture, all CC are cut into strip or dumbbell shapes. Like the compression test, the tensile test also requires large enough tissue for test specimen fabrication. When performing a mechanical test in tension, a cartilage sample is typically extended at a constant dynamic rate of extension (Figure 1.6(a)), or it can be extended sequentially by small displacements and allowed to relax to equilibrium states. CC exhibit stress-relaxation behavior when tested in tension (Figure 1.6(b)). This behavior has been described by the quasi-linear viscoelastic theory. When cartilage is loaded rapidly, the flow of interstitial fluid, which is dependent on cartilage permeability, can contribute to cartilage resistance to that load. Dynamic tensile experiments can yield stiffness values that are dependent on the interstitial fluid flow, and use of these load values can lead to high estimates of intrinsic equilibrium tensile properties. Dynamic tensile experiments are convenient for assessing tissue strength and stiffness, whereas equilibrium tensile tests give measurements allowing assessment of the elastic tensile material properties. For example, human AC from the femoral condyles can exhibit a ramp

modulus of 200 MPa and withstand a stress of 30 MPa before failing. In contrast, at equilibrium, the same tissue exhibits an intrinsic tensile modulus of 5 MPa [26]. These values are site- and depth-dependent and can vary depending on the structure and content of collagen and proteoglycans in the ECM. However, for cases in which the cartilage has been eroded, with disruption of cartilage integrity or exposure of bone, a tensile test may not be suitable.

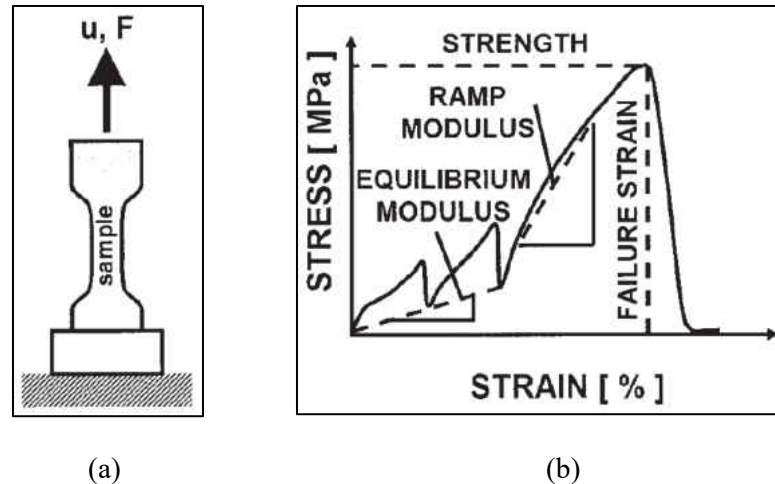


Figure 1.6(a) Dumbbell-shaped specimen used in a tensile test is extended at a constant rate while the load is measured. (b) Equilibrium and dynamic tensile testing. Force and displacement are normalized to cross-sectional area and gage length at 0% strain, respectively, to give stress and strain. The strength, or failure stress, and failure strain is obtained from the dynamic stress–strain data. The ramp modulus is calculated as the slope of the best-fit line between 25 and 75% of the maximum stress. The equilibrium tensile modulus can be obtained from the best-fit line between the three equilibrium data points [26].

Bi-yun Guo et al.[3] tested the healthy human CC samples with different age and gender on an Instron materials testing machine. During the measurement, the CC samples were cut into dumbbell-like shape with a 10-15mm length, a minimum 1.5-3mm width or cylinder shape with a 30mm length and 0.8mm radius, and fixed on two self-made clamps. The clamp on the bottom end was fixed on a fastened lower grip while the clamp on the top end could move at a specified speed in the vertical direction (Figure 1.7). The forces in the tensile strength, stress-strain relationship, stress relaxation, and creep characteristics testing were measured using a 100N sensor and the displacement was controlled by the testing machine. The experiment was

performed at room temperature, with an ultrasound moistener to keep the specimen moist. Biyun Guo et al. found the tensile strength of female children, female adolescent, female adult, male children, male adolescent and male adult were 5.96 ± 0.38 , 7.20 ± 0.70 , 4.27 ± 0.41 , 4.60 ± 0.56 , 5.31 ± 0.33 and 4.30 ± 0.59 MPa, respectively, which indicated that the children group has the highest tensile strength in both male and female groups. The adolescent group has the lowest strength, which could be a reason that the bigger distortion happened after using the adolescent CC in the auricular reconstruction operation, as compared to using children's CC. Moreover, the male group relaxed and crept more than that of the female group in all three age groups. Thus, the recorded results show the biomechanical properties of CC are donor age and gender related.

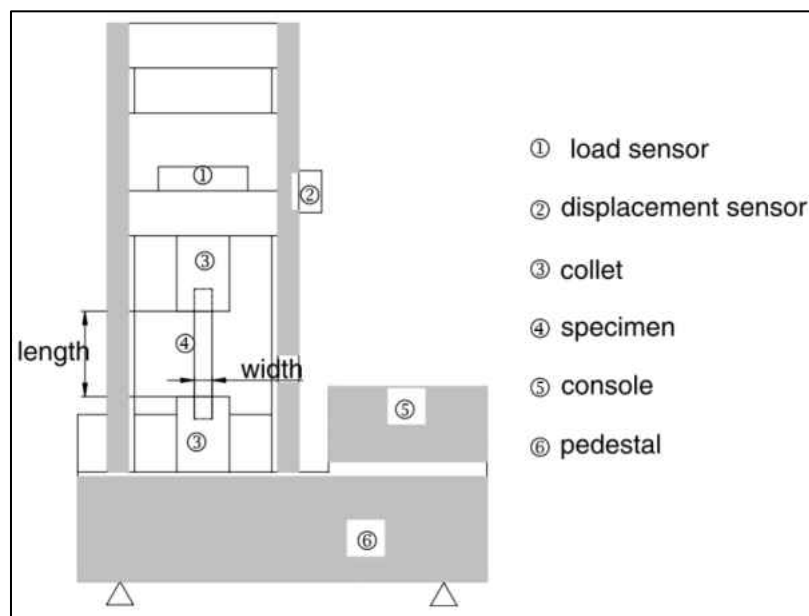


Figure 1.7 Schematic of tension test apparatus [3].

Jiexiong Feng's group[17] applied the uniaxial tensile test in the direction parallel to the cartilage surface on fourteen samples of the sixth PE CC (aged from 3 to 6 years; mean, 4.2 years) and ten samples of the healthy CC (aged from 3 to 6 years; mean, 4.4 years) which are trimmed to $3\text{cm} \times 0.8\text{cm}$ cylinder shape and stored in Ringer's solution at 4°C for 2 hours before testing. The test was carried out on a material testing machine (Shimadzu Model AG-10TA,

Tokyo, Japan) with the cross-head set to move at $5 \text{ mm} \cdot \text{min}^{-1}$. The specimen was kept in buffered saline, and the environmental temperature was maintained at 25°C . By transforming the relation curve of load-deformation to the relation curve of stress-strain relation, Jiexiong Feng's group found that the average tensile strength of healthy CC is $2.27 \pm 0.23 \text{ MPa}$, while the average tensile strength of PE CC is only $1.52 \pm 0.37 \text{ MPa}$. The test result shows that PE CC has less tensile strength as compared with healthy CC.

1.2.3. Flexure Test

Flexure tests are generally used to determine the flexural modulus or flexural strength of CC. Flexural strength is defined as the maximum stress at the outermost fiber on either the compression or tension side of the specimen. Flexural modulus is calculated from the slope of the stress vs. strain deflection curve. These two values can be used to evaluate the CC ability to withstand flexure or bending forces.

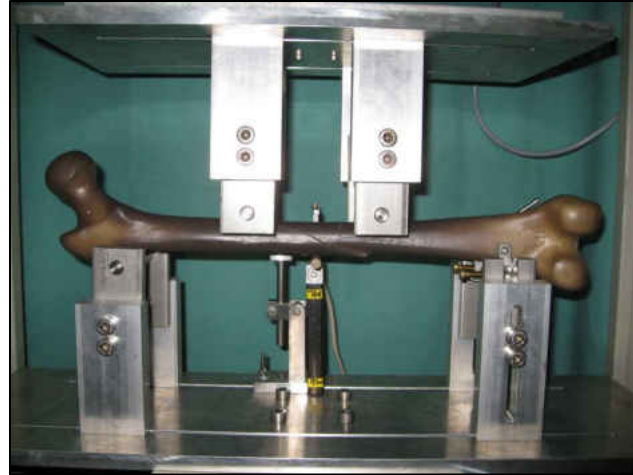
In flexure tests, CC are laid horizontally over two points of contact (lower support span) and then a force is applied to the top of the material through either one or two points of contact (upper loading span) until the sample fails. As such, the two most common types of flexure tests are three-point and four-point flexure bending tests. A three-point bend test as illustrated in Figure 1.8 (a) consists of the sample placed horizontally upon two points and the force applied to the top of the sample through a single point so that the sample is bent in the shape of a "V". A four-point bend test as in Figure 1.8 (b) is roughly the same except that instead of the force applied through a single point on top it is applied through two points so that the sample experiences contact at four different points and is bent more in the shape of a "U". Unlike a compression test or tensile test, a flexure test does not measure fundamental material properties. When a specimen is placed under flexural loading all three fundamental stresses are

present, tensile, compressive, and shear, so the flexural properties of a specimen are the result of the combined effect of all three stresses as well as (though to a lesser extent) the geometry of the specimen and the rate the load is applied. Usually, a flexure test is more affordable than a tensile test and test results are slightly different. A three-point flexural bending test is typically adopted for the testing of CC, since it is more suitable for testing smaller samples[22].

Jiexiong Feng's group[17] applied a flexure test in the direction perpendicular to the cartilage surface on ten samples of the sixth PE CC (aged from 3 to 6 years; mean, 4.2 years) and eight samples of the healthy CC (aged from 3 to 6 years; mean, 4.4 years) which are trimmed to 3cm ×0.8cm cylinder shape and stored in Ringer's solution at 4°C for 2 hours before testing. The test was carried out on a material testing machine (Shimadzu Model AG-10TA, Tokyo, Japan) with the cross-head set to move at 5 mm·min⁻¹. During the test, the specimen was kept in buffered saline, and the environmental temperature was maintained at 25°C. By transforming the relation curve of load-deformation to the relation curve of stress-strain relation, their group found that the average flexure strength of healthy CC and PE CC are 7.64±1.88MPa and 4.13±1.22MPa, respectively. Additionally, the time of damage in the PE CC group is 30 seconds, and shorter than 38 seconds as measured in the healthy CC group.



(a)



(b)

Figure 1.8 Experimental setup for (a) three-point bend test [23] ; (b) four-point ben test[24].

W. Grellmann et al[22] separated the cylinder shape CC samples from the 6th and 9th ribs (both male and female, age 37-86 years) with both a length and diameter of 6mm. The production of the plane-parallel test specimen was carried out using a friction sawing device of Exact Norderstedt under permanent cooling with Ringer's solution. In Zweick universal testing machine, the test was carried out using the three-point loading arrangement as showed in Figure 1.9. The deflection rate at the center loading point was controlled by the cross head movement, which was set at $1\text{mm}\cdot\text{min}^{-1}$. The measured bending modulus and strength are $8.8\pm 2.9\text{ MPa}$ and $24.3 \pm 12.2\text{ MPa}$, respectively.

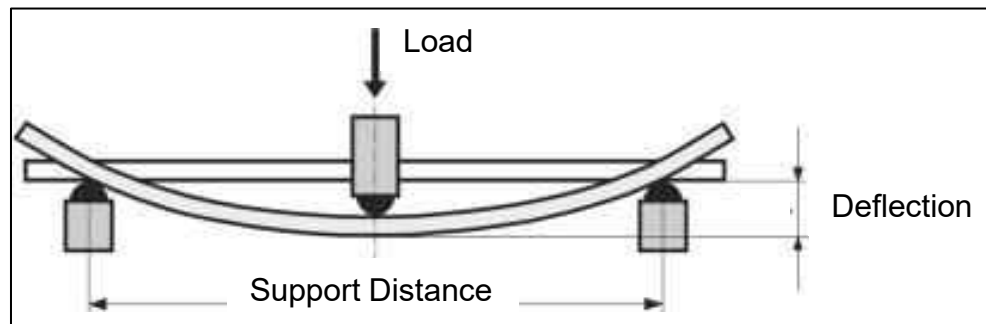


Figure 1.9 Measuring arrangement of three-point bend flexure test for determination of bending properties in W. Grellmann's group [22].

In Rani Roy's group[25], they also used a three-point bend test for characterizing the bending behavior of porcine CC. The CC samples were harvested from 4-8 week old porcine within 1 hour of sacrifice, cut into strips (20mm × 4mm×1mm) with perichondrium being removed, and stored frozen at -20 °C until testing. During the three-point bend test as illustrated in Figure 1.10, the load and displacement were measured throughout testing. Porcine CC strips were placed on grips that were 5 mm apart and the load applicator was located above the center of the strip. Data was sampled every 0.5s with a right deflection of 0.02 mm·s⁻¹ and a load resolution of 10mN. During testing, cartilage strips were kept hydrated with PBS solution. Frozen tissue also was tested in comparison to fresh tissue with no difference found in the modulus. A mathematical model was adapted from the large-deflection plate theory to evaluate the elastic properties of CC. The calculated bending modulus of CC is 7.06 MPa.

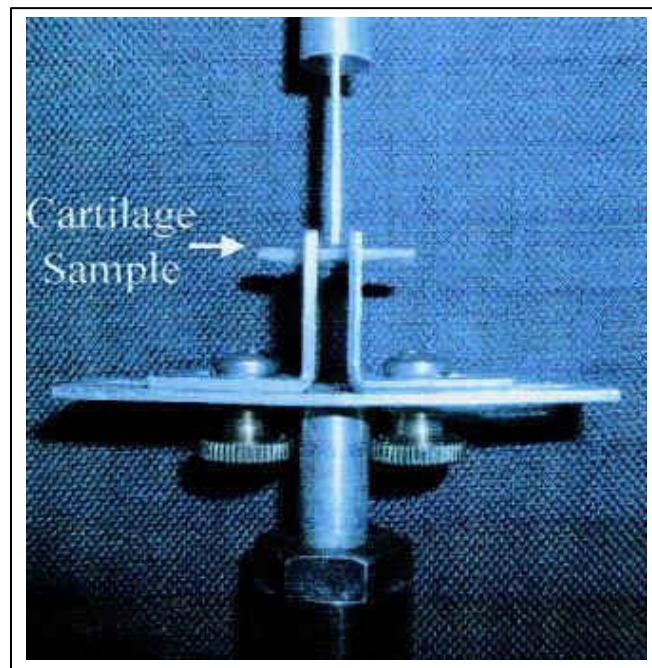


Figure 1.10 Depiction of three-point bend setup in Rani Roy's paper [25]. Samples were tested in three-point bending where the thickness was measured for each sample. The samples were placed between two grips a distance, ranging from 0.5–1.0 cm apart. Deflections were applied and resultant loads were measured.

1.2.4. Macro-scale Indentation Tests

A macro-scale indentation test as shown in Figure 1.11 (a) is performed on cartilage tissue by compressing a surface of cartilage using a rigid (relative to cartilage) object of known size, shape, and boundary conditions (permeability and friction), and then measuring load, displacement, and time. The test patterns are shown in Figure 1.11 (b). It is usually implemented via a custom displacement-controlled indentation instrument (CDI). The indenter tip size (i.e., diameter) is typically smaller than the cartilage thickness in order to minimize the effect of the rigid underlying material (bones, holding plates) on the stiffness measurement. The macro-scale indentation testing has been widely used for characterizing the health and function of cartilage because of the relative ease of the experimental setup as well as the availability of classical and more recent mathematical solutions for estimating biomechanical properties of cartilage from indentation test results.

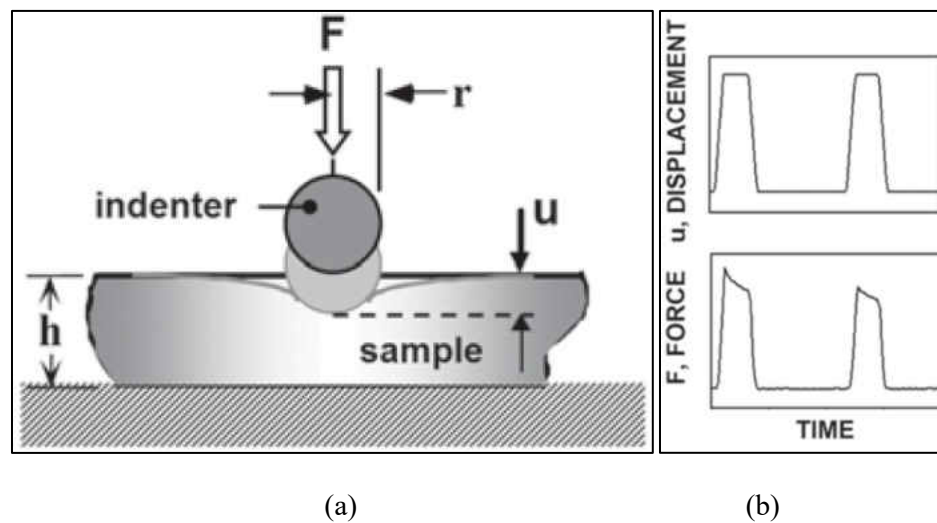


Figure 1.11 (a) Cross-section schematic of indentation testing using a sphere-ended tip r and a displacement-controlled protocol (b) Applied displacement or resultant load are illustrated[26].

Macro-scale indentation testing is now extensively employed for examining the mechanical behavior of healthy CC midsubstance [1, 4, 27] at its cross-sections. All indentation

tests carried out on CC in the literature requires the CC to be deconstructed and cut into slices (6-10mm) for learning the cartilage midsubstance feature. Moreover, for CC characterization, the sphere tips were always chosen during the measurement (2-3.15mm radius) to indent on the specimen surface to a certain penetration depth (<10% of the specimen thickness) with ramp-up time (0.5-2.125s) and was held for 10 times longer than the ramp-up time (2min). Data of a representative CC indentation load-time relaxation response is recorded and sampled at 100Hz-150Hz [4].

Anthony Lau et.al [1] uses a CDI to test 11 fresh human CC, both males and females, with an age range of 23-77 years. Samples were thawed and CC cross sections approximately 6 mm thick were prepared from the second, third and fourth left ribs (Figure 1.12 (a)). Indentation tests were performed on the midsubstance of the CC cross sections (Figure 1.12 (b)). The spherical indenter tip used by Anthony Lau et.al was machined from stainless steel to a diameter of 3.15 mm and mounted on a CDI. The input indentation test parameters were a target peak displacement of 0.425 mm (7% of tissue thickness), which gives a contact radius of approximately 0.82 mm (substantially smaller than the cartilage sample size). The target rise time was 2.125 s and the peak displacement was held for 2 min for load-relaxation. Depending on the amount of available tissue, 11–25 individual indentation tests were performed per ribcage specimen for a total of 188 individual tests. During the test, CC were soaked in 0.9% saline solution. Averaged over the entire study, the current result found a similar modulus for adult human CC (5.2 MPa) as was found for young porcine cartilage as mentioned in some previous studies, which calculated the three-point bending modulus (7.1 MPa)[17, 25] for 4–8 week old porcine cartilage samples. Their own previous study obtained the modulus results for time-zero was slightly smaller but comparable (5.3 MPa)[28]. These reported CC values in the range 5–7

MPa are found in all cases. Furthermore, the changes in proteoglycan solubility and water content of the tissue appear consistent with a greater mechanical stiffness of CC[1].

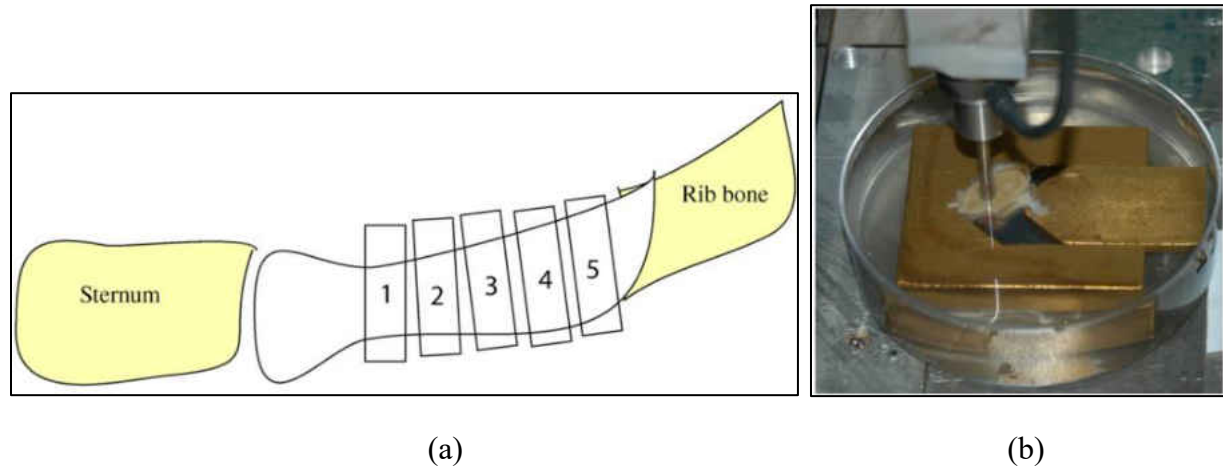


Figure 1.12 (a) A schematic illustration of CC cross section preparation. Multiple cross sections were cut in the cartilage between the sternum and rib bone, using a parallel-blade device such that each section was separated by a thin slice of discarded tissue. (b) A section of CC during the indentation test. Cartilage is held by a custom holder inside a Petri dish filled with 0.9% saline solution[1].

In Jason Forman's group[27], five whole healthy CC segments were harvested from the 4th ribs of human cadavers with perichondrium being removed. Each CC segment was separated into 3-4 cross-sectional test samples (each approximately 6 mm thick). Each of these samples was potted in a plastic dish with Fast Cast[®], with the cross-sectional surface to be indented facing upwards (Figure 1.13 (a)). Prior to testing, each of the samples was soaked in a bath of physiologic saline at body temperature for approximately 30 min. After placing the CC disks on the testing stage of CDI, the indenter tip (2mm diameter sphere) moved at approximately $0.5\text{mm}\cdot\text{s}^{-1}$ (attaining this velocity prior to contact with specimen, so as to reduce inertial effects) till penetration into the cartilage to a depth of approximately 0.25mm (approximately 4% of the sample thickness) (Figure 1.13 (b)). At this small relative depth of penetration, the tests can be regarded (and analyzed) to be an indentation into an infinite half-space. The average measured instantaneous elastic moduli of all the healthy human CC ranged

from 8.7 to 12.6MPa.

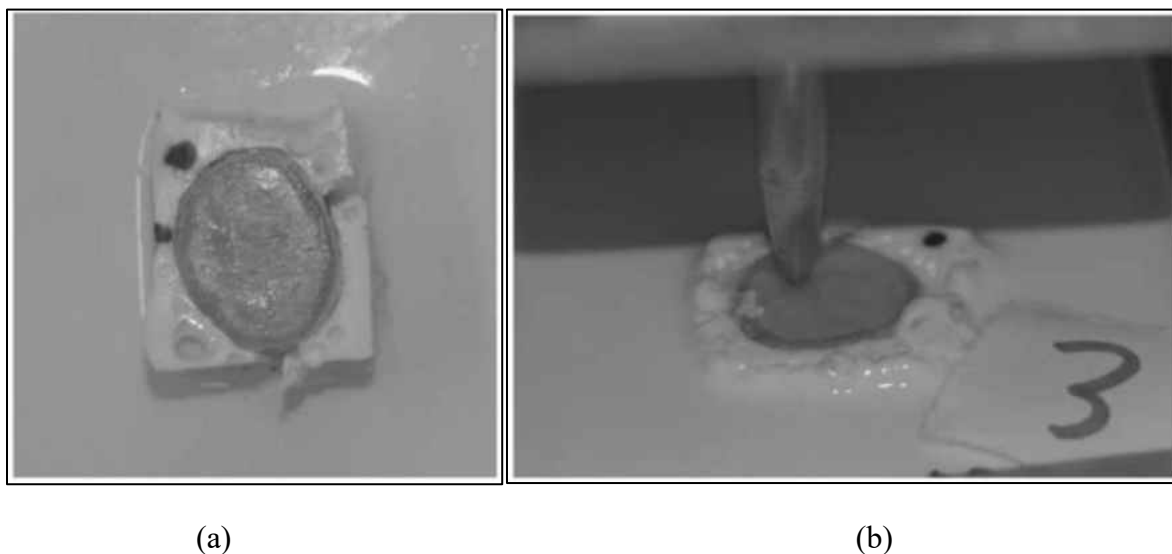


Figure 1.13 Pictures of indentation testing: (a) a cross-sectional CC specimen prepared and potted in fast-cast; (b) a specimen being subjected to an indentation test[27].

The CC segments used by JM Mattice and his group[28] were harvested from immature female porcine with age 28 days to 132 days. Each CC segment was further cut into 5-mm-thick cross-sectional slices. Each prepared specimen was allowed to equilibrate in a physiological saline bath at room temperature (25 °C) prior to testing. The CC test was indented by a 3.15-mm-diameter spherical indenter tip in a customized CDI instrument as shown in Figure 1.14. Indentation tests were conducted in physiological saline at room temperature. CC indentation tests were performed at three different peak displacement levels (0.225, 0.325, 0.425mm) at a fixed rise time of 1.84 ± 0.1 s for all three displacement levels and with a 120s hold time at peak displacement. The force-time data for each displacement level were used for analysis. As a result, the measured instant indentation modulus is 5.3MPa, respectively.

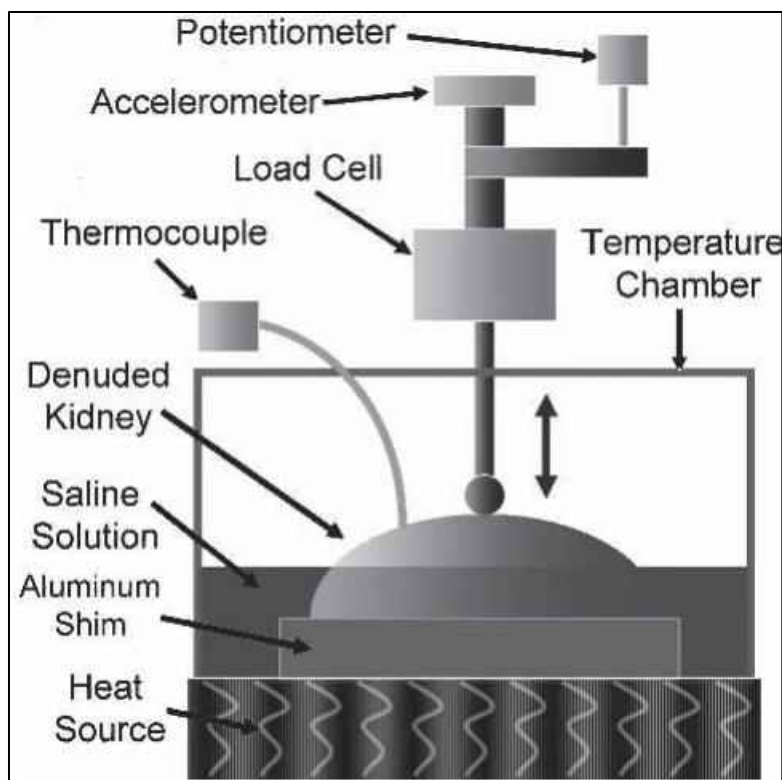


Figure 1.14 Schematic illustration of the CDI instrument used for experiments in JM Mattice's study [20].

M.L. Oyen et al [29] carried out macro-scale indentation measurement on human CC. Human CC were obtained from the fifth rib of two female subjects at age 32 and 71, store frozen and thawed prior to testing. In indentation test, the CC were cross-sectioned into sections with 5 mm thickness as illustrated in Figure 1.15. Prior the testing, the prepared human CC were equilibrated and tested in a physiological saline at room temperature ($\sim 25^\circ\text{C}$). In the indentation test, a spherical steel indenter tip with a diameter of 3.15mm was used to indent the CC samples to 0.4 mm peak displacement with a rise time of 2.1 seconds and hold time of 120 seconds. The obtained 5th human CC modulus is 10 MPa.

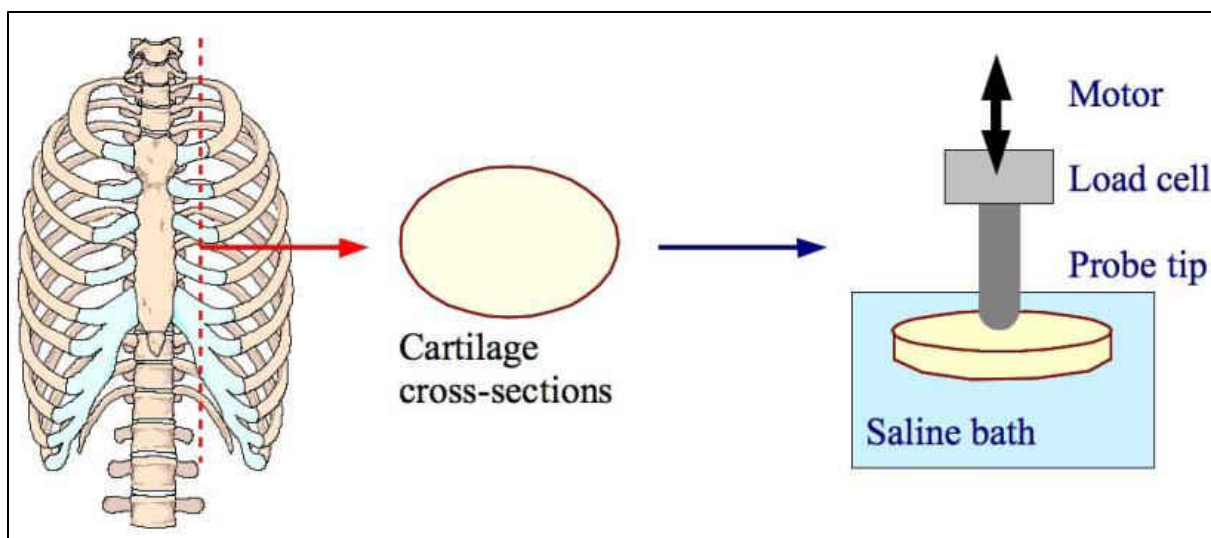
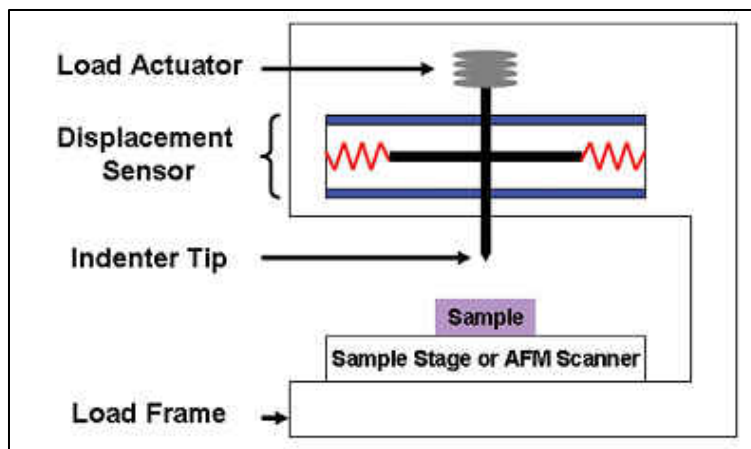


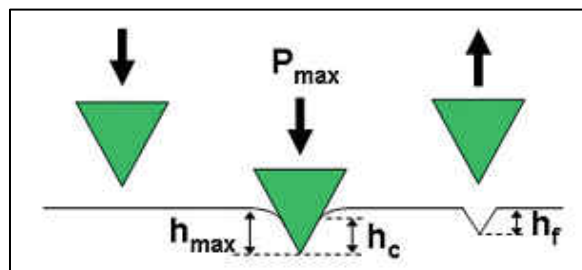
Figure 1.15 Schematic illustration of the CC indentation testing procedure developed in M.L. Oyen's work[29]. CC are sectioned and cross-sections are indented in the cartilage mid-substance using a CDI instrument.

1.2.5. Nanoindentation tests

Nanoindentation, also named as instrumented or depth-sensing indentation, typically implicates by AFM or nanoindenters to induce local surface deformation by controlling load to the surface. Take the commercial nanoindenter system as shown in Figure 1.16 (a) for example, during the measurement, the tip of a nanoindenter system with a three-plate capacitor for displacement (1 nm to 20 μm) sensing is mounted directly onto the middle plate of the capacitor. While a load (1 μN to 500 mN) is applied to move the tip into the specimen and monitored by electrostatic force generation, magnetic coils, or expansion of a piezoelectric element, the displacement is directly captured through capacitance or inductance[30]. Figure 1.16 (b) illustrates the interaction between the tip and the specimen during the indentation process. Meanwhile, rested on the continuously monitored data of load and displacement during the indentation process, a load-displacement curve can be extracted which is similar to the one shown in Figure 1.17 [30].



(a)



(b)

Figure 1.16 (a) Schematic of a nanoindenter system; (b) the indentation process P_{max} =maximum load, h_{max} =penetration depth, h_c =contact depth (the height of the contact between the tip and the sample); h_f =final depth; S = unloading stiffness. [30]

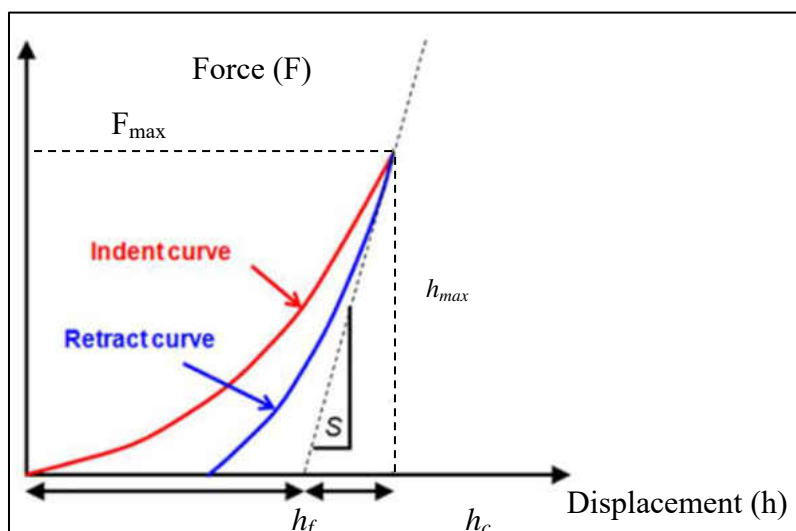


Figure 1.17 Schematic of a typical load-displacement curve [30].

Because of its millimeter-sized probes, nanoindentation can be used for the characterization of cartilage and other soft tissues. For instance, when the nanoindentation is implied by AFM, a 1-10 μm radius of the probe tip can be chosen for CC characterization with a ramp up time 10-25s and a holding time 125s which is 10 times longer as claimed in traditional indentation tests. Currently, a large portion of the biomaterial nanoindentation literature focuses on the measurement of material properties such as Young's modulus or elastic modulus [7, 31], and indentation hardness (H)[32] from nanoindentation data. Data of a representative CC nanoindentation load-time relaxation response is recorded and sampled at 100Hz-150Hz as well as the traditional indentation tests[4].

S. Tripathy and E. J. Berger [4] filled up the blank of AFM data on CC in the literature. In their study, AFM indentations using spherical beaded tips of radii 1, 5 and 10 μm were performed on the medial surface of healthy human CC (third rib from male cadavers with ages 54, 62 and 31 years) to isolate the mechanical properties. Thus, each specimen was cut into 7-10mm thick disks as shown in Figure 1.18. The indentation depth cannot be accurately controlled in the AFM test, so the maximum penetration depth was approximately maintained. The maximum depth was always much below the limit (10% of the sample thickness). The relaxation time was more than 10 times the ramp time. The overall length of each indentation was between 10 and 25 s. For some tests longer hold time of about 100–125 s was used. About 25–30 min was allowed before the indentations for the cantilevers to thermally equilibrate to the surrounding fluid medium. Indentations were performed at about 400–500 different sites on each cross section. Indentations were performed at about 400–500 different sites on each cross section. After plugging in the collected data into their model, the mean Young's modulus of CC was found to be about 2.17, 4.11 and 5.49MPa for three CC samples. As compared with the elastic

modulus values of AC found in the literature using AFM indentation (0.027 and 2.6MPa for porcine, 0.045 and 0.481MPa for bovine and 2.34 for rabbit)[33-36], they suggested that the CC is stiffer than the AC. In their study, the average elastic moduli (over all the cross sections) of human CC were 2.17 ± 1.32 , 4.11 ± 1.87 and 5.49 ± 2.41 MPa for each of the samples. Overall a range of 1–10MPa was obtained. Furthermore, a large variation of modulus was observed over the tissue. Also, the modulus values decreased with distance from the costochondral junction[4].

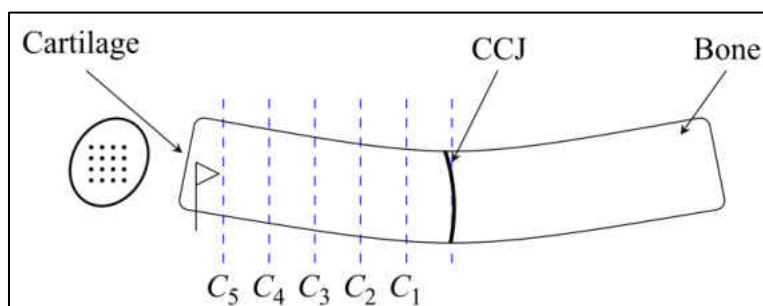


Figure 1.18 Sections of the CC. C_1 is closest to the costochondral joint and C_5 is the farthest. The modulus decreased from C_1 to C_5 [4].

In Shikha Gupta's study[37], porcine CC were chosen as a test material since, like other types of hyaline cartilage; it exhibits the nonlinear viscoelastic response and is uniformly heterogeneous. Three young porcine whole spare ribs were obtained from a local abattoir within 24 h of sacrifice. The third and fourth costal ribs were dissected from the sternum of each slab and cut into multiple samples. From each rib ($n=5$) one specimen, approximately 3 mm thick, was cored for nanoindentation and snap frozen in optimal cutting temperature solution. Since nanoindentation depths are less than 5 μm , experimental load–displacement curves are sensitive to surface asperities and roughness. To minimize errors from asperities, the top and bottom surfaces of the PC CC samples were cryomicrotomed prior to testing to ensure a smooth indentation surface. Before the test, frozen samples were first brought to room temperature by thawing in air. The optimal cutting temperature solution was removed by repeated rinsing with

PBS for approximately 30 min. During experimentation, all samples were placed in a Petri dish and immersed in room temperature PBS supplemented with protease inhibitors (5 mM benzamide-HCL and 10 mM N-ethylmaleimide) to prevent autolytic activity during experimentation. All indents were performed using a Hysitron TriboIndenter (Hysitron, Minneapolis, MN) in displacement controlled feedback mode. Indents were taken with a 100 μm radius of curvature conospherical diamond indenter. To facilitate testing in fluid, as shown in Figure 1.19, the diamond tip was attached to a 5 mm long titanium shaft. Indents were performed on 11 to 12 different positions on each of the 5 samples. The indenter displacement was linearly ramped to a maximum penetration depth of either 2.0 μm or 3.1 μm at a displacement rate of either 0.2 $\mu\text{m}\cdot\text{s}^{-1}$ or 2 $\mu\text{m}\cdot\text{s}^{-1}$, followed by a 150s hold period at the maximum penetration depth, and withdrawn at a rate of 0.2 $\mu\text{m}\cdot\text{s}^{-1}$. A total of 44–48 indents were performed on each specimen.

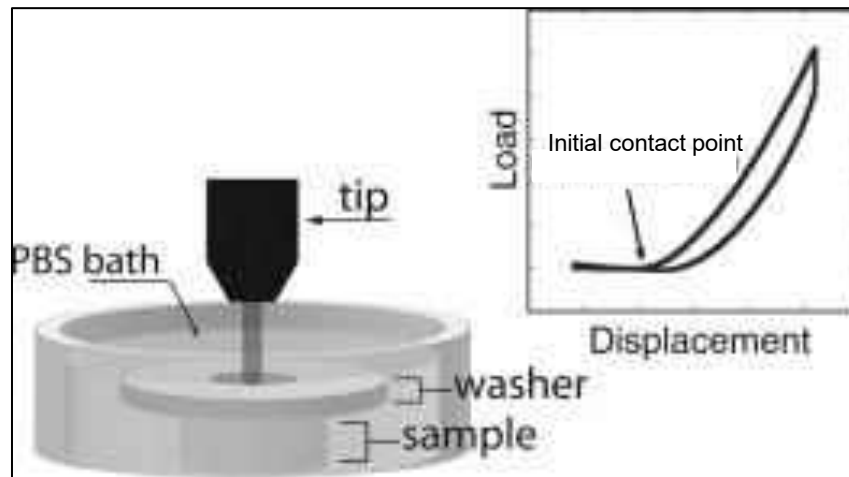


Figure 1.19 Schematic of the experimental setup for nanoindentation of porcine CC [37].

Shikha Gupta's group [37] found when the loading and initial relaxation response is at 0.2 $\mu\text{m}\cdot\text{s}^{-1}$ indentation rate. The total load relaxes by 17.3% within 30s of the hold time. However, when the loading and initial relaxation is at 2 $\mu\text{m}\cdot\text{s}^{-1}$, the total load relaxes by 29.5% with 20s of the hold time. Overall, for the 3.1 μm indentation depth, the relaxation in the load is 15.8% \pm 2.6%

and $28.74\% \pm 2.9\%$ (mean \pm S.D.) for the $0.2 \mu\text{m}\cdot\text{s}^{-1}$ and $2 \mu\text{m}\cdot\text{s}^{-1}$ displacement rates, respectively and $18.6\% \pm 3.1\%$ and $32.1\% \pm 4.3\%$ for the $2.0 \mu\text{m}$ depth. For all indents, an increase of 20%–22% in the maximum load is observed with an order of magnitude increase in the indenter displacement rate. Moreover, Young's modulus of all five samples for the $0.2 \mu\text{m}\cdot\text{s}^{-1}$ and $3.1 \mu\text{m}$ indentation depth is $1.65 \pm 0.45 \text{MPa}$.

1.3. Motivation

CC are bars of hyaline cartilage that connect the ribs to the sternum for providing the structural strength and flexibility of the thoracic cage. Owing to its abundance and surgical accessibility, CC are used as graft tissue in autologous therapies, such as craniofacial surgeries and tracheoplasty, and cosmetic surgeries, and as a cell source for engineered AC. Two most common types of chest wall deformity, sunken chest (PE) and pigeon chest (PC) are known to arise from the disorder of CC. The biological composition and structure of healthy and PE/PC CC are now well known, but the structural analyses at the tissue-level, ultrastructural-level, and molecular-level have all failed to identify significant differences between healthy and diseased CC.

As a load-bearing and nonstop-deforming tissue from respiration, the mechanical properties of CC are critical for maintaining their structural health and delivering their physiological function. According to the biological background, the peripheral region differs in structure and functions from the interior region, and the mechanical properties at the CC exterior surface influence diffusion of oxygen and nutrients and thus are intrinsic to maintaining their structural characteristics. However, very limited knowledge exists on the mechanical properties of peripheral CC, due to their highly irregular geometries. To date, to obtain regular geometries for measurement, CC were cut into strips along the cartilage length and disks along the

transverse direction. CC strips were measured using uniaxial tension/compression [3, 17, 22, 25] flexural testing [17, 22]. CC disks were measured on the cleaved transverse cross-section using rigid spherical indenters [1, 4, 27, 28, 37]. These pioneering studies have established that mechanical properties of human CC vary along their length [4] and show a link with aging and gender [1, 3]. Only one study examined the mechanical behavior of human PE CC and found a weakened biomechanical stability of PE CC as compared with control CC [17]. To the best knowledge of the authors, no mechanical studies on human PC CC have yet been reported in the literature. However, the peripheral region is removed in CC strips and thus their measured results do not reveal the mechanical properties of CC in its peripheral region; indentation on the cleaved transverse cross-section of CC disks does not examine the mechanical properties of CC at their exterior surface. The CC retain a heterogeneous structure at transverse cross-section and a curved centerline along their length, so any variation in strip and disk preparation (e.g., sample axis not aligned with the cartilage centerline) will translate to significant measurement errors. The curved exterior surface of CC rules out using indentation via rigid indenters for their measurement, simply because non-conformity of a rigid indenter to the curved surface causes a varying constant contact area during indentation, which yields significant errors in the measured mechanical properties of CC [38, 39]. Moreover, the nanoindentation technique is even lacking the effect of physiological loading.

1.4. Objective

This dissertation is aimed to determine the mechanical properties at the exterior surface of CC and examine how they vary with the cartilage length and the anatomical sites of CC in the ribcage via conformal indentation testing which is employed by a tactile sensor for distributed-deflection detection. By using this novel testing method, CC experiences compressive

loading at its exterior surface in vivo and retains its structural integrity.

1.5. Dissertation Layout

Chapter Two presents the polymer-based microfluidic resistive tactile sensor without a built-in probe employed in this study for detecting distributed normal loads. The working principle, fabrication protocols, and its performance characterization are presented in detail. Technical issues associated with the sensor are also discussed.

Chapter Three introduces a built-in probe to the current polymer-based microfluidic resistive tactile sensor and investigated the feasibility of using this sensor with the built-in probe for conformal mechanical measurements of CC at its exterior surface. The theoretical model, qualitative analysis, numerical study, performance characterization, and data analysis method are presented, respectively.

Chapter Four presents the implementation of using the sensor with a built-in probe to measure the mechanical properties at the exterior surface of porcine CC. The measured results are presented and compared with those in the literature. The relation between the measured mechanical properties and the anatomical sites of CC in the ribcage is discussed as well.

Chapter Five presents the implementation of using the sensor with a built-in probe to measure the mechanical properties at the exterior surface of human PC CC. The testing results are not only compared with those in the literature but also compared the measured results of porcine CC in Chapter Four.

Finally, Chapter Six discusses the advantages and drawbacks of using the sensor with a built-in probe to test the mechanical properties of CC at its exterior surface and proposes future work that can be built upon this dissertation.

CHAPTER 2

A POLYMER-BASED TACTILE SENSOR WITH A BUILT-IN PROBE FOR DISTRIBUTED-DEFLECTION DETECTION

This chapter depicts a previous designed polymer-based microfluidic resistive tactile sensor without a built-in probe employed in this study for detecting distributed normal loads. The core of the sensor is a polymer rectangular microstructure embedded with distributed resistive transducers underneath. Together with five electrode pairs, one body of electrolyte in the microchannel functions as five distributed resistive transducers. The microstructure converts distributed normal loads to continuous deflection, which register as discrete resistance changes at the locations of the distributed transducers. Since the detailed design, fabrication, and characterization process of the sensor have been presented in the previous work [40-42]. A brief description of the sensor is given in this chapter for completeness. Following is the working principle, fabrication details, sensor characterization, and technical issues associated with this tactile sensor before adding a built-in probe are elaborated in the rest of the chapter. Due to the study duration of this dissertation, three sensors with identical design are used. The sensor used in this measurement is labeled as sensor A.

2.1. Work Principle

Figure 2.1 shows the basic configuration of the polymer-based microfluidic resistive tactile sensor for distributed-deflection detection. The tactile sensor consists of a rectangular polymer microstructure embedded with an electrolyte-filled microchannel and five electrode pairs distributed along the microchannel length. Together with the electrode pairs, one body of electrolyte in the microchannel functions as five distributed resistive transducers. Each transducer can record the resistance of the portion of an electrolyte between the two opposing

electrodes across the microchannel width. The reservoirs at each end of the microchannel are utilized to fill the microchannel with an electrolyte and provide a conduit for electrolyte to flow in/out during the sensor operation. Thus, adding the reservoirs not only completely confines electrolyte within the sensor, but also allows electrolyte to freely flow during the sensor operation. PDMS is chosen as the structural material, due to its low elastic modulus and great fabrication simplicity. The ionic liquid 1-ethyl-3-methylimidazolium dicyanamide (EMIDCA) with a 98% concentration is selected as the electrolyte filling in the microchannel for its stability, low volatility, and a relatively high conductivity compared to its counterparts, which are NaCl and KCl solutions, used in previous research [40-42].

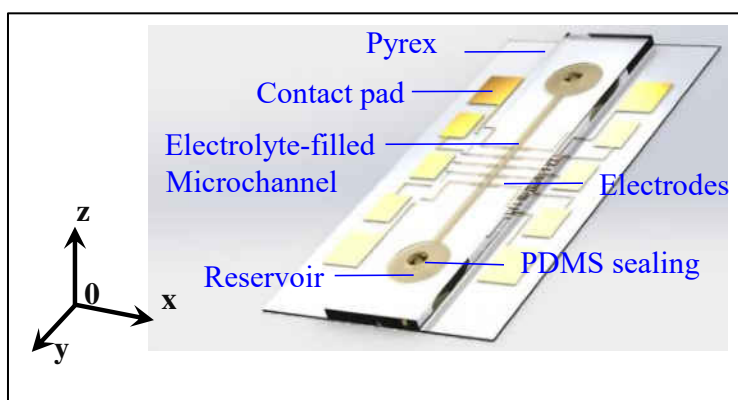


Figure 2.1 Schematic of the experimental setup for nanoindentation of porcine costal cartilage.

To better illustrate how controlled displacement is converted to recordable resistance changes at the transducer locations, the rationale of the tactile sensor is demonstrated in Figure 2.2. While the microstructure converts continuous distributed loads to continuous deflection along its length (y -axis), the distributed transducers translate the continuous deflection to discrete resistance changes at specific locations along the microstructure length. To avoid spillover of the electrolyte during the sensor operation, two reservoirs are sealed by PDMS after electrolyte injection. The key parameters and their values of the tactile sensor in this work are labeled in Figure 2.3 and listed in Table 2.1 respectively.

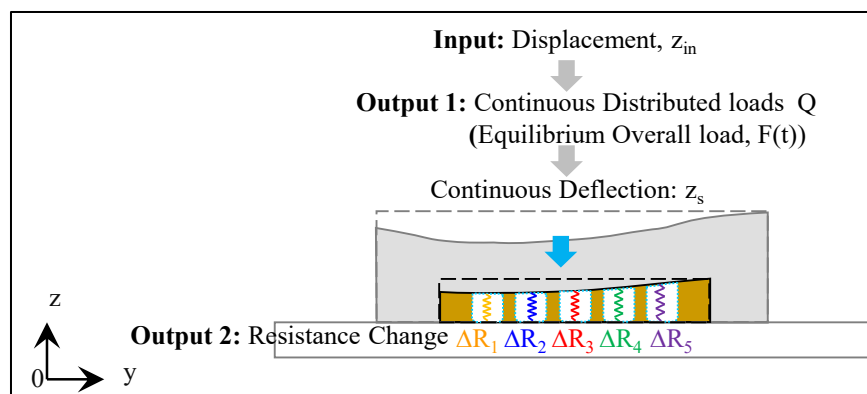
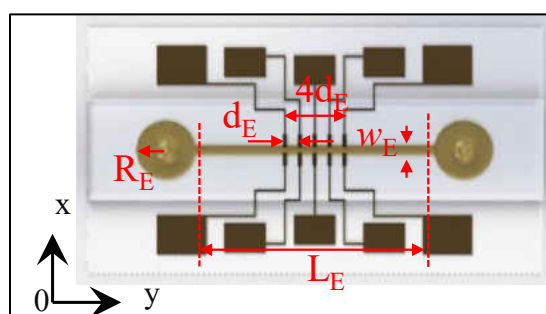
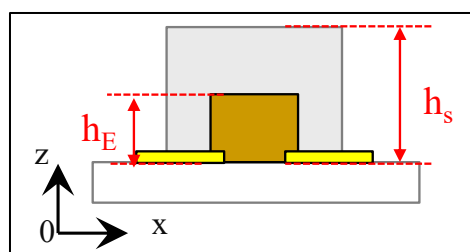


Figure 2.2 Working principle of the tactile sensor.



(a)



(b)

Figure 2.3 Key design parameters of the polymer-based microfluidic tactile sensor: (a) top view; (b) side view.

Table 2.1 Key design parameters of the polymer-based microfluidic tactile sensor.

Key parameters	Values	Symbol
Microchannel cross-section	0.5mm×80μm	$w_E \times h_E$
Microchannel length	12mm	L_E
Reservoir radius	1.5mm	R_E
Spatial resolution of transducers	0.75mm	d_E
Microstructure thickness	1mm	h_s
Microstructure Elasticity	700kPa	E_s

The electrodes on one side are connected to a function generator, while the electrodes on the other side are connected to the circuits that amplify the signals and convert them to DC output. The sensor essentially has both a capacitive and a resistive nature. The capacitive nature is mainly from the double layer effect formed by the electrode-electrolyte interface. However, with the highly conductive electrolyte EMIDCA, the entire sensor can be treated as resistive dominant when the passing signal is at high frequencies (>100 kHz), since at high frequencies the capacitor is treated as a wire [41, 43-45]. In addition, DC voltage will cause severe electrolysis and damage the deposited electrodes. In this work, the voltage of the AC signal is kept around 120 mV, since low voltage magnitude helps prevent the hydrolysis of the electrolyte. Each opposing pair of electrodes can record the voltage on the electrolyte portion at its corresponding location. Deflection of the PDMS structure causes a corresponding resistance change of the electrolyte in the microchannel and is recorded as a change in the output DC voltage. A sensor characterization has to be carried out for obtaining the relation between the voltage output and the mechanical input before conducting any measurement on material samples. Once this relation is established, the deformation of the PDMS microstructure at the locations of the transducers can be deduced from the change in the voltage output. A simultaneous spatial measurement thus becomes feasible.

The mechanical input for sensor characterization is applied by a rigid cylindrical probe with a diameter of 0.8mm and length of 6mm, as can be seen in Figure 2.4. The cylindrical probe is aligned along the microchannel length and provides a regional deformation above the microchannel, leaving the rest of the sensor or the rest region of the material, under test minimally affected by the applied load. However, due to the cylindrical shape, misalignment of the probe about its own axis is alleviated.

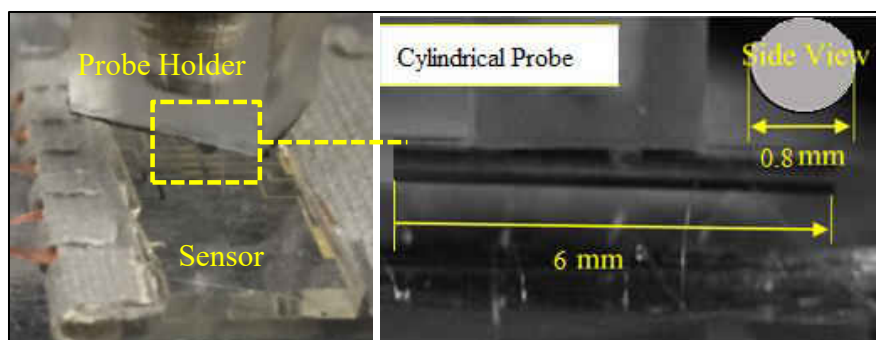


Figure 2.4 Key dimensions of a rigid cylindrical probe for sensor characterization.

2.2. Fabrication Process

A standard two-mask fabrication process as shown in Figure 2.5 for the sensor, one mask is for patterning electrodes on a Pyrex slide and the other one is for forming SU8 mold and translates to PDMS microstructure later by soft lithography. The main steps for this two-mask fabrication process can be summarized as: photolithography and sputtering for electronics pattern, soft lithography for PDMS microstructure and bonding. Before the main steps, all the Pyrex slides used in the fabrication process should be first cleaned by Potassium hydroxide (KOH) and acetone bath in an ultrasonic cleaner for 10min, respectively, and then rinsed with isopropyl alcohol and DI water, and dried with Nitrogen gas later on.

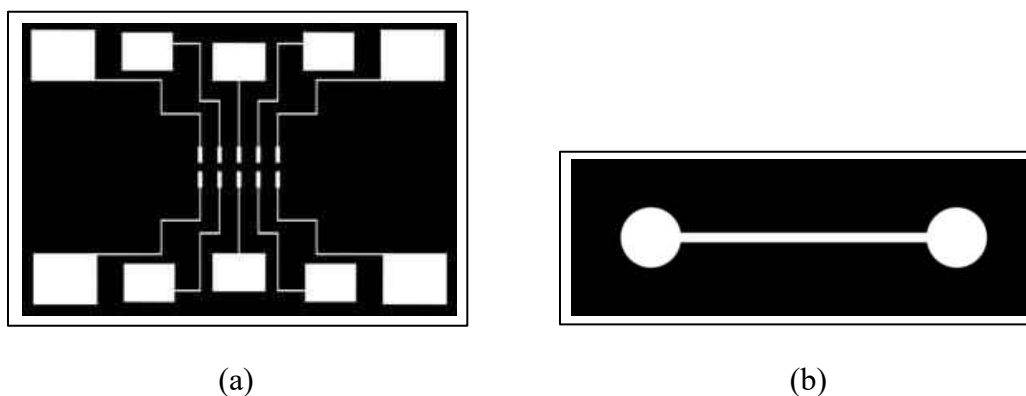
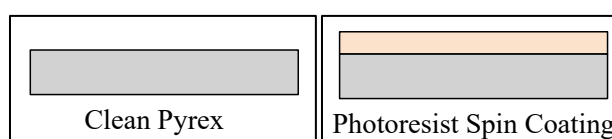


Figure 2.5 Mask design for (a) the microchannel and (b) the patterned electrodes.

2.2.1. Photolithography and sputtering for electrodes pattern

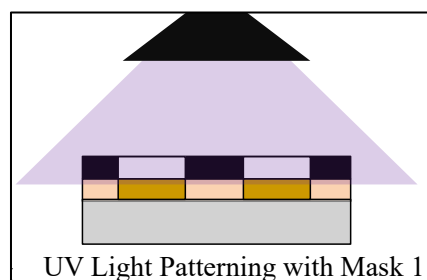
First of all, the electrodes with the desired pattern are in AutoCad® and later were

printed on a polyester film as a transparent region, as illustrated in Figure 2.5 (a). Please note, the undesired region remains black. Then, as illustrated in Figure 2.6, after pre-baking the clean Pyrex for 3-5 minutes at 90°C, the photoresist material S1800 or S1805 is spin coated on the Pyrex side, at 500 rpm for 10 seconds and 2000 rpm for 30 seconds and dehydrated on a hot plate at 90°C for another 1 minute. S1800 and S1805 are positive photoresistive material that eventually leaves the part not exposed to UV light on the Pyrex slide. Thus, following the soft bake, the Pyrex slide covered with the electrodes mask is placed under an Exoteric 405 nm h-line UV Flood Source and exposed to h-line UV with exposure intensity of 11.74mW/cm² for 5 seconds. In the successive step, the coated Pyrex is developed in MF-24 till the pattern is neat and clear, rinsed in Di water, and dried with Nitrogen gas later on. Then the developed Pyrex is placed in a sputter coater (300TD, Electron Microscopy Sciences) for depositing 10 nm Cr and 100 nm Au and soaked in an ultrasonic acetone bath for undesired Au/Cr removal, which is also called a lift-up process. After an indispensable cleaning process, including isopropyl alcohol rinsing, Di water rinsing and Nitrogen gas dry, Pyrex with patterned electrodes is finally obtained.



(a)

(b)



(c)

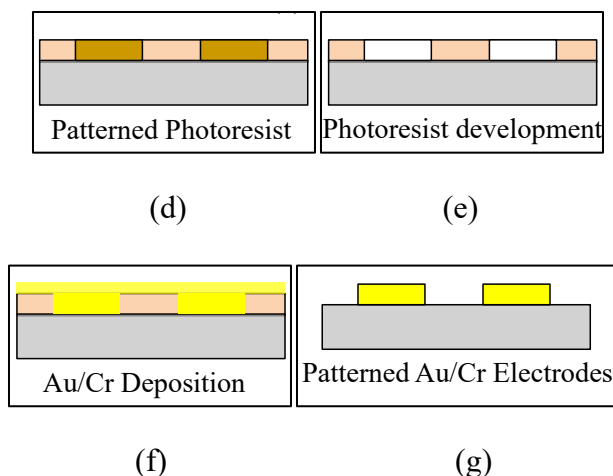


Figure 2.6 Fabrication process for patterning electrodes on Pyrex substrate: (a) Pyrex cleaning; (b) Photoresist spin coating; (c) UV light patterning with Mask 1; (d) Pyrex with patterned photoresist; (e) Photoresist development in MF-24; (f) Au/Cr deposition; (g) Succeed electrodes.

2.2.2. Soft lithography for PDMS microstructure

The PDMS microstructure is fabricated by a soft lithography process. First, to make the mold for the microchannel, a photoresist material SU-8 50 is first spin-coated to a Pyrex slide to form a uniform thin layer. SU-8 is a commonly used epoxy-based negative photoresist that can be used to pattern high aspect ratio structures. It can be spun over a thickness ranging from below 1 μm to more than 300 μm before proceeding to photolithography. After pouring SU-8 on the Pyrex slide, it is followed by a five-second spin coating at 500 rpm and a 30-second spin coating at 1500 rpm. Then, the slide is baked at 65°C for 10 minutes and 95°C for 30 minutes. After that, the Pyrex slide with an 80 μm thick SU-8 layer is ready for exposure.

By using the similar photolithography process as Au/Cr electrodes, the Pyrex slide with SU-8 is then brought to an ultraviolet (UV) light with the microchannel mask mounted (Figure 2.5 (b)) on it. Since SU-8 is a negative photoresist material, the part exposed to the UV light is left on the Pyrex slide. In this case, an i-line Karl Suss MJB3 mask aligner is applied to expose the slide for 8 seconds at the exposure intensity of 30mW·cm⁻² and ensure the exposure energy at 240mJ·cm⁻² for 80 μm thick SU-8 layer. This is followed by a 1 minute post-exposure

bake(PEB) #1 at 65°C, a 10 minute PEB #2 at 95°C, and a 5-minute development by an SU-8 developer. Then, the Pyrex slide with the SU-8 mold is cleaned with isopropyl alcohol and DI water. After drying the slide, the SU-8 mold with the pattern of an 80 μ m thick microchannel is ready to use, as shown in Figure 2.7. Figure 2.7 clarifies a soft lithography fabrication process used to form the PDMS microstructure in this study. Basically, a 1:10 ratio of curing agent to PDMS elastomer is poured over the SU8 mold and cured to form the PDMS microstructure for 24 hours at room temperature on the optical table to ensure an even thickness. The thickness of the PDMS microstructure is adjusted by the amount of mixture being poured into the mold. The cured PDMS microstructure is peeled off from the SU8 mold. A needle with an inner diameter of 1mm is used to punch a hole into each reservoir for injecting electrolyte into the microchannel later on.

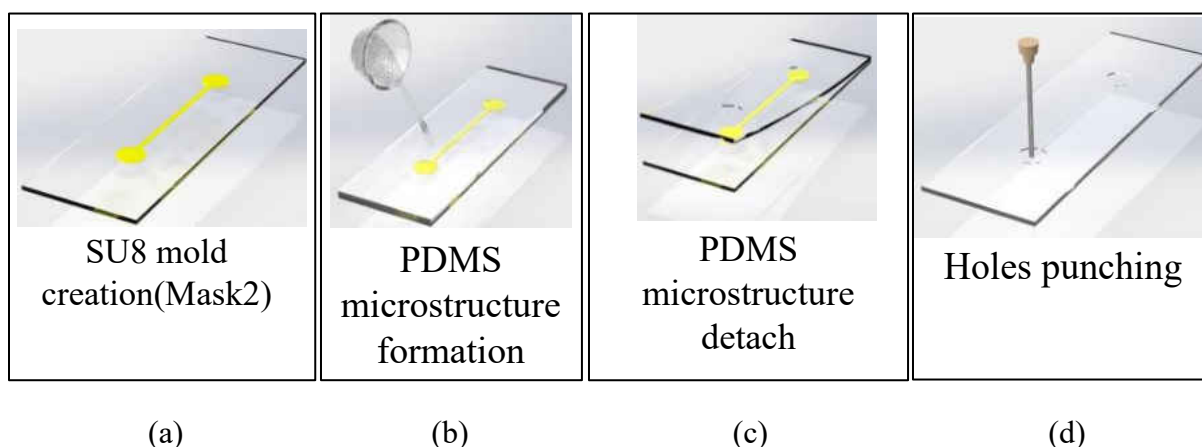


Figure 2.7 Soft lithography on PDMS microstructure: (a) SU8 mold creation by microchannel shape mask; (b) PDMS microstructure formation; (c) PDMS microstructure detach; (d) Holes punching.

2.2.3. Bonding

First of all, to ensure the efficiency of oxygen plasma deposition, both Pyrex with patterned electrodes and PDMS microstructure need to be soaked and cleaned by an ethanol bath in ultrasonic for 10 minutes, and rinsed by Di water. After the essential drying method by

Nitrogen gas, both electrodes Pyrex and PDMS layer are dehydrated at 130 °C for 5 minutes with both electrodes side and microchannel side facing upwards. Then, after oxygen plasma treatment on both electrodes side and microchannel side, the two layers are aligned and bonded under an optical microscope. Finally, 1-ethyl-3-methylimidazolium tricyanomethanide (EMIM TCM) is used as the electrolyte for the sensor and is injected into the microchannel via a syringe. Furthermore, to avoid electrolyte spillover during the sensor operation, one drop of 1:10 PDMS mixture is placed on the top of each reservoir to cover the pouched hole. Electrical connection is made to the sensor by gluing wires to the Au/Cr contact pads with conductive epoxy (8331, RoHS compliant). The final finished tactile sensor is shown in Figure 2.8.

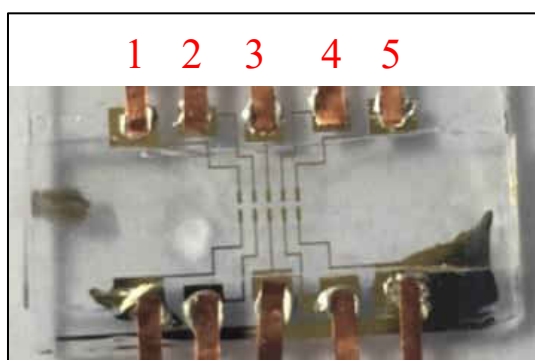


Figure 2.8 Fabricated microfluidic tactile sensor with electrolyte in the microchannel. The transducers are labeled by numbers.

2.3. Performance Characterization

Two types of sensor performance tests are carried out on this tactile sensor. One measurement is characterized by a rigid cylindrical probe aligned along the microchannel to press against the top of the PDMS structure which is above the microchannel. Another one is carried out on the exterior surface of a human PC CC to see the feasibility of extracting the mechanical properties of the CC. The detail experiment setup, method, data analysis method, and corresponding results are presented below. Due to the study duration of this dissertation, three sensors with identical design are used. The sensor used in this measurement is labeled as

sensor #A.

2.3.1. Experiment method of the sensor characterization with a rigid probe

2.3.1.1. Experiment setup

The experimental setup is illustrated in Figure 2.9. The tactile sensor is fixed on a printed circuit board (PCB) and is bonded with wires for electrical connection. Then, the PCB with a wire-bonded sensor is mounted on a 5-axis manipulator located on an optical table. A function generator is used to apply an AC voltage to the inputs of the transducers of the sensor and the output of each transducer is connected to its own dedicated electronics on a PCB for converting an AC current from a transducer to a DC voltage signal, which feeds in a DAQ board (NI PCIe-6363) and is further recorded by a custom LabVIEW program.

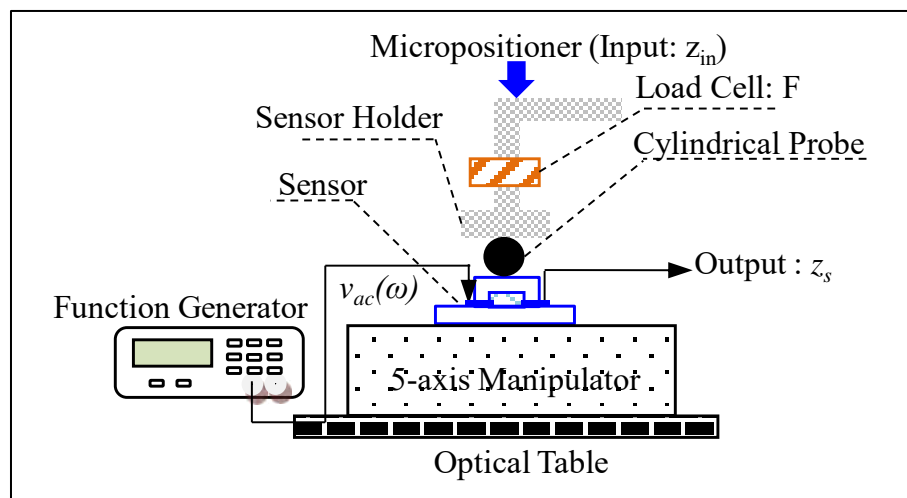


Figure 2.9 Experiment setup for sensor without a built-in probe characterization.

To exert a distributed displacement on the sensor, a rigid cylinder probe with 0.4 mm in radius and 6mm in length and a six-axis force/torque sensor (Nano17, ATI Industrial Automation) are incorporated together with a micropositioner. The six-axis force/torque sensor here is to record the overall force/torque experienced by our tactile sensor. The cylinder probe is utilized to exert precisely controlled indentation depths on the top of the tactile sensor. The 5-

axis manipulator is used to better align the cylinder probe in parallel to the sample surface so that the sample experiences the same indentation depth from the probe at the locations of all the transducers.

Prior to the testing of the sensor, the probe is manually aligned to the top of the microchannel. The 5-axis manipulator is then manually adjusted to better align to probe in parallel with the microchannel length. Afterward, the probe moves against the sensor with a pre-defined displacement pattern. The outputs of the sensor and the readout of the load cell are recorded. Note that the change of a transducer is calculated as the difference between its resistance measured at a displacement input and the initial resistance, which is measured right after the probe being aligned but prior to a displacement input.

2.3.1.2.Experiment method

Step 1: Determination of the contact point of the probe with sensor top

The probe is brought down to a visible distance above the sensor top. Then, the probe is brought down by an interval of $10\mu\text{m}$ using the micropositioner at a time until a noticeable change in the readout of the load cell is observed and recorded in a LabVIEW program. Afterwards, the probe is moved back by $10\mu\text{m}$. At this point, the probe is assumed to be in contact with the top of the sensor, while not deforming the sensor. Thus, there might be a gap of $\sim 10\mu\text{m}$ between the probe and the sensor top.

Step 2: Indentation measurement

By using the micropositioner, the probe exerts an indentation step, $z_{step}=20\mu\text{m}$, on the sensor top above the microchannel at a ramp speed of $1\text{mm}\cdot\text{s}^{-1}$. At the instant the probe reaches its final location, the readout of the load cell is recorded. The holds time, t_{hold} , is 5s for the indentation. This hold time, t_{hold} , allows the microstructure to relax to a great extent [46]. The

readout of the load cell is recorded again at the end of the $t_{hold}=5s$ hold time. The DC outputs of the sensor corresponding to the start and end of the 5s hold time are also recorded (note: the readout of the load cell and the DC voltage outputs of the sensor are recorded with a sampling rate of 500Hz for the entire hold time. However, only the values at the start and the end of the 5s hold time are used for data analysis later on). Then, the probe is brought down to exert another indentation of $20\mu m$ ($z_{step}=20\mu m$) on the microchannel top at the same ramp speed as before. After the same parameters are recorded at the start and end of the same 5s hold time, the probe is brought back to the contact point at the same speed. This procedure is repeated for 20 times with an indentation depth increment of $20\mu m$ each time until the final indentation depth reaches $400\mu m$. Therefore, multiple $F-z_{in}$ data points at the start and end of a 5s hold time, respectively, at different indentation depths are recorded for this sensor characterization.

The indentation pattern is illustrated in a schematic as Figure 2.10. In brief, the indentation step, z_{step} , final indentation depth, holds time, t_{hold} , and ramp speed are $20\mu m$, $400\mu m$, 5s, $1mm\cdot s^{-1}$, respectively. This indentation measurement is repeated three times for error elimination.

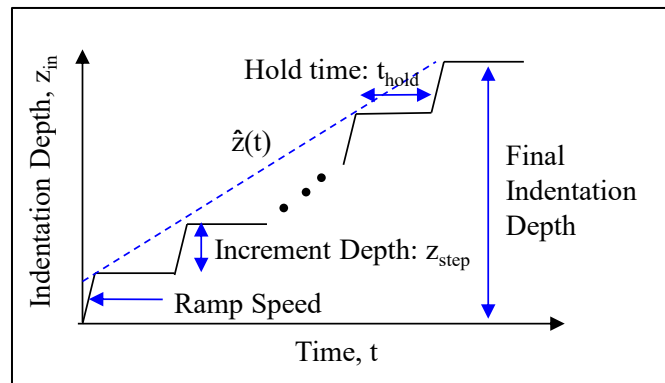


Figure 2.10 Key parameters for the patterns of indentation depth in sensor characterization.

2.3.2. Experiment method of the sensor performance characterization by CC measurement

2.3.2.1. Sample Preparation

A human PC CC is chosen to fulfill this measurement and label as CC#1. This human CC was obtained from the ribs of the lower thoracic region of a 17 yr-old male patient at Children's Hospital of The King's Daughters (CHKD), Norfolk, VA. Prior to removal of the cartilage tissues, patient consent was obtained with full IRB approval. Figure 2.11 shows the CC#1 from a 17yr-old male patient. This sample was measured after being stored at -20°C for some time, because the testing setup was not ready at the time it was removed from the patient. The indentation measurement is carried out once at both anterior and posterior surface.

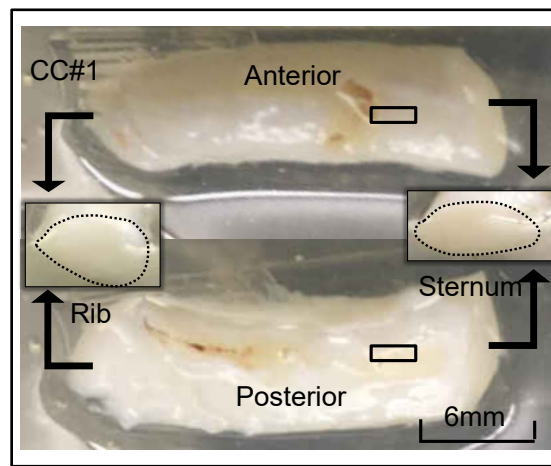


Figure 2.11 Pictures of human PC CC#1 sample with measured locations. (Black blocks and arrows on the cross sections of the samples indicate the locations of the probe in measurement; and left side: toward the rib, right side: toward the sternum)

2.3.2.2. Experiment setup

Figure 2.12 depicts the experimental setup for characterizing the sensor performance on CC measurement. The whole experimental setup is implemented on an optical table. During the measurement, a sensor and a 6-axis load cell mentioned above are assembled together by a probe holder, which is connected to a 3 degree of freedom (DOF) micro-positioner. Electrical connection is made to the sensor by gluing wires to the contact pads via silver conductive epoxy adhesive still. A specimen holder with a half cylinder hole is fixed on a 5-axis manipulator. The CC segment is placed right in the half cylinder shaped mold for preventing it from moving and

soaked in the PBS solution for keeping it in an aqueous condition during the operation. Afterwards, the sensor is manually brought right above a CC segment. The 5-axial manipulator is utilized to better align the microchannel of the sensor in parallel to the specimen surface so that the specimen experiences the same pre-defined displacement at the locations of all the transducers. The sensor can exert precisely-controlled displacements along the z-axis on a specimen through the micro-positioner. The 6-axis load cell here is optional and is used for the overall load verification.

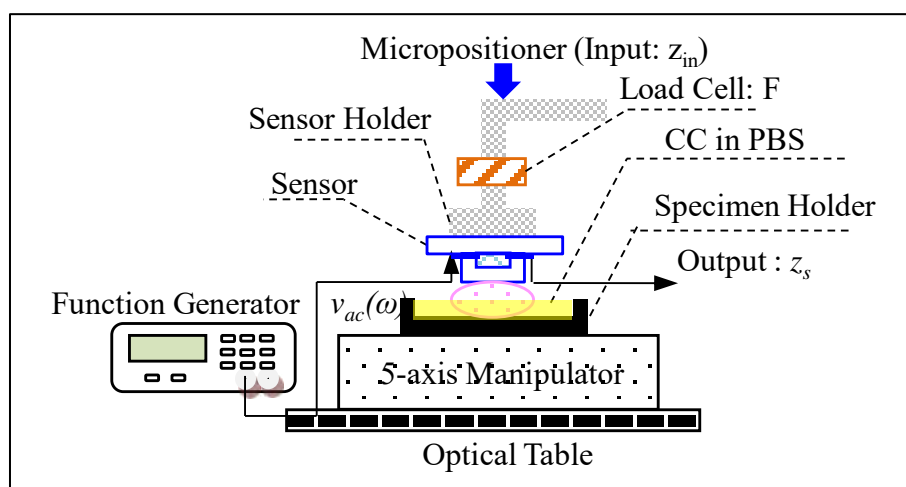


Figure 2.12 Experiment setup for sensor performance on CC measurement.

2.3.2.3. Experiment method

Step 1: Determination of the contact point of the probe with sensor top

Similarly, the sensor is brought down to a visible distance above the CC top. Then, the sensor is brought down by an interval of $20\mu\text{m}$ using the micropositioner at a time until a noticeable change in the readout of the load cell is observed and recorded in a LabVIEW program. Afterwards, the sensor is moved back by $20\mu\text{m}$. At this point, the sensor top is assumed to be in contact with the highest location of the CC top, while not deforming the sensor and tissue. Thus, there might be a gap of $<20\mu\text{m}$ between the sensor top and the highest location of

CC specimen.

Step 2: Indentation measurement

The indentation pattern can also be presented by Figure 2.10. In brief, the sensor is brought down an incremental indentation depth of $z_{step}=100\mu\text{m}$ from the contact point each time with a ramp speed of $1\text{ mm}\cdot\text{s}^{-1}$ and a $t_{hold}=20\text{s}$ hold time until reaching the final indentation depth of $z_{in}=1\text{mm}$. The corresponding sensor deflections at each indentation depth are acquired by the sensor via the LabVIEW program.

CC #1 was measured three times with a 30min recovery time in between. The first measurement on both locations differed dramatically from the following two measurements, indicating that a CC tissue in vitro loses capability of full recovery. Similar observations were also reported in the literature [47]. As such, the measured results of the first measurement was adopted.

2.3.3. Theoretical Analysis

From a mechanical perspective, the force exerted on the polymer structure causes deflection as clarified in Figure 2.2. The force and sensor deflection relation can be expressed using a linear expression:

$$F = k_s \cdot z_s \quad (2.1)$$

where k_s means the sensor stiffness, and z_s represents the displacement applied by a probe on the top surface of the sensor. In the later analysis, z_s should equal to the indentation depth z_{in} .

From an electrical perspective, the circuits include a demodulation stage and a transimpedance amplifier. The AC signal from the sensor output can be amplified and converted to a steady DC output, which can be calculated as:

$$V_{out-i} = \frac{V_{pp}^2 \cdot R_F^2}{8 \cdot R_i^2(z_s)} \quad (2.2)$$

In the Equation 2.2, V_{pp} represents the peak to peak value of the AC voltage that is applied to this sensor; R_F is the feedback resistor with a known resistance value, 25 kΩ in this study. $R_i(z_s)$ is the resistance value of the i^{th} transducer. The circuit diagram and the derivation of Equation 2.2 are presented in Appendix. The peak to peak value of the AC voltage, V_{pp} is pre-set as 120mV. The DC voltage output is recorded by the LabVIEW program. As such, the resistance value of the i^{th} transducer $R_i(z_s)$ can be derived as

$$R_i(z_{s-i}) = \frac{V_{pp} \cdot R_F}{2\sqrt{2V_{out-i}}} \quad (2.3)$$

Thus, in response to the distributed deflections of the microstructure, the resistance change, ΔR_i , of the i^{th} transducer array is:

$$\Delta R_i(z_{s-i}) = R_i(z_{s-i}) - R_{0i} \quad (2.4)$$

where R_{0i} denotes the initial resistance of the i^{th} transducer after a probe is aligned on the sensor but prior to a measurement.

Since the resistance change of i^{th} transducer pairs, $\Delta R_i(z_{s-i})$, is obtained as the function of the top deflection of the sensor z_{s-i} which equals to the indentation displacement z_{in} in the sensor characterization with a rigid probe. However, in the sensor characterization on CC measurement, the relation between the indentation displacement z_{in} and the top deflection of the sensor z_s is expressed as

$$z_{in} = z_s + z_t \quad (2.5)$$

where z_t denotes as the tissue deflection in the CC measurement. The relation between resistance change, $\Delta R_i(z_{s-i})$ and the top deflection of the sensor, z_{s-i} , can be extracted by the sensor characterization by a rigid probe. The indentation depth, z_{in} follows a pre-defined pattern. As such, after an evaluation of the resistance change value, $\Delta R_i(z_{s-i})$ in the CC measurement, the top deflection of the sensor, z_{s-i} can be monitored and considered as known. The corresponding tissue deflection in CC measurement can be calculated by the difference of indentation depth and top deflection of the sensor:

$$z_t = z_{in} - z_s \quad (2.6)$$

2.3.4. Results

2.3.4.1. Results of the sensor characterization with a rigid probe

As shown in Figure 2.13, the sensor exhibits a linear load-deflection relation and thus, is capable of capturing the indentation behavior. Here, F means the force exerted on the polymer structure; k_s is the sensor stiffness; z_s is the top deflection of the tactile sensor. The three repeated indentation measurements show almost the same trend which indicates the robust feature of the sensor and can be used over a long-duration with almost no change in mechanical behavior. Additionally, the sensor stiffness, k_s equals to $1720 \text{ N}\cdot\text{m}^{-1}$.

Figure 2.14 depicts the relation between the resistance change, ΔR and top deflection of the tactile sensor, z_s . The average value of the resistance change, ΔR and the sensor deflection z_s of three identical measurements are used for extracting their relation in Figure 2.14. The standard deviation indicates the variation of the value of resistance change among the three measurements. As can be seen, the standard deviation is very small and further proves the robust feature of this sensor. Additionally, it shows the resistance change slightly varies among the transducers, owing this to fabrication variation and probe misalignment problems as discussed in

the Section 2.4. The slope of $\Delta R \sim z_s$ relations in Figure 2.14 are $375 \text{ k}\Omega \cdot \text{m}^{-1}$, $770 \text{ k}\Omega \cdot \text{m}^{-1}$, $1052 \text{ k}\Omega \cdot \text{m}^{-1}$, $932 \text{ k}\Omega \cdot \text{m}^{-1}$ and $1095 \text{ k}\Omega \cdot \text{m}^{-1}$, respectively.

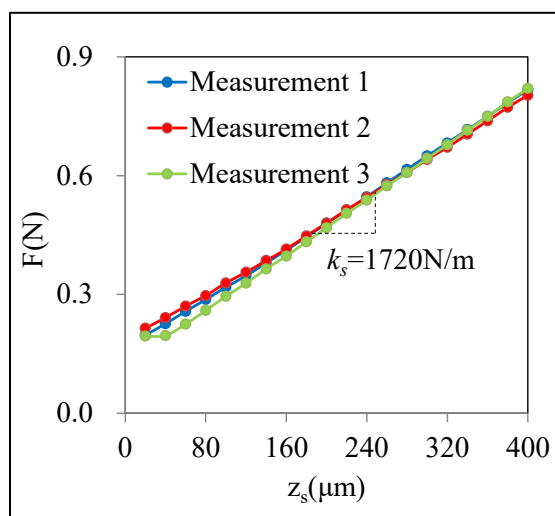


Figure 2.13 Force-deflection relation of the tactile sensor characterization with a rigid probe. Measurement represents the three repeated indentation measurement.

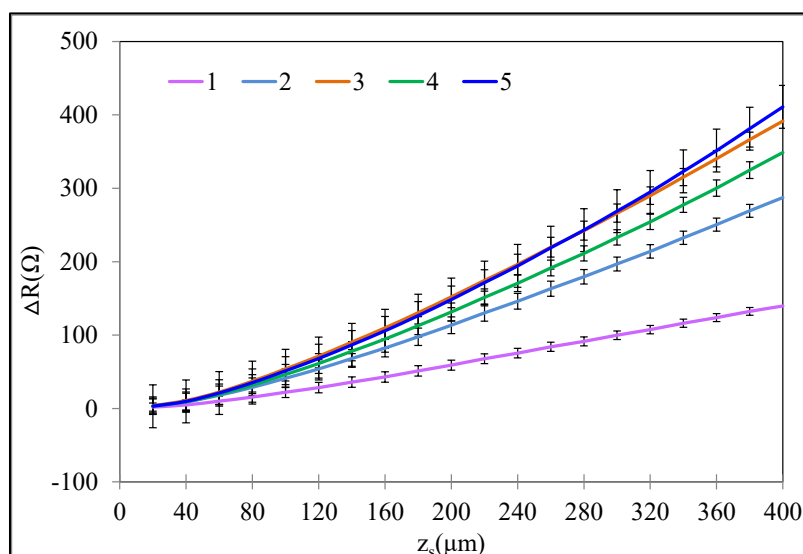


Figure 2.14 Relation of average resistance change ΔR and average top deflection of the tactile sensor, z_s of three identical measurements. (1-5: sensor deflections at transducer 1-5). The standard deviation denotes to the robust feature of the tactile sensor.

2.3.4.2. Results of the sensor performance characterization by CC measurement

Figure 2.15 illustrates the spatially distributed sensor deflection as a function of indentation depth of CC #1 at its anterior and posterior surfaces from their first measurements.

The sensor deflection varies dramatically among the locations of the transducers; the sensor deflection abruptly varies with the indentation depth; and the relaxed sensor deflection does not follow the instant sensor deflection at some transducers. This is believed to arise from the fact that, other than the sensing-plate, the surrounding region of the microstructure comes in contact with the cartilage exterior surface, causing a random change in contact area and lateral force on the sensing-plate over the indentation depth range. As shown in Figs. 3(a), the CC specimen possesses not only curved shape but also extrusions at its exterior surface. The severity of raggedness in the measured deflection-depth (z_s - z_{in}) relation indicates the interference of extrusions in these measurements and sensor limit of capturing the true mechanical properties of CC with curved surface.

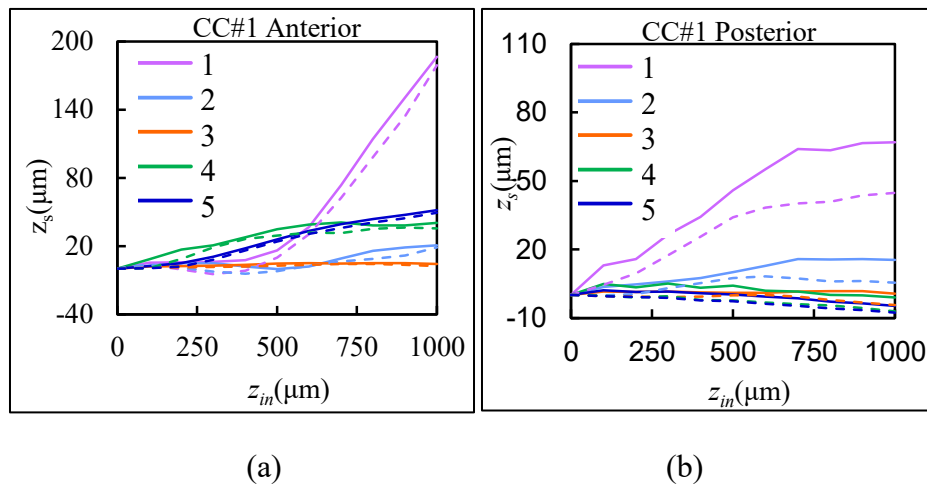


Figure 2.15. The spatially distributed sensor deflection, z_s as a function of indentation depth z_{in} on CC #1 using the tactile sensor (solid line: instant values; dashed line: relaxed values) (a) anterior surface (b) posterior surface (1-5: sensor deflections at transducer 1-5)

2.4. Technical Issues Encountered

Three technical issues associated with the tactile sensor itself and the performance characterization are discussed in this section, including fabrication variation, probe misalignment, and the curved surface of CC specimen.

2.4.1. Fabrication variation

Fabrication variations are other issues that affect the sensor performance. The main leading reasons of fabrication variation are the microchannel height and the electrodes resistances. Since the microchannel height has the smallest dimension among all the key design parameters of the sensor, a slight non-uniformity of the microchannel height could significantly affect the voltage output from the sensor. As demonstrated in the fabrication process (Section 2.2.2), the microchannel height is determined by the thickness of the SU-8 mold via a soft lithography process. It is impossible to maintain the SU-8 height perfect uniformity without slight variations. Moreover, the detach process of PDMS microstructure would also cause the variation of microchannel height. Another reason is resistance variation among the patterned electrodes, since it is inevitable that the photolithography and sputtering process would cause the thickness of the Au/Cr electrodes layer has some variations.

2.4.2. Probe misalignment

Misalignment of the probe will bring in an initial uneven microchannel top deformation and affects the voltage output of the sensor. There are three types of misalignment existing in this one-dimension microfluidic tactile sensor, including z-direction misalignment, x-y in plane misalignment, and axial misalignment. The rigid probe is a cylindrical size which will not affect the voltage output about the y-axis (axial misalignment) as clarified in Figure 2.16. The other two types of misalignment play a critical role in affecting the voltage output of the sensor.

Figure 2.17 schematically illustrates the z-direction misalignment of the probe. In this case, the probe is well aligned along the microchannel length (y-axis). However, the probe tilts towards on end of the microchannel on the z-direction, which leads the top of the microchannel to have non-uniform deflections. Luckily, z-direction misalignment can be detected by observing

the increasing or decreasing trend of voltage output and the transducers' responding sequence.

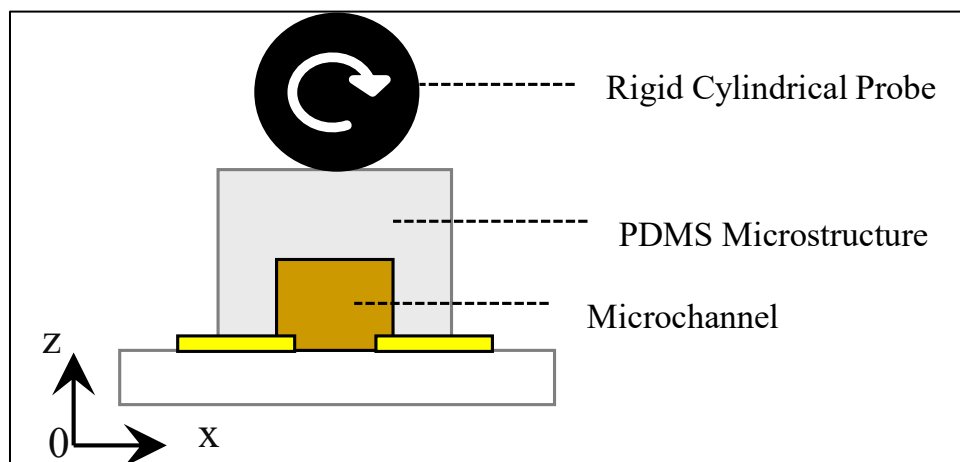


Figure 2.16. Schematic of the misalignment about the x-axis. (x-z side view)

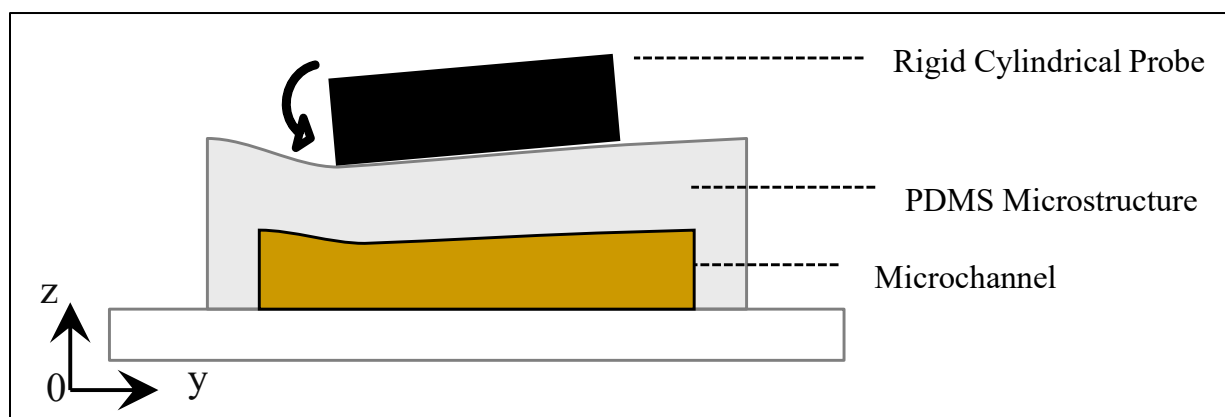


Figure 2.17. Schematic of the z-direction misalignment. (y-z side view)

Figure 2.18 demonstrates the x-y in-plane misalignment. In this case, the probe does not perfectly cover the microchannel top, and rotates about the z-axis by several degrees. The effect of the x-y in-plane misalignment is similar to the z-direction misalignment and will cause the non-uniformity deformation of the microchannel, which will further cause the variations in the voltage outputs among the transducers. This type of misalignment can lead to the increasing or decreasing trend of voltage output as well, but the response time of the transducers should be the same.

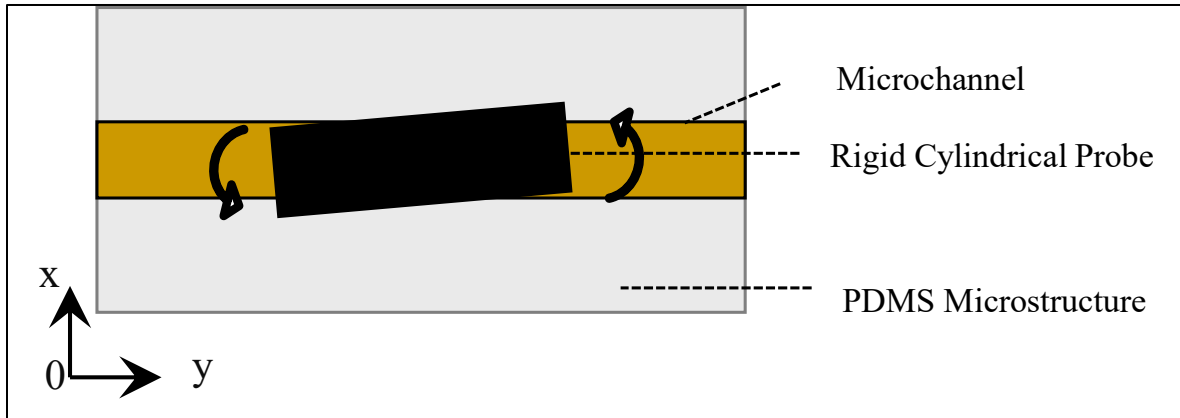


Figure 2.18. Schematic of the x-y in-plane misalignment. (x-y top view)

2.4.3. Curved surface of CC specimen

The interaction between the tactile sensor and a curved tissue surface is depicted in Figure 2.19. Since the sensing-plate and its surrounding region of the microstructure are on the same plane, the surrounding region will interfere with the interaction between the sensing-plate and the tissue. For instance, any relatively large extrusions and curved shape at the cartilage exterior surface may interact with the surrounding region of the microstructure, thus either preventing full contact of the sensing-plate with the tissue surface or causing lateral loading to the sensing-plate. Such non-full contact of the sensor with a tissue surface and lateral loading introduces significant errors in the measured results, as will be seen later on.

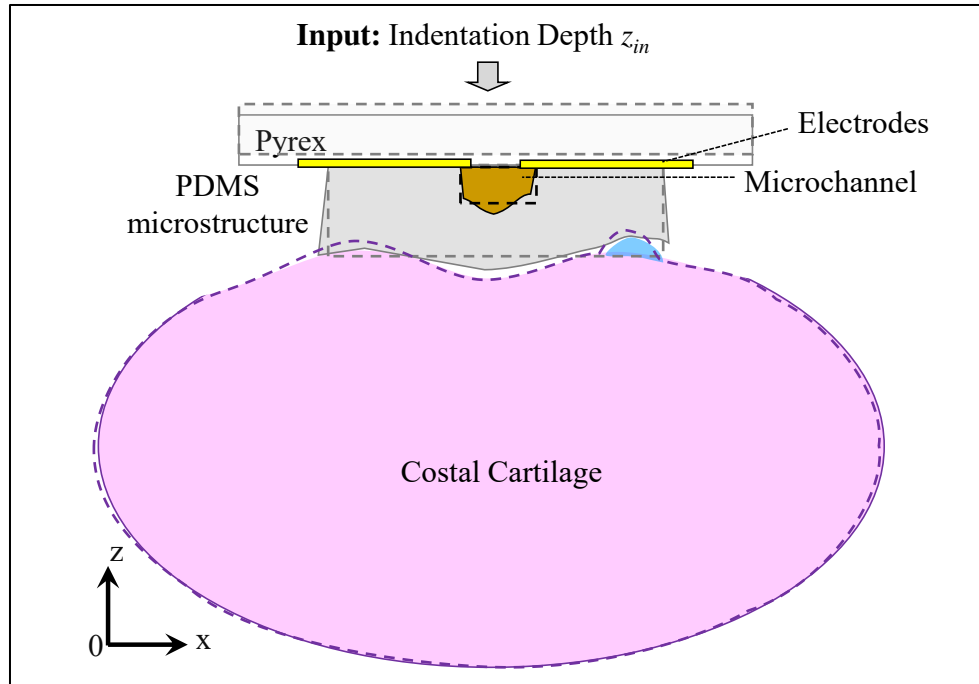


Figure 2.19. Interaction between the tactile sensor and a CC tissue at its exterior surface. (dashed line: before indentation; solid line: after indentation)

2.5. Discussion

In this section, sensor configuration, rationale, fabrication critical and performance characterization are discussed, together with the encountered technical issues. To address the voltage output variations caused by fabrication variation or probe misalignment, the resistance change from each transducer is suggested to introduce for replacing the use of direct voltage output in the data analysis. Although, the types of misalignment can be distinguished by the increasing or decreasing trend of the voltage output and the response time of the transducers, for further reducing the effect of misalignment, the average of sensor deflection, z_{s-i} at each transducer can be adopted. As such, the voltage output variation caused by the misalignment can be canceled out, and further optimize the value of sensor deflection. Moreover, from the results of sensor characterization with a rigid probe, linear relations and high robust features are observed in both the force-deflection relation and resistance change-deflection relation. Thus,

despite the inconsistency in the initial voltage values caused by the misalignment of probe or fabrication variations, the sensor is still able to detect the change in the input. As a result, the voltage change or resistance change from each transducer and its slope should be used in the later calculation.

However, the effect of the CC specimen with a curved surface will require further investigation. A built-in probe is suggested to add on the top of the tactile sensor to optimize the sensor-tissue interaction region, avoid surface extrusions, achieve conformity of the curved tissue surface during measurement and ease the data interpretation for deriving the mechanical properties of a soft tissue for the recorded data.

2.6. Conclusion

This chapter depicts a previous designed polymer-based microfluidic resistive tactile sensor without a built-in probe employed in this study for detecting distributed normal loads. The theoretical models for the microfluidic device from both the mechanical and electrical perspectives are presented, which are the basis for the further analysis on the indentation-relaxation testing with the incorporation of the sensor. The fabrication process for the polymer-based microfluidic resistive tactile sensor provides a low cost and simple manufacturing solution. The performance characteristics of this tactile sensor were evaluated by two experimental studies. By the experimental study on sensor performance characterization via a rigid probe, the sensor stiffness was obtained by the force-deflection relation. The relation between the pre-defined indentation displacement and the resistance change of the tactile sensor was also built and used to extract the mechanical properties of soft tissues with a flat surface in our previous study. In the experimental study on sensor performance in CC measurement at its exterior surface, the severity of raggedness in the measured deflection-depth ($z_s - z_{in}$) relation indicates the interference of

extrusions in these measurements and sensor limit of capturing the true mechanical properties of CC with a curved surface.

According to the three repeated sensor characterization measurements, the sensor shows its robust feature and can be used over a long-duration with consistent mechanical behavior. However, both the probe misalignment issues and the sensor limit capability of capturing the mechanical behavior of CC with curved surface introduces significant errors to the measured results or even fails to detect the true mechanical properties of soft tissues. As such, the sensor design needs to be improved in the future for providing a better solution to these two main technical issues.

In sum, the polymer-based microfluidic tactile sensor without a built-in probe is introduced in this chapter. The working principle, fabrication protocols, theoretical model, sensor performance characterization, and technical issues encountered in the experimental characterization are thoroughly discussed.

CHAPTER 3

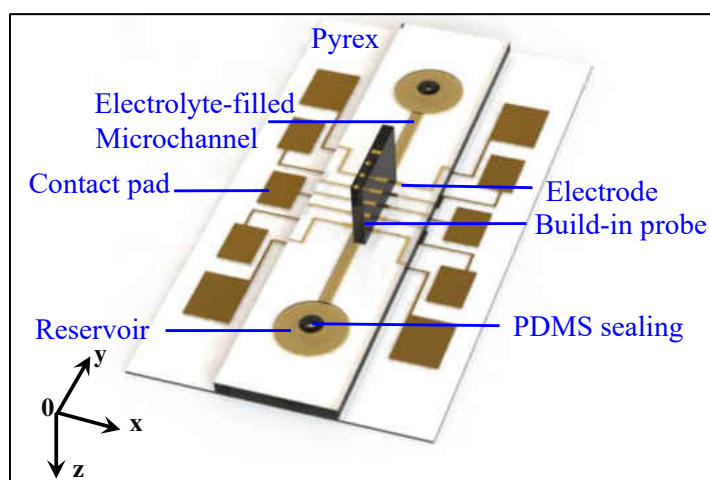
NUMERICAL AND EXPERIMENTAL STUDY ON A BUILT-IN PROBE ON THE TACTILE SENSOR FOR CURVED SURFACE

The objective of this chapter is to investigate the feasibility of a tactile sensor with a built-in probe for mechanical measurements of CC at its exterior surface. In chapter 2, it demonstrates a tactile sensor without a built-in probe and successfully characterized its performance by a rigid cylindrical probe which is capable of measuring mechanical properties of soft tissues with a flat surface in our previous study[48]. However, the sensor fails to measure the mechanical properties of CC at its exterior surface, due to its nonconformity to the curved tissue surface. In this chapter, a built-in probe is added to the top of the sensor to conform to the curved tissue surface in measurement, so that the curved tissue surface does not distort the measured mechanical properties of CC. Although flexible tactile sensors have been proposed for mechanical measurement of soft tissues with a curved surface and two flexible tactile sensors have recently been demonstrated for great conformity to curved tissue surface [49, 50], mechanical measurements of soft tissues with curved surface using such sensors have not been reported in the literature. This chapter is the first of its kind to achieve conformal mechanical measurements of soft tissues with a curved surface using a tactile sensor and measure the mechanical properties of CC at its exterior surface. The sensor used in this chapter is sensor B.

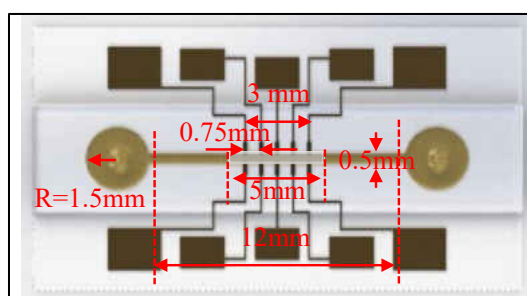
3.1. Configuration and Rationale

Based on the tactile sensor described in Chapter 2, a built-in probe is added to the top of the PDMS microstructure and coincides with the transducer array and has an in-plane dimension of 0.5mm×5mm as illustrated in Figure 3.1. Since the probe and the transducer array share the same width, the probe-tissue interaction is confined to the top of the transducer array,

thus avoiding the interference from the interaction between the tissue and the rest region of the microstructure surrounding the probe in mechanical measurement. As such, the distributed deflection acting on the top of the built-in probe causes geometrical changes in the transducer array and registers as resistance changes by the transducers at their locations. The built-in probe can be added to the sensor by pouring a mixture of 10:1 (Base: Curing agent) PDMS material into the mold for the probe. The key dimensions and their values of the tactile sensor are summarized in Table 2.1 located in Section 2.1.



(a)



(b)

Figure 3.1. Schematics of a tactile sensor with a built-in probe: (a) 3D configuration; (b) Top view with key dimensions.

3.2. Theoretical Analysis

3.2.1. Theoretical model

CC possess an extremely irregular geometry and are thus chosen as the example of a soft tissue with a curved surface for analysis. Figure 2.19 in Section 2.4.3 already depicts the interaction between a CC tissue and the tactile sensor without a built-in probe. Owing to the curved tissue surface, the rest region of the microstructure surrounding the transducer array interferes with the interaction between the portion of the microstructure above the transducer array and the tissue region underneath, which prevents the sensor from capturing the true mechanical properties of the tissue region underneath the transducer array. After adding a built-in probe on the top of PDMS microstructure, the interaction between CC and the sensor with a built-in probe is presented in Figure 3.2 providing the comparison with the tissue-sensor interaction without a built-in probe in Figure 2.19. Figure 3.2 shows that such interference has been avoided after attaching a built-in probe to the top of the microstructure. Meanwhile, as compared with the sensor-tissue interaction in Figure 2.19, the probe-tissue interaction in Figure 3.2 is confined to a very small region. Thus, the curved tissue surface in the probe-tissue interaction can be treated as a flat surface. As long as a full contact between the probe and the tissue region is maintained in a measurement, the true mechanical properties of the tissue region can be manifested in the sensor outputs. In addition, since the built-in probe is attached right on the portion of microstructure which is above the microchannel, the probe top deformation could be directly transferred to the microchannel top deflection and prevent the inference of the surrounding area of the microchannel to alleviate the effect of x-y in-plane misalignment.

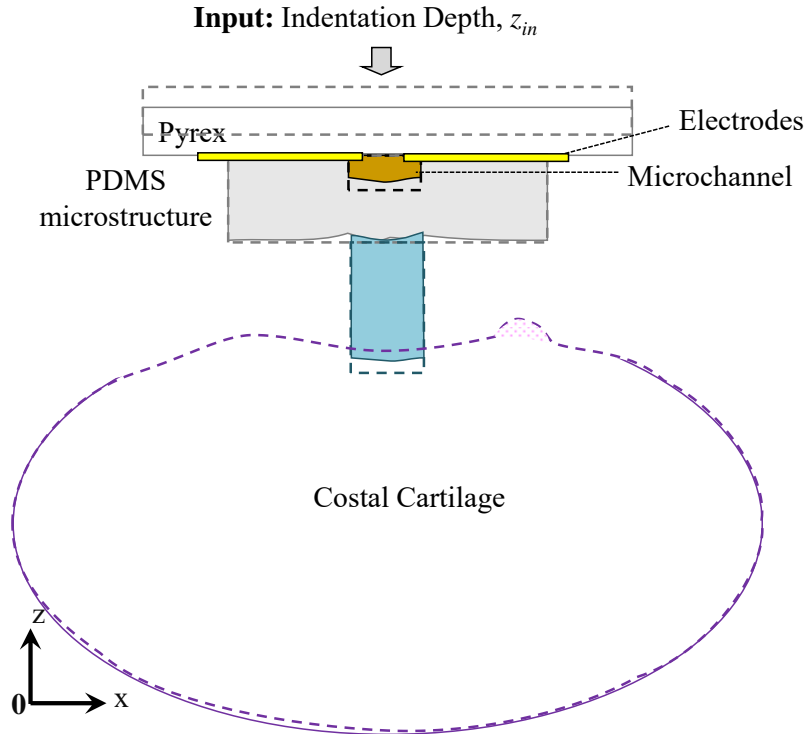


Figure 3.2. Interaction between the tactile sensor with a built-in probe and a CC tissue at its exterior surface. (dashed line: before indentation; solid line: after indentation)

Figure 3.3 (a) illustrates the rationale for mechanical measurement of a CC tissue with a curved surface using the sensor with a built-in probe. After being aligned with the tissue surface, the sensor is pressed against the tissue with a pre-defined indentation depth input, z_{in} . Then, the tissue region under the probe, the probe and the portion of the microstructure above the transducer array all experience deflection. Owing to the deflection conformity, the indentation depth input, z_{in} , should be equal to the sum of tissue deflection, z_t , the probe deflection, z_p , and the deflection of the microstructure, z_s . The sum of the probe deflection, z_p , and the deflection of the microstructure, z_s can be considered as the equilibrium deflection of the sensor with a built-in probe, z_s' .

$$z_{in} = z_t + z_p + z_s, \quad z_{in} = z_t + z_s', \quad (3.1)$$

The microstructure, the probe, and the tissue region can be treated as a lumped-model

with two or three springs in series as shown in Figure 3.3 (b) and (c). The reaction force, F , should be the same for them:

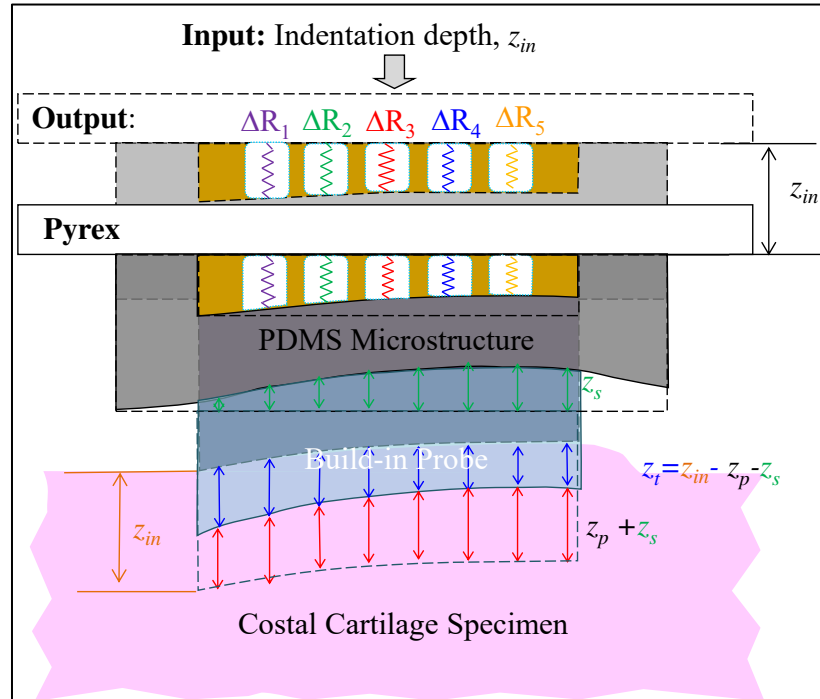
$$F = k_t \cdot z_t = k_p \cdot z_p = k_s \cdot z_s = k_{s'} \cdot z_{s'} \quad (3.2)$$

where k_t , k_p , k_s and $k_{s'}$ denote the tissue stiffness, probe stiffness, sensor stiffness, and equilibrium stiffness of the sensor with the built-in probe, respectively. Note that the sensor deflection can be obtained from the transducers and therefore serve as the outputs in a measurement. The probe deflection is related to the sensor deflection by:

$$z_p = \frac{k_s}{k_p} \cdot z_s \quad (3.3)$$

According to Equation 3.1 and Equation 3.3, the tissue deflection becomes:

$$z_t = z_{in} - z_s - \frac{k_s}{k_p} \cdot z_s, \quad z_t = z_{in} - z_s \quad (3.4)$$



(a)

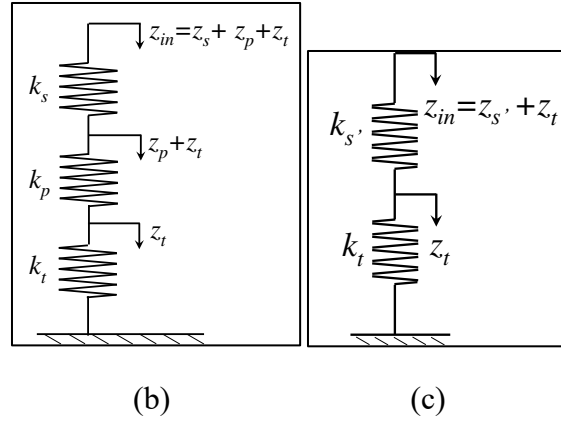


Figure 3.3. A tactile sensor with a built-in probe for measuring mechanical properties of a soft tissue with non-flat surface (drawn not to scale for clear illustration): (a) rationale (the transducers are color coded for clear illustration of resistance changes caused by sensor deflection), (b) three springs lumped-model and (c) two springs lumped-model (sensor with built-in probe is considered as one equilibrium spring) of PDMS microstructure, built-in probe and tissue region for the tissue-sensor interaction.

Based on Equation 3.2 and Equation 3.4, the tissue stiffness can be expressed as:

$$k_t = \frac{z_s}{z_t} \cdot k_s = \frac{z_s \cdot k_s}{z_{in} - \left(1 + \frac{k_s}{k_p}\right) \cdot z_s} = \frac{\hat{z} \cdot k_s}{1 - \left(1 + \frac{k_s}{k_p}\right) \cdot \hat{z}}, \quad k_t = \frac{z_{s'}}{z_t} k_{s'} = \frac{z_{s'} \cdot k_{s'}}{z_{in} - z_{s'}} = \frac{\hat{z}' \cdot k_{s'}}{1 - \hat{z}'} \quad (3.5)$$

where

$$\hat{z} = \frac{z_s}{z_{in}}, \quad \hat{z}' = \frac{z_{s'}}{z_{in}} \quad (3.6)$$

In a measurement, the recorded data on the tissue region is the relation of the sensor deflection versus the indentation depth. Here, \hat{z} , \hat{z}' defines the deflection-depth slope of the sensor deflection (without built-in probe) versus the indentation depth and the deflection-depth slope of the equilibrium sensor deflection (with built-in probe) versus the indentation depth which are immune to the uncertainty in contact point.

The portion of the microstructure above the transducer array undergoes flexural deflection in a measurement. Then, the sensor stiffness is related to the sensor design parameters

by:

$$k_s \propto \frac{E_s \cdot h_s^3}{A} \quad (3.7)$$

where A is the probe in-plane dimension; and E_s and h_s are the elasticity and height of the PDMS microstructure, respectively. The probe experiences axial loading as a block and its stiffness is given by:

$$k_p = \frac{E_p \cdot A}{h_p} \quad (3.8)$$

where E_p and h_p are the elasticity and height of the probe, respectively. The ratio of the sensor stiffness to the probe stiffness is defined as:

$$\alpha = \frac{k_s}{k_p} \propto \frac{E_s \cdot h_s^3 \cdot h_p}{E_p \cdot A^2} \quad (3.9)$$

The tissue stiffness is related to the probe in-plane dimension by:

$$k_t \propto \frac{E_t \cdot A}{h_t} \quad (3.10)$$

According to Equation 3.7~3.10, the design parameters of the sensor and the built-in probe can be adjusted for achieving the desired relations among the sensor, probe, and tissue stiffness, which is critical for accurate mechanical measurement of a tissue with a curved surface.

3.2.2. Design and Qualitative Analysis of the Tactile Sensor with a Built-in Probe

As illustrated in Figure 3.4, three sets of design parameters are involved in the mechanical measurement of a CC tissue with a curved surface:

- i) Tissue parameters: tissue baseline thickness, h_t , tissue elasticity, E_t , and the highest thickness, δ_b , above the baseline thickness;
- ii) Sensor parameters: sensor stiffness, k_s , and sensor linear deflection range, $(0, z_{s_linear})$;
- iii) Built-in probe parameters: probe elasticity, E_p , and probe thickness, h_p .

The tissue parameters are the inherent characteristics of the tissue itself. The parameters of the sensor and the probe need to be tailored to meet the following three performance criteria for the tissue of interest:

- 1) The indentation depth range needs to ensure that the tissue strain reaches a certain level;
- 2) The probe should be conformed to the curved tissue surface in the lower indentation depth range so that the higher indentation depth range is utilized to acquire the mechanical properties of the tissue region;
- 3) The sensor needs to operate in its full linear deflection range in accordance with the indentation depth range so as to minimize experimental errors.

Table 3.1 summarizes the related parameters and their values used for the design of the sensor and the probe. The elasticity of CC, E_t , is in the range of 1MPa-7MPa and its baseline thickness, h_t , is about 10mm. The highest thickness of the tissue, δ_t , above the baseline thickness is assumed to be 0.5mm. The maximum linear deflection of the sensor, z_{s_max} , is 0.8mm. The sensor stiffness, k_s , is $1272\text{N}\cdot\text{m}^{-1}$, which is obtained from the experimental characterization of the sensor. The probe in-plane dimension, A , is fixed at $0.5\text{mm}\times 5\text{mm}$. The probe is assumed to be also made of 10:1 (Base: Curing agent) PDMS and its elasticity, E_p , is the same as the PDMS microstructure.

Table 3.1 The key design parameters and their values of the sensor and the built-in probe for mechanical measurement of costal cartilage tissues.

Parts	Parameters	Values	Symbols
Tissue	Elasticity range	1MPa-7MPa	E_t
	Baseline thickness	10mm	h_t
	Highest thickness	0.5mm	δ_t
Sensor	Maximum strain	10%	ε_{t_max}
	Sensor stiffness	$1272\text{N}\cdot\text{m}^{-1}$	k_s
	Maximum linear deflection	0.8mm	z_{s_linear}
Built-in probe	Elasticity	700kPa	E_p
	In-plane dimension	$0.5\text{mm}\times 5\text{mm}$	A

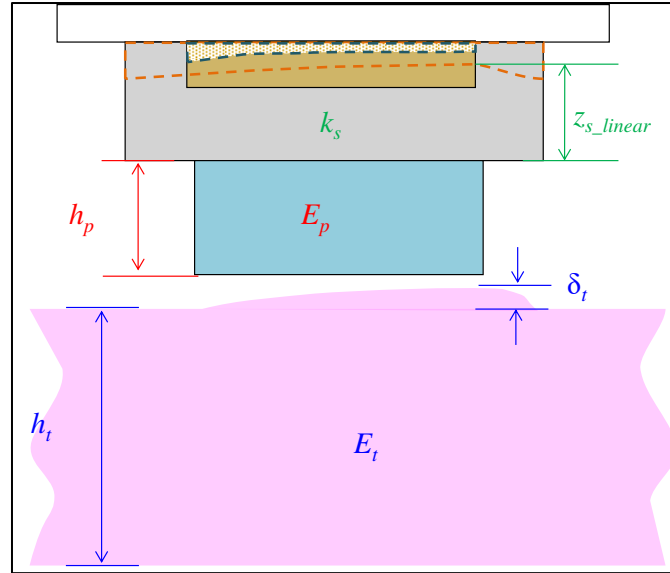


Figure 3.4. Three sets of design parameters involved in mechanical measurement of a CC tissue with curved surface (cartilage axial direction): i) Tissue parameters: tissue baseline thickness, h_t , tissue elasticity, E_t , and the highest thickness, δ_t , above the baseline thickness; ii) Sensor parameters: sensor stiffness, k_s , and sensor linear deflection range, $(0, z_{s_linear})$ (Solid line: before indentation depth; Dash line: after indentation depth); iii) Built-in probe parameters: probe elasticity, E_p , and probe thickness, h_p .

The maximum tissue strain, ε_{t_max} , relative to the baseline thickness in a measurement is assumed to be 10%. Then, the maximum tissue deflection, z_{t_max} , becomes:

$$z_{t_max} = \varepsilon_{t_max} \cdot h_t \quad (3.11)$$

The maximum tissue deflection is 1mm. According to Equation 3.1 and 3.9, in response to the maximum tissue deflection, z_{t_max} , the maximum sensor deflection, z_{s_max} , and the maximum probe deflection, z_{p_max} , are:

$$z_{s_max} = \frac{k_t}{k_s} \cdot z_{t_max} \quad (3.12)$$

$$z_{p_max} = \alpha \cdot z_{s_max} = \alpha \cdot \frac{k_t}{k_s} \cdot z_{t_max} \quad (3.13)$$

Then, based on Equation 3.1, 3.12, and 3.13, the maximum indentation depth becomes:

$$z_{in-max} = \left(1 + (1 + \alpha) \cdot \frac{k_t}{k_s} \right) \cdot z_{t-max} \quad (3.14)$$

Similarly, the sensor deflection, δ_s , and the probe deflection, δ_p , used for accommodating the curved tissue surface with the highest thickness, δ_t , above the baseline thickness become:

$$\delta_s = \frac{k_t}{k_s} \cdot \delta_t, \quad \delta_p = \alpha \cdot \frac{k_t}{k_s} \cdot \delta_t \quad (3.15)$$

Then the indentation depth, δ_{in} , required for tissue surface accommodation is:

$$\delta_{in} = \left(1 + (1 + \alpha) \cdot \frac{k_t}{k_s} \right) \cdot \delta_t \quad (3.16)$$

Based on Equation 3.12~ 3.16, we analyze how to tailor the design of the sensor and the probe to meet the three performance criteria. In most cases, the maximum tissue deflection is above 1mm for achieving a relatively high tissue strain (>10%). According to Equation 3.12, when the sensor stiffness, k_s , is the same as the tissue stiffness, k_t , the maximum sensor deflection, z_{s-max} , is equal to the maximum tissue deflection, z_{t-max} . Since the microstructure in the sensor is only 1mm thick, the maximum linear deflection, $z_{s-linear}$, is less than 1mm ($z_{s-linear} < 1\text{mm}$). Moreover, according to the Equation 3.15, the sensor needs to deform by a small amount, δ_s , in the lower indentation depth range when the built-in probe deforms, δ_p , to conform to the curved tissue surface with the highest thickness, δ_t . In other words, the sum of the maximum sensor deflection, z_{s-max} , and sensor deflection for fitting the curved surface, δ_s , should be lower than its maximum linear deflection, $z_{s-linear}$ ($z_{s-max} + \delta_s < z_{s-linear}$), which is lower than 1mm. Then, the sensor deflection is able to stay in its linear deflection range for capturing the true mechanical properties of the tissue. Therefore, the sensor stiffness, k_s , must be lower than the tissue stiffness, k_t ($k_s < k_t$).

When the sensor stiffness, k_s , is lower than the tissue stiffness, k_t , the maximum sensor deflection, z_{s_max} , is a fraction of the maximum tissue deflection, z_{t_max} . The ratio of the sensor stiffness to the tissue stiffness, k_t / k_s , needs to be tailored such that the maximum sensor deflection, z_{s_max} , is a little bit lower than the adjusted maximum linear deflection, $z_{s_linear} - \delta_s$, of the sensor so that the collected data is not located in a very low linear deflection range of the sensor.

According to Equation 3.13, the maximum probe deflection, z_{p_max} , is the maximum sensor deflection, z_{s_max} , multiplied by the stiffness ratio, α . Since the built-in probe needs to accommodate the highest thickness, δ_t , on the curved tissue surface by δ_p , the probe stiffness, k_p , should be lower than the sensor stiffness, k_s , or $\alpha > 1$. In the meantime, the probe elasticity, E_p , and in-plane dimension, A , are fixed, in accordance with the material used and the dimension of the transducer array, respectively. Then, according to Equation 3.8, a low probe stiffness translates to a high probe height, $h_{p_buckling}$, which may cause buckling in the tissue-probe-sensor interaction. As such, the probe height, h_p , is a tradeoff between accommodation of the highest thickness, δ_t , on a curved tissue surface and avoidance of buckling ($\delta_p < h_p < h_{p_buckling}$).

In Table 3.1, the elasticity range of CC is 1MPa-7MPa. According to Equation 3.10, the highest tissue stiffness is seven times the lowest tissue stiffness. Then, the sensor and the probe designed for measuring CC with its elasticity in the higher end will cause the collected data on CC with its elasticity in the lower end to be located with the lower linear deflection range of the sensor. This indicates that the measured results on CC with lower elasticity bear a much larger amount of experimental errors, as compared with its counterparts on CC with higher elasticity. In contrast, the sensor and the probe designed for CC with its elasticity in the lower end will simply fail to measure the mechanical properties of CC with its elasticity in the higher

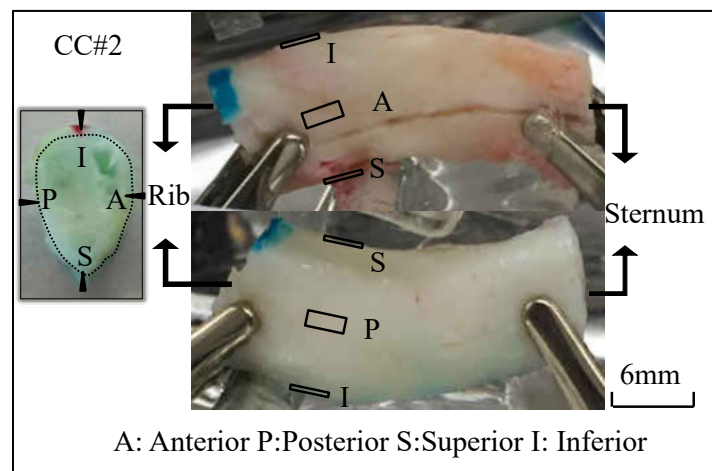
end.

Finally, the theoretical analysis on the relations of the design parameters of the sensor and the probe to the tissue parameters is a scaling analysis. The tissue-probe-sensor interaction in mechanical measurement is, by no means, simply one-dimensional. To accurately determine the design parameters of the sensor and the probe, a numerical analysis needs to be conducted for soft tissues of interest in the future.

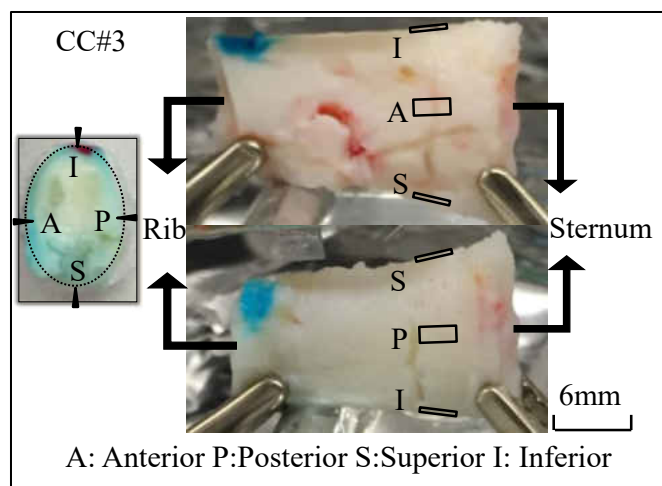
3.3. Performance Characterization

3.3.1. Sample preparation

Two human CC samples (CC#2 and CC#3) were first chosen from two PC patients at Children's Hospital of The King's Daughter's (CHKD), Norfolk, VA for the trial proof-of-concept test. Prior to removal of the cartilage tissues, patient consent was obtained with full IRB approval. Both of the samples were from ribs of the lower thoracic region. Figure 3.5 (a) and (b) show the two samples from different ribs of a 15yr-old male patient. These two samples were measured right after they were removed from the patient. Note that intercostal muscles and perichondrium were removed from the surface of the samples.



(a)



(b)

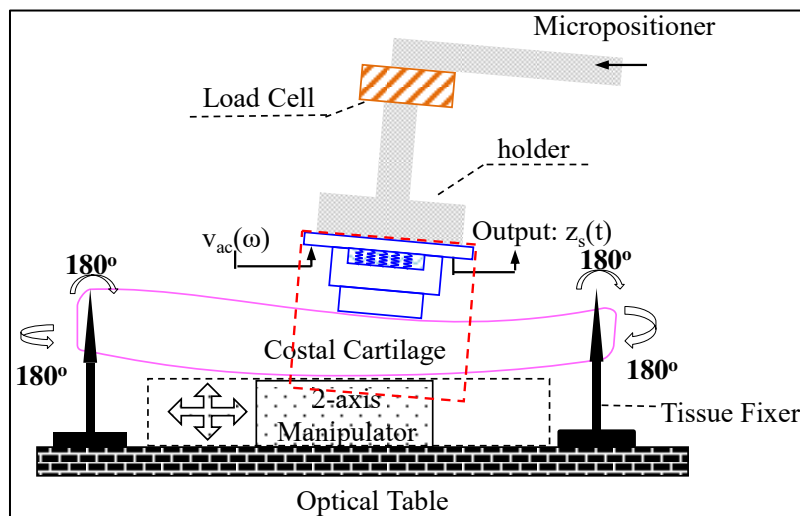
Figure 3.5. Pictures of human PC costal cartilage samples with measured locations (a) CC #2 (b) CC #3. (Blue color on CC #2 and CC #3 came from the marker for marking locations; black blocks and arrows on the cross sections of the samples indicate the locations of the probe in measurement; and left side: toward rib, right side: toward sternum)

3.3.2. Testing protocol

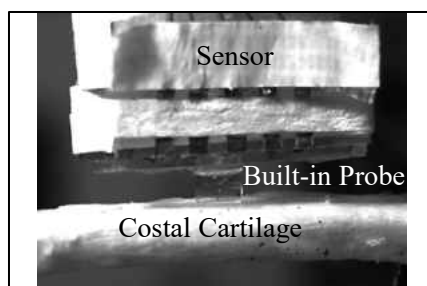
Figure 3.6 illustrates the experimental setup on an optical table for both performance characterization of the sensor and mechanical measurements of the CC samples. It is similar to the experimental setup up used in Section 2.3.2. Similarly, with the probe facing downward, the sensor was connected to a load cell and was further fixed to a micropositioner. A few electronic instruments were connected to the sensor for recording the resistance signals of its transducer array. The details about the experimental setup and signal acquisition can be found in the literature in Section 2.3.1. However, the method for fixing the sample is slightly changed. In brief, prior to measuring the CC samples, a Pyrex slide was placed under the sensor. With the micropositioner controlling the displacement of the sensor, the sensor was pressed against this slide, and the corresponding overall reaction force and the resistance changes were recorded by the load cell and the sensor, respectively. The only difference is the tactile sensor used in this setup is attached with a built-in probe. The built-in probe of $0.5\text{mm} \times 5\text{mm} \times 3\text{mm}$ is aligned right

over the transducer array and has a 1mm overlap at each side of the transducer array along the array length to avoid the edge effect during the probe deformation. The elasticity of the built-in probe is the same elasticity of PDMS microstructure to ease the data processing.

The sensor displacement was the deflection at the top of the probe, which is defined as the sensor deflection, z_s . Figure 3.7 illustrates the measured relations of the resistance changes, ΔR , of the five transducers (1~5) and overall reaction force, F , versus the sensor deflection, z_s . Defined as the slope of the overall reaction force versus the sensor deflection, the measured sensor stiffness, k_s , was $960\text{N}\cdot\text{m}^{-1}$. Since the sensor A used in Chapter 2 is damaged, a sensor B with an identical design is chosen for this performance characterization. Sensor A is only used for showing the limitation of the sensor without a built-in probe. It won't affect any measured results in the following study. The stiffness mentioned previously, is the equilibrium stiffness of the sensor B with a built-in probe. The relations of the resistance changes to the sensor deflection were utilized to convert the recorded resistance changes in the CC measurements to the sensor deflection. Owing to fabrication variation, the relation of the resistance change versus the sensor deflection varied among the transducers, although they were designed identically.



(a)



(b)

Figure 3.6. Experimental setup (a) schematic (b) the sensor with a built-in probe aligned on CC.

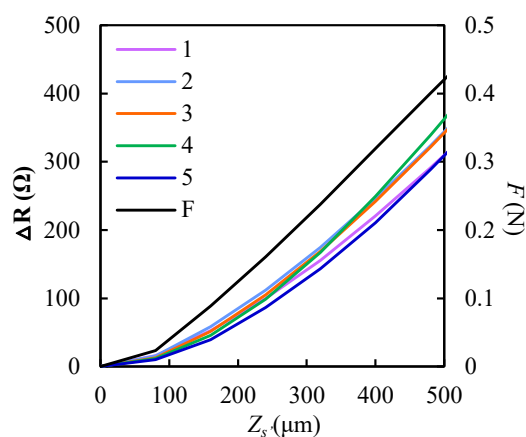


Figure 3.7. Performance characterization of the tactile sensor with a built-in probe: resistance changes, ΔR , of the five transducers (1~5) and overall reaction force, F , as a function of the sensor deflection, z_s .

As shown in Figure 3.5 (a) and (b), the four locations: anterior/posterior surfaces and superior/inferior borders, at the same position of CC # 2 and #3 measured using the sensor with a built-in probe. To get these locations facing the sensor, a CC specimen was rotated and fixed at its two ends with clips. A 2-axis manipulator with a mold holder was placed under the measured position of the sample for further securing the sample in place and serving as the supporting substrate during measurement. PBS was sprayed on the cartilage surface to maintain its hydration during measurement. After the sensor was manually aligned with a CC specimen, a custom LabVIEW program was used to carry out a measurement. Only one measurement was

conducted at each location of CC #2 and CC #3, since the first measurement was believed to be close to their in vivo mechanical behavior as mentioned in the CC#1 measurement in Chapter 2.

The pre-defined indentation patterns used for these two samples still follow the pattern in Figure 2.10. As compared with the testing parameter for CC#1($z_{step}=100\mu\text{m}$, ramp speed of $\dot{z}=1\text{mm}\cdot\text{s}^{-1}$, a hold time of $t_{hold}=20\text{s}$ and a final indentation depth, $z_{final}=1\text{mm}$). The testing parameters used for CC #2 and CC#3 were: $z_{step}=80\mu\text{m}$, $\dot{z}=0.2\text{mm}\cdot\text{s}^{-1}$, $t_{hold}=40\text{s}$, and $z_{final}=1.28\text{mm}$. The reduction in incremental depth was aimed to increase data points in a measurement; the reduction in ramp speed was to match those values commonly used in CC measurements in the literature [1]; the increase in hold time helped quantitatively maximize the normalized relaxation which is defined in the next section and used to qualify the CC viscosity; and the built-in probe increased the linear operation range of the sensor and this allowed the increase in final indentation depth.

A CC sample experienced a step displacement input at each incremental depth and underwent stress relaxation over the following hold time. In response to the indentation depth input, the outputs were the time-varying deflections of the sensor at the locations of the transducer array, or spatially distributed sensor deflection along the transducer array. Thus, the originally recorded data on a CC sample were the spatially distributed sensor deflection as a function of time, in response to the indentation depth input.

As mentioned in Section 2.4.1, one of the encountered technical issues for this sensor is the fabrication variation, even with the identical design. In order to solve this issue, a PDMS block with mixing ratio of 1 to 10 and a dimension of $3\text{mm} \times 3\text{mm} \times 6\text{mm}$ is used as a standard for the sensor calibration. Thus, the variation caused by the fabrication process among the different sensors with identical design can be discarded. The measured CC elasticity can be

compared and calibrated with the PDMS elasticity, 700kPa to ensure its accuracy. Please note that mechanical properties of the CC in the following sections of this dissertation are all being tested by the calibrated tactile sensor.

3.3.3. Data analysis

In order to simplify the data analysis, the two springs in a series lumped-element model is adopted in this section. As such, according to Figure 3.8 and Equation 3.5, the deflection-depth slope at the start of the hold time of each incremental depth is defined as the instant deflection-depth slope. Then, the instant CC stiffness becomes:

$$k_{instant} = \frac{\hat{z}_{instant} \cdot k_{s'}}{1 - \hat{z}_{instant}} \quad (3.17)$$

As shown in Figure 3.6 (a), the probe is very small relative to a CC specimen. Then, the probe-tissue interaction can be treated as a rectangular flexible flat-ended probe on a semi-infinite elastic medium. The tissue instant indentation modulus is thus related to the measured instant tissue stiffness by [51]:

$$E_{instant} = \frac{1 - \nu^2}{8.9a} \cdot k_{instant} (t = 0s) \quad (3.18)$$

where $\nu=0.4$ is the Poisson's ratio of a CC specimen, and $a=0.25\text{mm}$ is half of the probe width.

$k_{instant} (t=0)$ is the instant stiffness of CC at the start of the hold time.

According to Equation 3.12, the instant stress, $\sigma_{i-instant}$, and relaxed stress, $\sigma_{i-relaxed}$, in the tissue region at the i^{th} indentation depth are:

$$\sigma_{i-instant} = \frac{k_{s'} z_{s'-i-instant}}{A} ; \sigma_{i-relaxed} = \frac{k_{s'} z_{s'-i-relaxed}}{A} \quad (3.19)$$

where $A=0.5\text{mm}\times 5\text{mm}$ denotes the probe in-plane dimension, and $z_{s'-i-instant}$ and $z_{s'-i-relaxed}$ denote the instant and relaxed sensor deflection, respectively. Since the curved shape of the tissue region under the probe is mild, it is reasonable to assume the in-plane dimension of the tissue region is the same as the probe in-plane dimension. As shown in Figure 3.8(b), we define the normalized relaxation as the stress drop, $\Delta\sigma_i$, normalized to the stress input, σ_{i-step} , at the i th incremental depth:

$$\Delta E_i = \frac{\Delta\sigma_i}{\sigma_{i-step}} = \frac{\sigma_{i-instant} - \sigma_{i-relaxed}}{\sigma_{i-instant} - \sigma_{(i-1)-relaxed}} \times 100\% \quad (3.20)$$

The instant indentation modulus and normalized relaxation of the CC segments were derived from the recorded data to quantify their elasticity and viscosity, respectively.

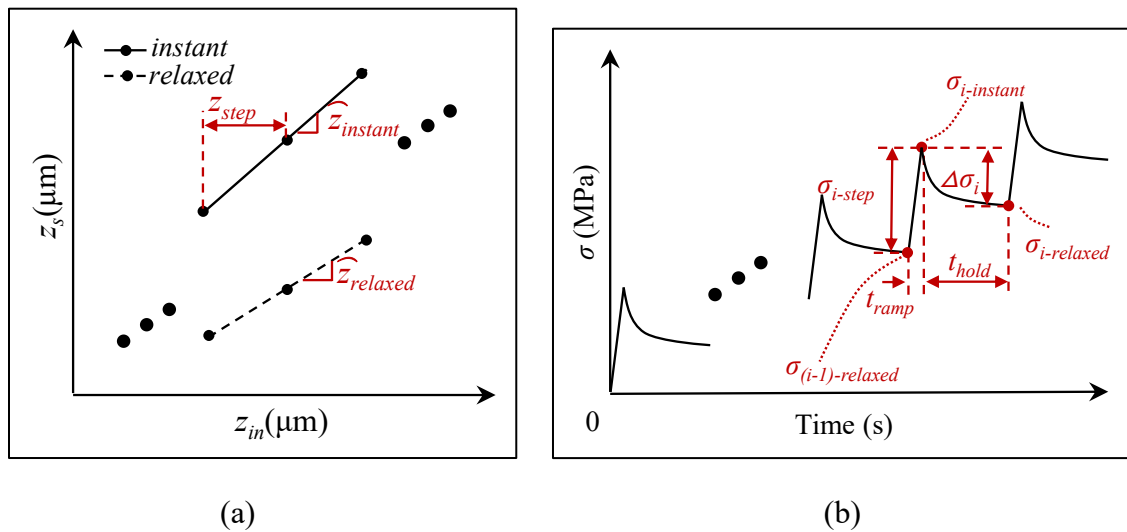


Figure 3.8. Conformational mechanical measurement of costal cartilage at its exterior surface using the tactile sensor with a built-in probe (a) definition of the deflection-depth slope (here, $\hat{z}' = \hat{z}'_{instant}$) (b) definition of parameters related to normalized relaxation.

3.3.4. Finite Element Analysis

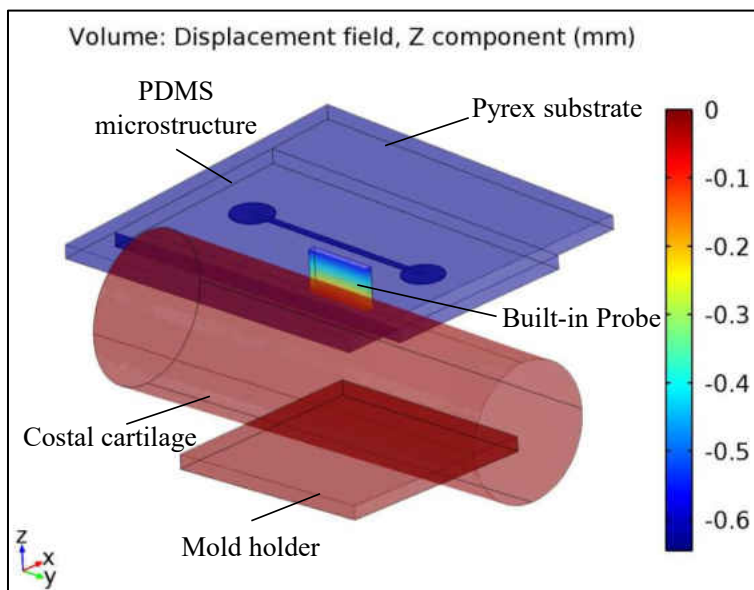
3.3.4.1. Finite Element Modeling

In this section, to investigate how tissue elasticity measured using the indentation-relaxation method varies with tissue parameters, a finite element model (FEM) is created using

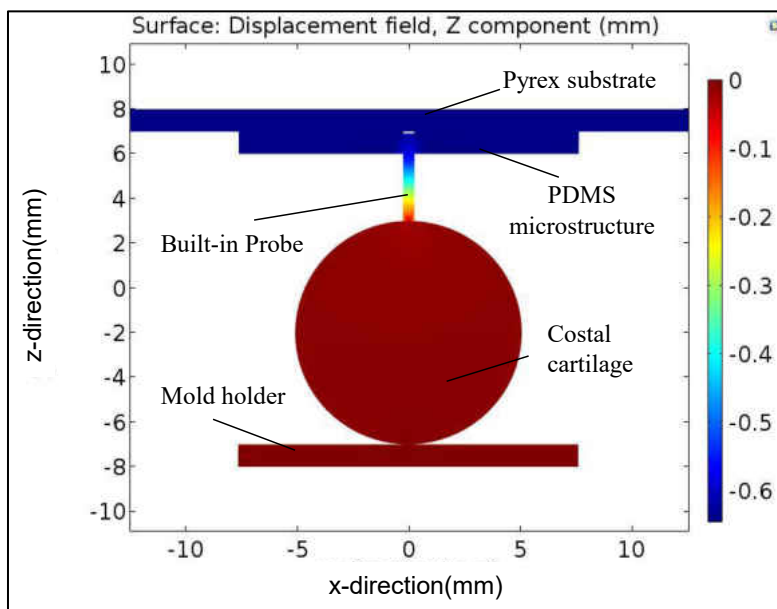
COMSOL Multiphysics (Version 5.1, COMSOL Inc., Burlington, MA, USA). In the FEM, the tactile sensor is represented by the PDMS microstructure, the Pyrex substrate, and the PDMS built-in probe. The built-in probe is aligned on the top center of the PDMS microstructure and along the microchannel length. The sensor with a built-in probe is flipped over and aligned at the cylindrical CC exterior surface. Below the CC specimen, a steel mold holder is also included in the FEM as shown in Figure 3.9. For simplicity, the built-in probe, the PDMS microstructure, and the cylindrical CC are assumed to be elastic materials. The bottom surface of the mold holder is fixed. The input is the pre-defined indentation depth acting on the Pyrex substrate bottom. The output is the top deflection of the probe (z-displacement) at the tissue-probe interaction surface.

With the sensor parameters being fixed in the FEM, the pre-set CC elasticity (Young's modulus) and the CC diameter are varied separately to examine how they affect the deflection-depth slope, $\hat{z}_{simulated}$ and the simulated tissue elasticity, $E_{simulated}$, which is considered to be equivalent to the measured tissue elasticity $E_{instant}$ in the experimental measurement. Furthermore, since the key parameters of the sensor and built-in probe is determined during the fabrication process before the testing, it is critical to see how the compensation coefficient, γ , defined as the ratio of pre-set CC elasticity ($E_{pre-set}$) to the simulated CC elasticity ($E_{simulated}$) by the sensor with a built-in probe can be determined by using these particular designed key parameters of the tactile sensor. Other than the main geometric dimension of the tactile sensor listed in Table 2.1 and Table 3.1, the material properties of the simulation are summarized in Table 3.2. There are two CC variables, pre-set CC elasticity, $E_{pre-set}$ and CC diameter, $h_{pre-set}$. To estimate how the simulated CC elasticity, $E_{simulated}$, varies with the CC diameter, $h_{pre-set}$, at different pre-set CC

elasticity, $E_{pre-set}$, ranging from 100kPa to 7000kPa, the CC diameter, $h_{pre-set}$, is increased by 1mm at a time in the range of 3mm-14mm. The in-plane dimension is 0.5mm \times 5mm.



(a)



(b)

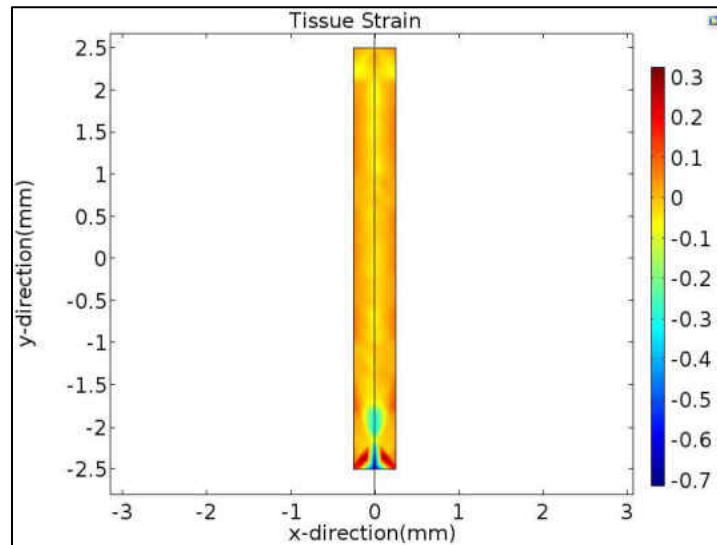
Figure 3.9. The z-displacement distributions of the tissue-sensor interaction in the indentation-relaxation test with a 0.64 mm indentation depth applied on the sensor bottom: (a) 3D view; (b) side view of x-z plane.

Table 3.2 Material properties used in the simulation.

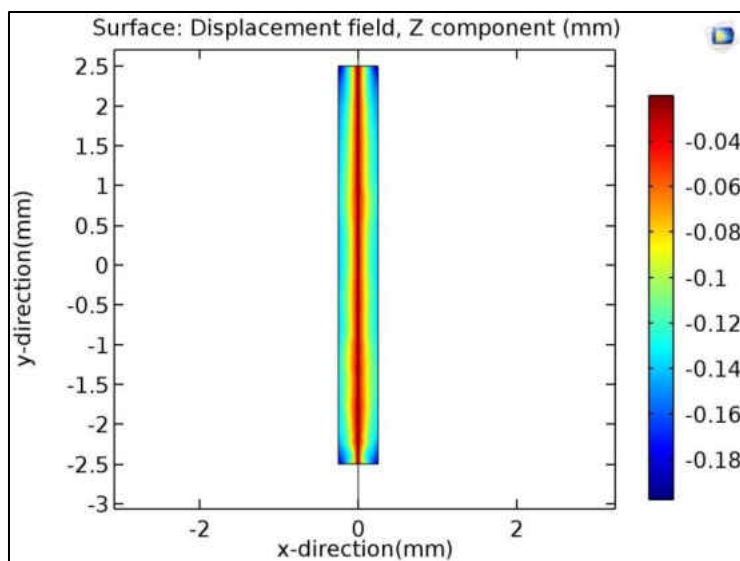
Parts	Parameters	Symbols	Values	Unit
PDMS Microstructure	Young's modulus of PDMS	E_s	700	kPa
	Poisson's ratio of PDMS	ν_s	0.45	-
	Density of PDMS	ρ_s	1000	kg·m ⁻³
	Height of PDMS	h_s	1	mm
	Microchannel cross-section	$w_E \times h_E$	0.5×0.08	mm ²
Pyrex substrate	Young's modulus of the substrate	E_{Pyrex}	1560	GPa
	Poisson's ratio of the substrate	ν_{Pyrex}	0.2	-
	Density of the substrate	ρ_{Pyrex}	2230	kg·m ⁻³
	Height of the substrate	h_{Pyrex}	1	mm
Built-in probe	In-plane dimension	A	0.5mm×5mm	mm ²
	Young's modulus of probe	E_p	700	kPa
	Poisson's ratio of probe	ν_p	0.45	-
	Density of probe	ρ_p	1000	kg·m ⁻³
	Height of probe	h_p	3	mm
Costal Cartilage	Young's modulus range of CC	E_t	0.1,0.5—7(increment:0.5)	MPa
	Poisson's ratio of CC	ν_t	0.4	-
	Density of CC	ρ_t	1000	kg·m ⁻³
Mold holder	Diameter range of CC	h_t	3-14(increment:1)	mm
	Young's modulus of mold holder	E_{holder}	530	GPa
	Poisson's ratio of mold holder	ν_{holder}	0.31	-
--	Density of mold holder	ρ_{holder}	1560	kg·m ⁻³
--	Indentation depth	z_{in}	0.64	mm

As shown in Figure 3.9 (a) and (b), the z-displacement distribution of the tissue-sensor interaction with an input indentation depth of 0.64mm acting on the exterior surface of the CC specimen, a higher deflection is found at the probe surface as compared with the deflection of the sensor top and microchannel top. Figure 3.10 (a) shows the simulated tissue strain at the tissue-sensor interaction surface across x-y plane when a 0.64mm indentation depth is applied on the sensor bottom. Figure 3.10 (b) and (c) illustrate the simulated z-displacement distribution of the contact surface on the CC exterior surface and the top surface of the five transducer array along the microchannel, respectively. It should be noted that the distributed deflection, z-displacement, acting on the top of the transducer array translates into the geometrical changes of the microchannel and registers as resistance changes. Next, the analytical method discussed in the

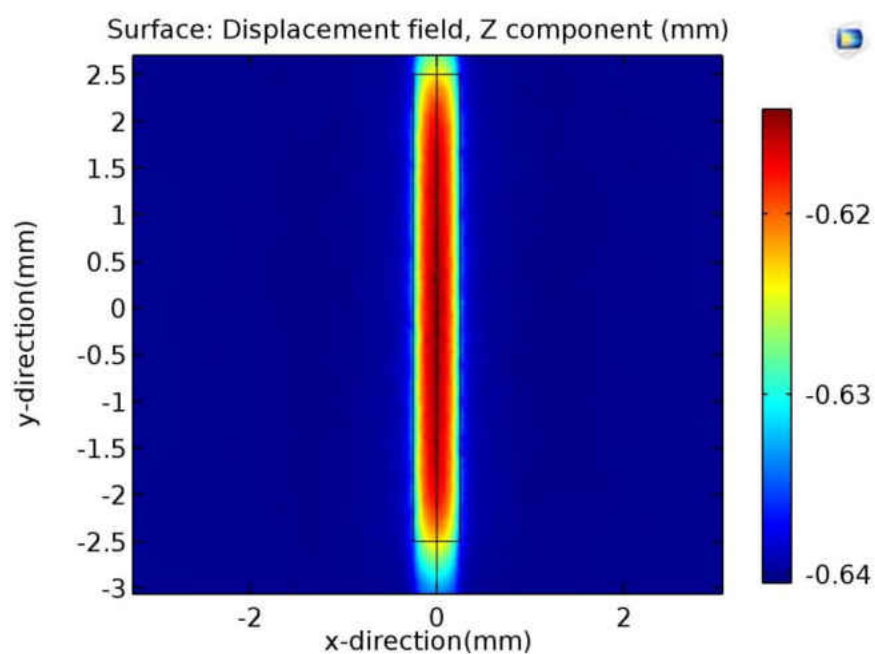
prior section is used to relate the instant simulated CC stiffness, $k_{simulated}$, and the instant simulated CC elasticity, $E_{simulated}$, of the CC site above the in-plane surface of the probe to the deflection slope, which is the probe top deflection versus the indentation depth. The overall deflection of the sensor with a built-in probe is represented by the average value of the probe deflections above the five transducer pairs. Therefore, the numerical result is the average deflection-depth slope, which mimics the deflection-depth slope measured in an experiment, and then Equations. 3.17 & 3.18 are respectively used to extract the tissue stiffness and the tissue elasticity from the simulated deflection-depth slope.



(a)



(b)



(c)

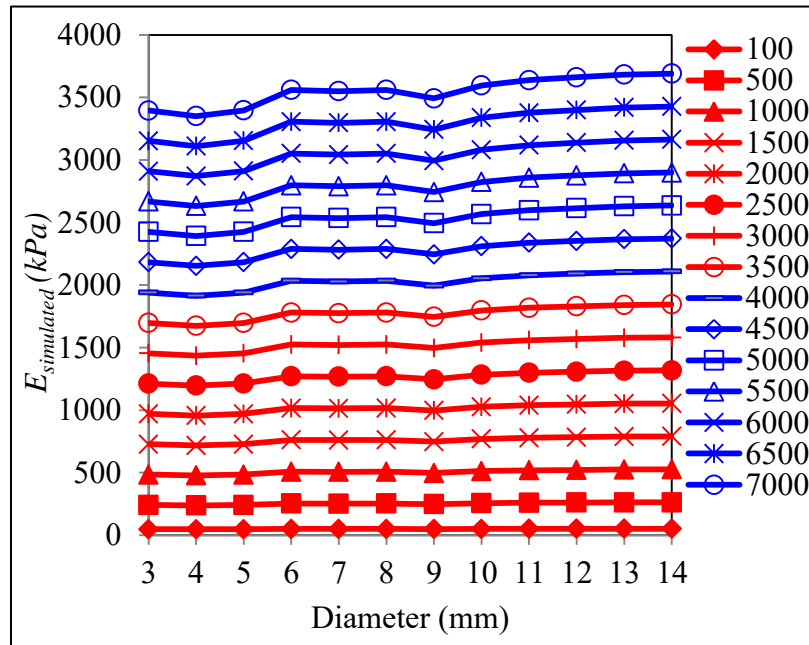
Figure 3.10. Simulation results of (a) the tissue strain at the tissue-sensor interaction surface across x-y plane; the z-displacement distribution with an indentation depth input of 0.64mm occurring at (b) the tissue-probe interaction surface on the costal cartilage exterior surface across the x-y plane, and (c) top surface of the transducer array below the built-in probe across x-y plane.

3.3.4.2. Numerical Simulation Results and Discussion

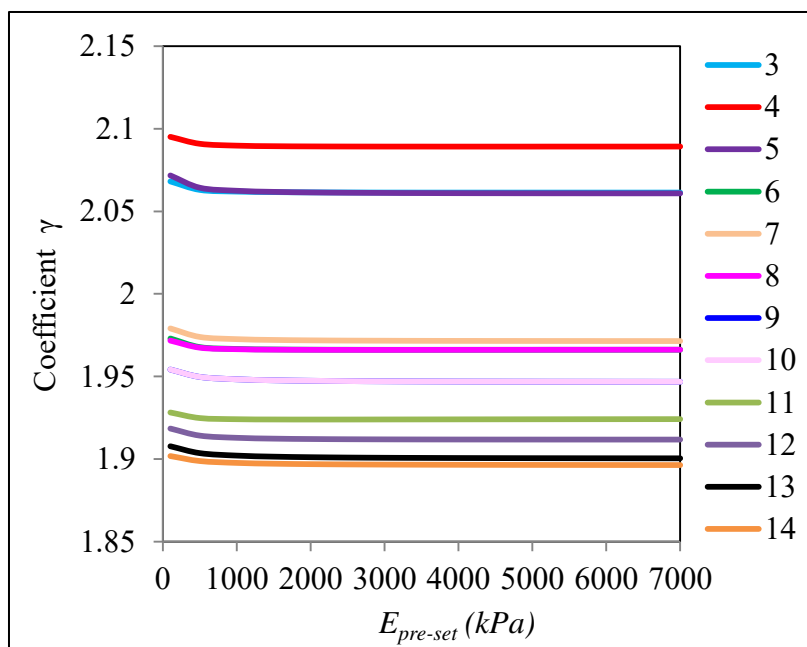
Figure 3.11(a) illustrates simulated CC elasticity, which is equivalent to the measured CC elasticity in the experiment, as a function of the CC diameter at different pre-set CC elasticity ranging from 100kPa-7000kPa. It is clear that the simulated CC elasticity goes up slightly with CC diameter when the CC diameter is smaller than 6mm. However, when the CC diameter is larger than 6mm, the simulated CC elasticity is relatively stable. The probe-tissue interaction can be considered as a flat-ended probe on a semi-infinite elastic medium at a large CC diameter since the CC diameter is much larger than the height of the built-in probe. However, when the CC diameter is close to the probe's height, this FEM will cause more errors and leads to inaccurate simulated CC elasticity. In the other words, when the CC diameter is small and in the range of 3mm-6mm, the simulated CC elasticity has larger differences with the pre-set CC elasticity. However, when the CC diameter is large and in the range of 6mm-14mm, the difference between the simulated and pre-set CC elasticity becomes smaller with the increase of CC diameter. The simulation results show that with small CC diameter ($h_t < 6\text{mm}$), the constraint at the bottom surface of the CC sample, equivalent to a rigid substrate, plays an effect on the simulated CC elasticity; while with a large CC diameter ($h_t \geq 6\text{mm}$), the bottom boundary has less influence on the simulated CC elasticity, due to its large distance from the sensing-plates. These simulated results can also be represented by the compensation coefficient as a function of pre-set CC elasticity as shown in Figure 3.11 (b). The compensation coefficient drops at low pre-set CC elasticity ($E_t \leq 500\text{kPa}$) and stabilizes at high pre-set CC elasticity ($E_t > 500\text{kPa}$), no matter how the CC diameter varies. When the CC diameter is smaller than 6mm, the compensation coefficient is much larger than the one with a larger CC diameter ($h_t \geq 6\text{mm}$), which leads to the same conclusion as Figure 3.11 (a). Overall, the simulated CC elasticity does not vary much with the change of the CC diameter. Thus, the numerical results are only used for validating that our

sensor is immune to the measured sample thickness. In addition, the values of pre-set CC elasticity are almost two times larger than the values of simulated CC elasticity. This is simply because the CC is considered as elastic material while the CC is viscoelastic material in real-life. Thus, the measured CC elasticity in the experiment does not need to be adjusted according to the simulation results.

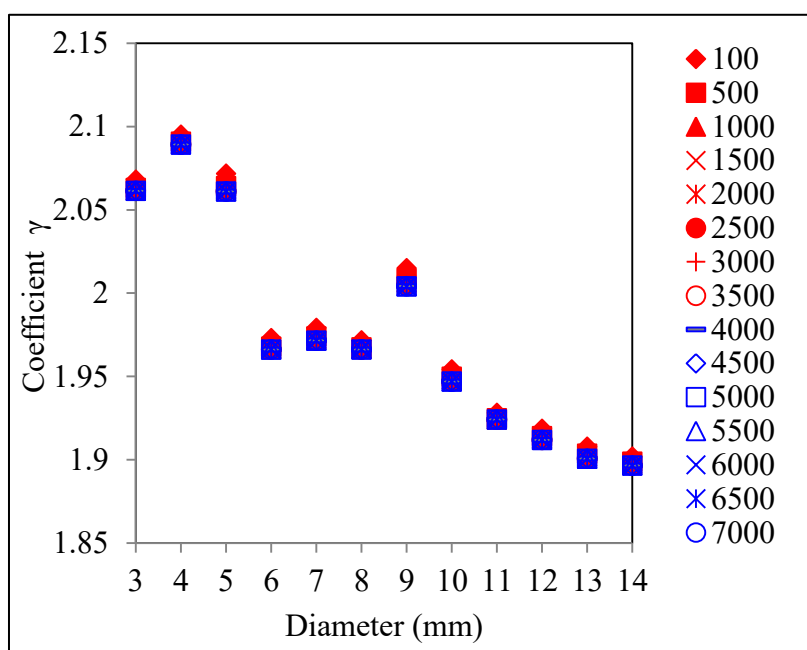
Figure 3.11(c) indicates the compensation coefficient as a function of CC diameter at different pre-set CC elasticity. As can be seen from the figure, no matter how the pre-set CC elasticity varies, there is a strong linear relationship between the CC diameter and the compensation coefficient. Although the compensation coefficient is relatively large with a small CC diameter and has more errors according to Figure 3.11(a), but overall it does not change much with the variation of the CC diameter.



(a)



(b)



(c)

Figure 3.11 Simulation results of (a) simulated CC elasticity, which are equivalent to the measured CC elasticity, as a function of CC diameter in the range of 3mm-14mm (100-7000: pre-set CC elasticity, kPa), and compensation coefficient, γ , as a function of (b) pre-set CC elasticity in the range of 100kPa-7000kPa (3-14: CC diameter, mm) at different CC diameters, and (c) CC diameter (h_i : 3mm-14mm) at different pre-set CC elasticity (E_i : 100kPa-7000kPa). (100-7000: pre-set CC elasticity, kPa)

3.3.5. Measured Results and Discussion

3.3.5.1. Conformity to the curved tissue surface

Figure 3.12 compares the difference in original recorded data between the sensor without a built-in probe and the sensor with a built-in probe. By combining these original recorded data with the pre-defined indentation depth input, we can get the spatially distributed instant and relaxed sensor deflections along the transducer array as a function of the indentation depth, as shown in Figure 3.13.

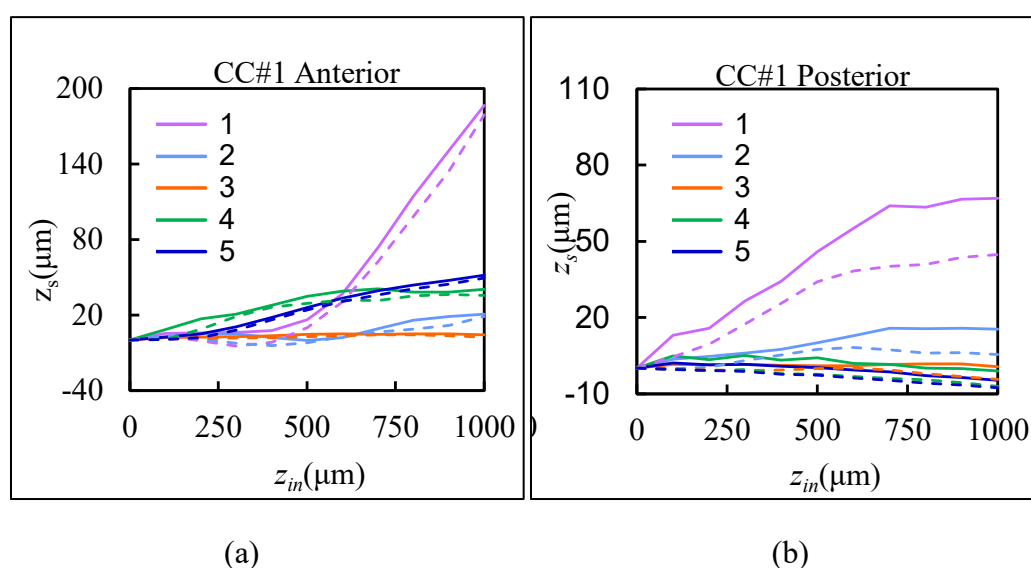


Figure 3.12. Original recorded data in a mechanical measurement: sensor deflection at the locations of the five transducers (1~5) as a function of time, in response to the pre-defined indentation depth input (a) CC #1 Anterior (b) CC #2 Anterior. (1-5: sensor deflections for first measurement at transducer 1-5)

Figure 3.13 shows the spatially distributed sensor deflection as a function of indentation depth of CC #2 at different locations. The corresponding results on CC #3 are omitted, due to their similarity. Noticeably, uncertainty in the contact point varies among the four measurements. All the measured deflection-depth relations are smooth and the difference in sensor deflection among the locations of the transducers is trivial, indicating great conformity of the probe to a tissue region, except the relatively large difference in sensor deflection between

the fourth transducer and the rest of the transducers at the posterior surface, which was caused by its associated interface electronics. The measured results on the posterior surface of CC#2 are obtained by excluding the fourth transducer later on.

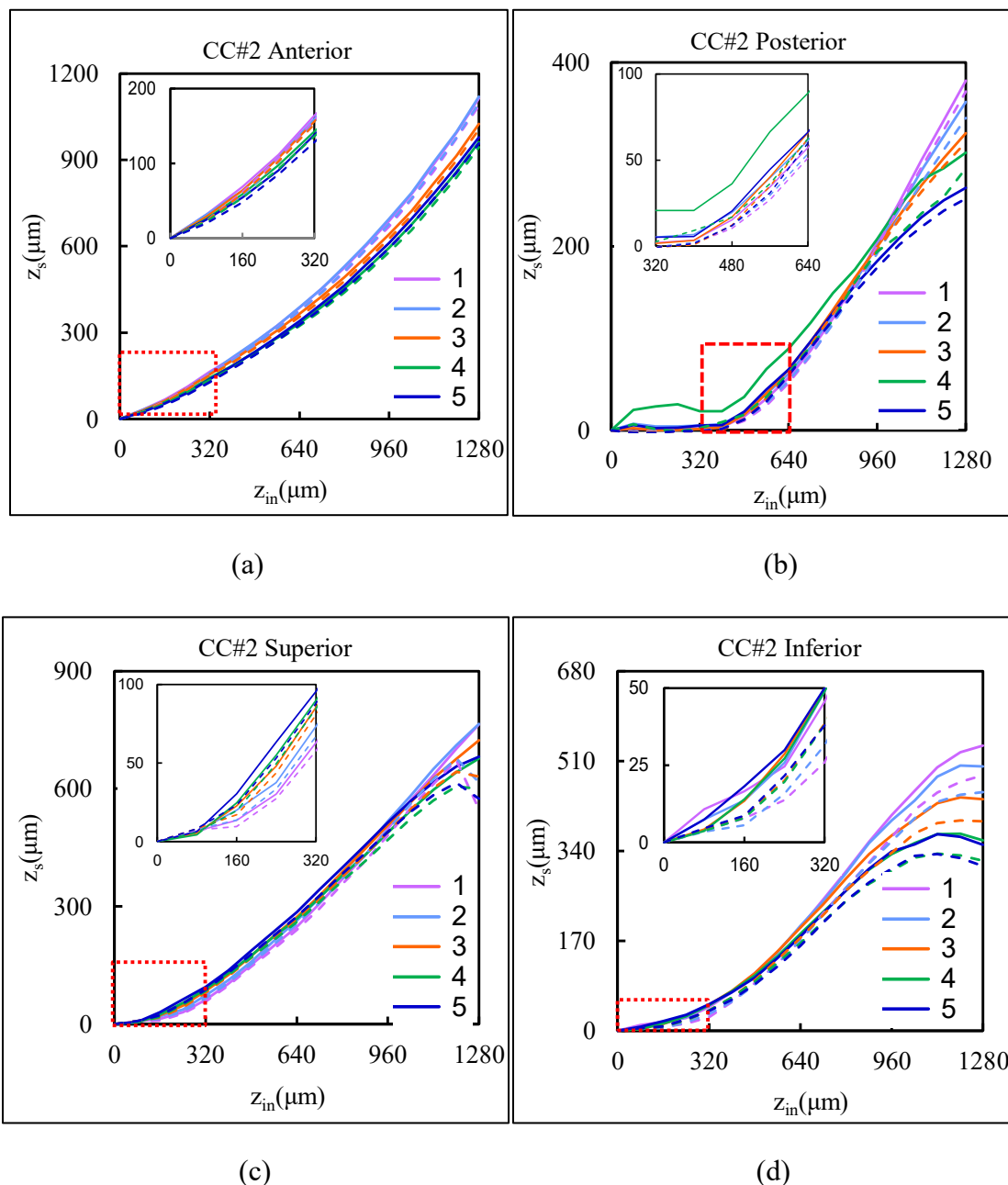


Figure 3.13. The spatially distributed sensor deflection as a function of the indentation depth measured using the sensor with a built-in probe (solid line: instant values; dashed line: relaxed values) (a) anterior surface (b) posterior surface (c) superior border (d) inferior border of CC #2. (1-5: sensor deflections for first measurement at transducer 1-5)

In the low indentation range, the probe is not in full contact with the tissue region, due to its curved surface, and thus the deflection-depth relation is relatively rough. As the indentation depth increases, the probe conforms to the curved tissue surface and achieves full contact with the tissue region. In the middle indentation range, the contact area remains unchanged, and the sensor deflection solely arises from the tissue stiffness. In the high indentation range, the sensor operates beyond its linear range and causes nonlinearity in the deflection-depth relation, as shown in Figure 3.13(a). In Figure 3.13(b), (c), and (d), slippage gradually happens at the indentation depth of $\sim 0.88\text{mm}$ at the posterior surface, $\sim 1\text{mm}$ at the superior border and $\sim 0.8\text{mm}$ at the inferior border of CC #2, respectively, so that the sensor deflection starts to diverge among the locations of the transducers.

The curved tissue surface will affect the spatially distributed sensor deflection to a relatively low extent, due to the small contact area. Meanwhile, tilt misalignment between the probe and a tissue surface is unavoidable, and translates to either an increasing or decreasing trend in the spatially distributed sensor deflection along the transducer array. As such, the spatial variation in the sensor deflection is believed to be a combination of curved tissue surface and tilt misalignment between the probe and the tissue surface. As shown in Figure 3.13, the very slight spatial variation in the sensor deflection indicates a mild curved tissue surface and a small tilt misalignment.

Uncertainty in contact point can be alleviated by using the measured deflection-depth slope. Given conformity and thus constant contact area, the average sensor deflection from the five transducers alleviates the measurement errors from tilt misalignment, and therefore is used to derive mechanical properties of the CC samples in the following section. According to Equation 3.2, the reaction force of a tissue region can be obtained from the average sensor

deflection. In summary, the built-in probe is used for achieving the conformity, and the transducer array is used for both ensuring the conformity and obtaining the reaction force in a measurement.

3.3.5.2. Measured mechanical properties

Figure 3.14 shows the average sensor deflection as a function of the indentation depth at the four locations of CC #2 and CC #3. As discussed earlier, the sensor deflection is determined by the tissue's mechanical properties only in the middle indentation range. Therefore, only the data in the middle indentation range are used for deriving the tissue's mechanical properties. Due to the variation in contact point misalignment, the middle indentation range used for extracting the deflection-depth slope varies among the measurements. The difference in the measured deflection-depth slope among the four locations of each sample is quite noticeable. In CC #2, the superior border and anterior surface exhibit much higher deflection-depth slopes than the posterior border. In CC #3, the inferior border registers the highest deflection-depth slope, and the rest of the three locations reveal similar deflection-depth slopes. As shown in Figure 3.5(b), the superior and inferior borders of CC #3 are more curved than the anterior and posterior surfaces, and thus slippage of the probe abruptly happens at these two locations.

Figure 3.15 illustrates the compression stress as a function of time for the two samples. The maximum compressive stress experienced by them is in the range of 0.1MPa ~ 0.4MPa. They exhibit stress relaxation behavior at each incremental depth. The stress relaxation behavior in Figure 3.15 is further quantified as the normalized relaxation, as shown in Figure 3.16. The indentation depth range in the figure is chosen for illustrating valid data only. All the locations of the two samples reveal a decreasing trend of the normalized relaxation with the indentation depth in the range of 80~240 μ m and become stabilized in the range of 240 μ m~480 μ m, except the

inferior border of two samples. As for CC#2, the normalized relaxation at anterior/posterior surfaces and superior border exhibit a similar decreasing trend. The normalized relaxation at the inferior border is well above those of the rest of the three locations. As to CC#3, the anterior/posterior surfaces and superior border also register a similar decreasing trend of the normalized relaxation with the indentation depth, while the inferior border registers a much lower normalized relaxation than the rest of the three locations.

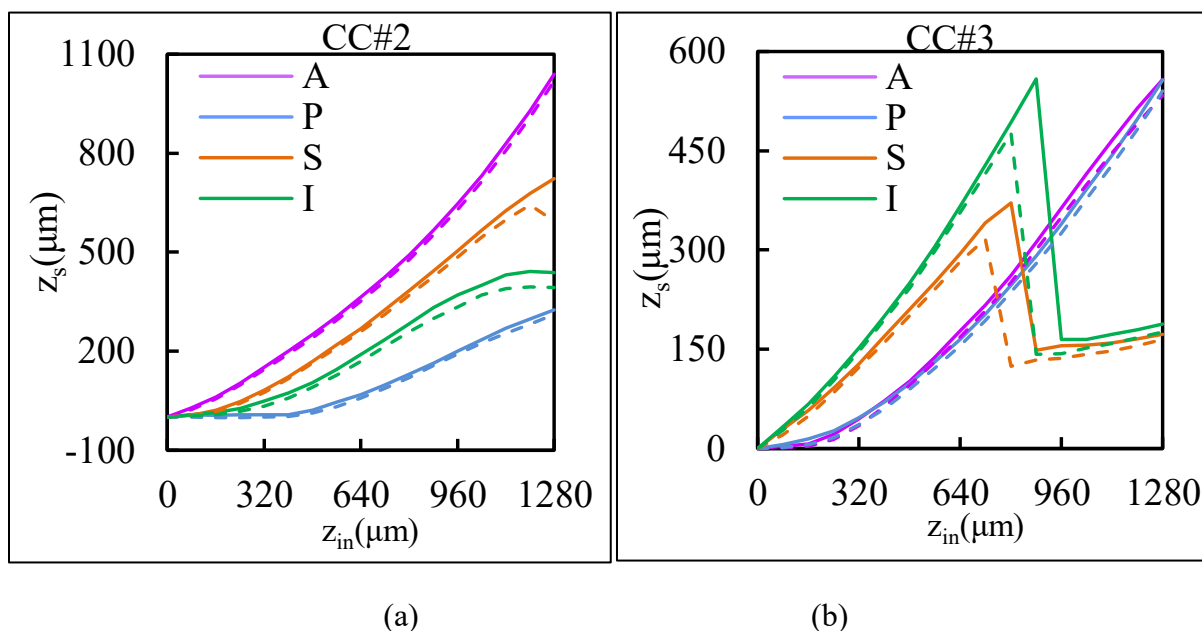
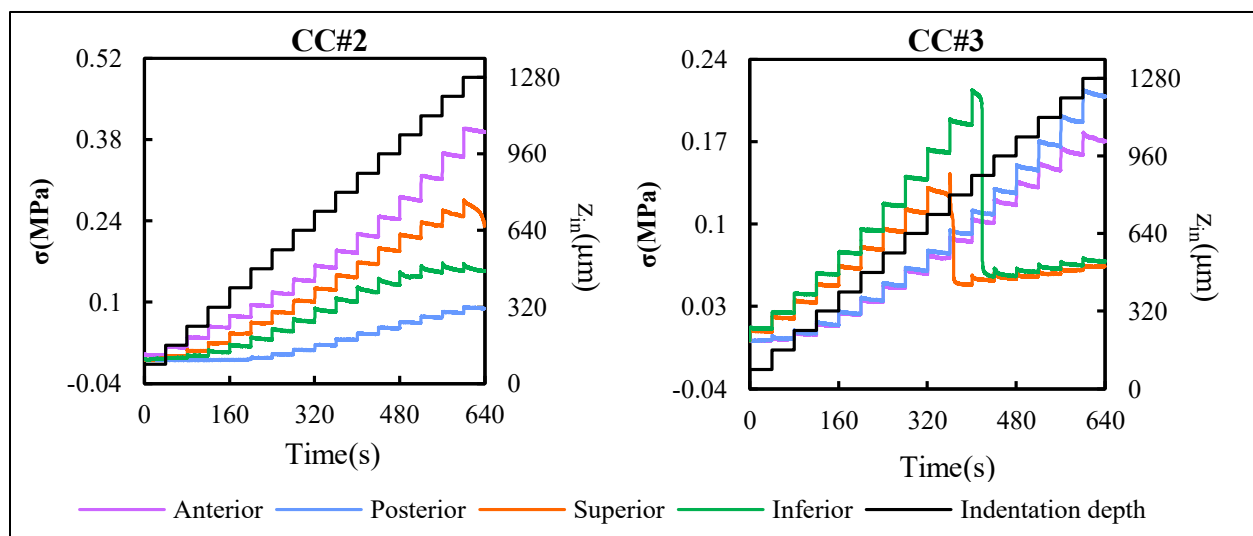


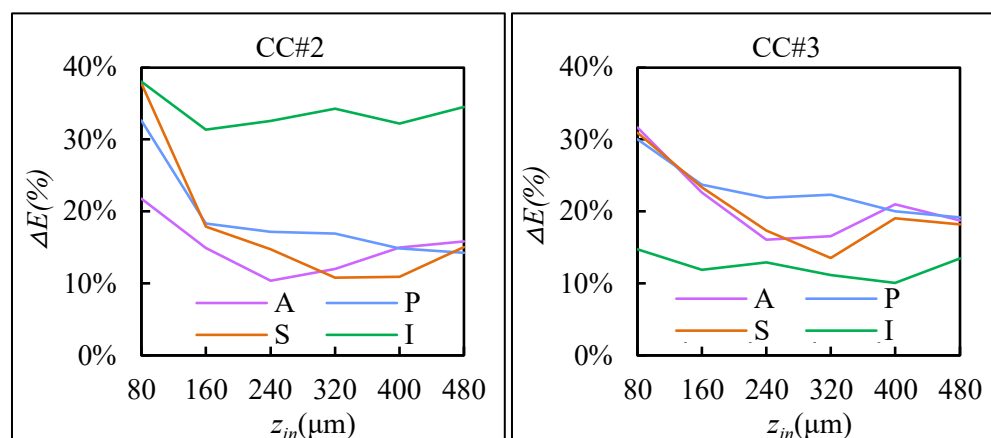
Figure 3.14. Sensor deflection versus the indentation depth (solid line: instant values; dashed line: relaxed values) (a) CC #2 (b) CC #3. (A: Anterior; P: Posterior; S: Superior; I: Inferior)



(a)

(b)

Figure 3.15. Compressive stress as a function of time (a) CC #2 (b) CC #3. (A: Anterior; P: Posterior; S: Superior; I: Inferior)



(a)

(b)

Figure 3.16. Normalized relaxation as a function of the indentation depth (a) CC #2 (b) CC #3 (A: anterior, P: posterior, S: superior, I: inferior)

Table 3.2 summarizes the measured mechanical properties at the four locations of CC #2 and CC #3. The table also lists the measurement errors for the measured instant deflection-depth slopes, the tissue instant stiffness, and the tissue instant indentation modulus. The normalized relaxation is the average value over the indentation depth range of 240 μm ~480 μm for all the locations. The anterior surface and inferior border are convex, and the posterior

surface and superior border are concave. The measured values are correlated neither to the curved shape nor to the tissue height. Overall, the instant indentation modulus and the normalized relaxation vary with the locations of each sample. The obtained instant indentation modulus of the two samples is in the range of 0.35MPa~0.92MPa, with CC #2 being stiffer than CC #3. The biological composition and structure of CC tissues vary among different locations of the same cartilage segment and different CC segments for adapting to their local biomechanical environments in the ribcage. As such, the difference in measured mechanical properties among the four locations of each sample and between the two CC samples from different ribs is reasonable.

No related data can be used for comparing with the values in Table 3.2, since mechanical measurements on the exterior surface of human CC, either healthy or PC, have not been reported in literature. The study closest to this work is the one conducted by Lau et al[1], where the reported instant modulus was roughly 5.2MPa measured on the cross-sections of human healthy CC disks from ribs of the upper thoracic region [1]. While the measured results on CC disks are dictated by the interior region (higher levels of aggrecan) of CC tissues and are associated with low tensile loading *in vivo* along the cartilage length, our results mainly arise from the peripheral region (lower levels of aggrecan) [52] and manifest the biomechanical environments for CC growth and assembly *in vivo* via oxygenation, nutrient and waste exchange.

Table 3.3 Measured mechanical properties of CC #2 and CC #3.

CC#	Parameters	Symbol	Anterior	Posterior	Superior	Inferior
CC#2	Instant deflection-depth slope	$\hat{z}_{instant}$	0.560±0.017	0.399±0.009	0.498±0.024	0.530±0.012
	Instant tissue stiffness	$k_{instant}$ (N·m ⁻¹)	1224.3±85.2	472.7±17.2	951.4±91.8	1085.3±50.9
	Instant tissue indentation modulus	$E_{instant}$ (kPa)	462.2±32.2	178.5±6.5	359.2±34.7	409.7±19.2
	Normalized relaxation	ΔE (%)	13.3%	15.8%	12.9%	33.4%
	Tissue height	h_t (mm)	7	7	14	14
	Compensation coefficient	γ	1.98	1.98	1.84	1.84
CC#3	Instant deflection-depth slope	$\hat{z}_{instant}$	0.463±0.013	0.392±0.011	0.438±0.013	0.546±0.015
	Instant tissue stiffness	$k_{instant}$ (N·m ⁻¹)	830.0±44.1	618.7±27.5	749.6±40.2	1156.0±72.0
	Instant tissue indentation modulus	$E_{instant}$ (kPa)	313.4±16.7	233.6±10.4	283.0±15.2	436.4±27.2
	Normalized relaxation	ΔE (%)	18.1%	20.8%	17.0%	12.4%
	Tissue height	h_t (mm)	7.5	7.5	14	14
	Compensation coefficient	γ	1.97	1.97	1.84	1.84

3.4. Conclusion

In this chapter, a tactile sensor with a built-in probe is utilized to achieve conformal mechanical measurement of CC at its exterior surface. Upon pressing the sensor against a cartilage exterior surface with a pre-defined indentation pattern, the built-in probe conforms to the curved cartilage surface first and then the mechanical properties of the cartilage tissue translate to the spatially distributed sensor deflection along the transducer array. The conformity to a curved cartilage surface is validated by the spatial variation in the sensor deflection.

The related theory is established to derive the tissue instant indentation modulus and normalized relaxation from the measured deflection-depth slopes of a CC specimen. As a result, the relation between the probe, sensor, and tissue is clearer. In summary, The sensor stiffness, k_s , must be lower than the tissue stiffness, k_t ($k_s < k_t$), so that the maximum sensor deflection, z_{s_max} , can be tailored to be a little lower than its adjusted maximum linear deflection range, $z_{s_linear} - \delta_s$, for keeping the collected data to cover the full linear deflection range of the sensor. The probe height, h_p , is a tradeoff between accommodation of the highest thickness, δ_t , on a curved tissue

surface, and avoidance of buckling ($\delta_p < h_p < h_{p_buckling}$). As to CC tissues with their elasticity range of 1MPa-7MPa, the highest tissue stiffness is seven times the lowest tissue stiffness. The sensor stiffness targeted for the CC in the higher elasticity end will cause the collected data on the CC in the lower elasticity end to be located in the lower linear deflection range of the sensor, which translates a larger amount of experimental errors. However, the sensor and probe stiffness in the lower end will fail to capture the mechanical properties of CC with its elasticity in the higher end.

Then, a numerical study is established to provide a feasible method to examine the effects of CC parameters on the measured CC elasticity via this tactile sensor of a built-in probe. The FEM analysis results show that the effects of CC parameters on the measured CC elasticity are more significant for the CC with small diameter and low pre-set CC elasticity. Thus, the numerical results suggest that the indentation-relaxation testing is more reliable in measuring CC with larger CC diameter and pre-set CC elasticity. The FEM analysis results also reveal the relation between the compensation coefficient and CC diameter. By multiplying this compensation coefficient to the instant indentation modulus which is calculated from the theoretical model, the true CC elasticity can be obtained. Please note that this compensation coefficient is only suitable for this tactile sensor with a 0.5mm×5mm×3mm built-in probe.

A proof-of-concept experimental study is carried on two human PC CC segments. As compared with the measured results of the PC CC by the sensor without a built-in probe, the measurements on two human PC CC segments validate the feasibility of a tactile sensor with a built-in probe for conformal mechanical measurements of CC at its exterior surface. Based on the recorded relation of average sensor deflection to indentation depth of the two samples measured using the sensor with a built-in probe, the CC instant indentation modulus and

normalized relaxation of the two samples are derived and found to vary significantly among the anterior/posterior surfaces and superior/inferior borders at the same position of each sample.

Overall, in this chapter, the qualitative, numerical and experimental studies of this tactile sensor with a built-in probe are thoroughly presented. The performance characterization of the tactile sensor with and without a built-in probe is also discussed carefully.

CHAPTER 4

MEASURED MECHANICAL PROPERTIES OF PORCINE COSTAL CARTILAGE

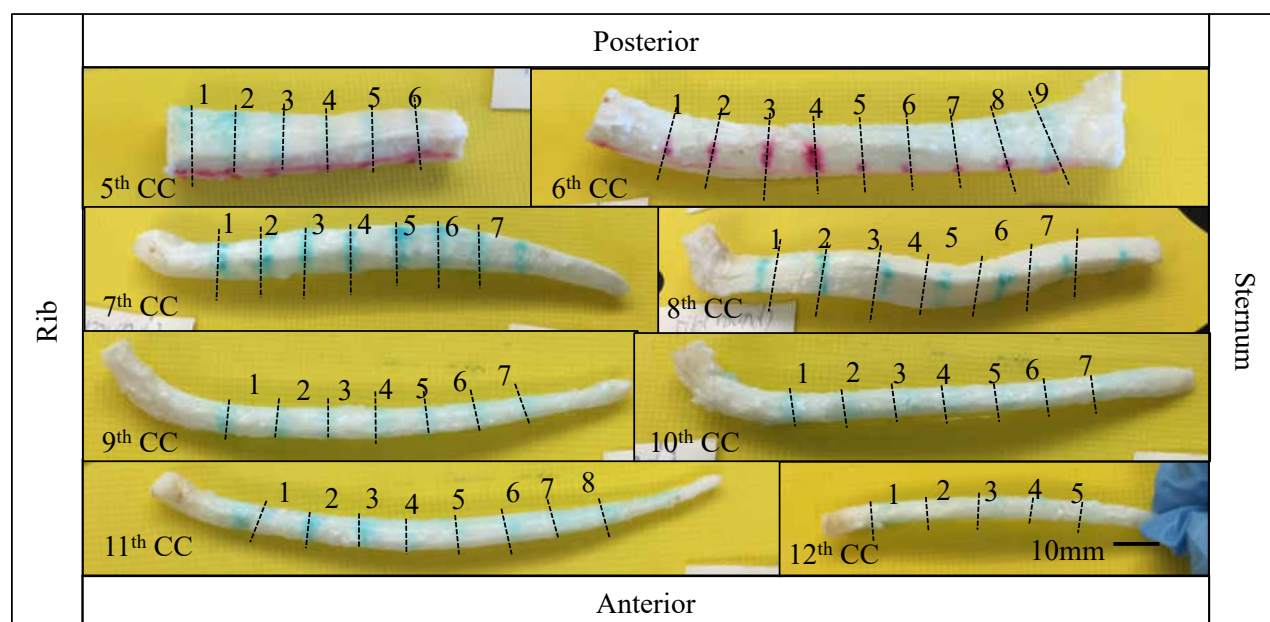
This chapter focuses on determining the mechanical properties at the exterior surface of porcine Costal Cartilage (CC) and examines how they vary with their anatomical sites of CC in the ribcage via the tactile sensor with a 5mm×0.5mm built-in probe discussed in Chapter 3. The tactile sensor used in this chapter is still sensor B. The sample preparation, results and discussions are elaborated in detail. The experimental setup, pre-defined parameters and data analysis for indentation pattern are presented in brief.

4.1. Sample Preparation

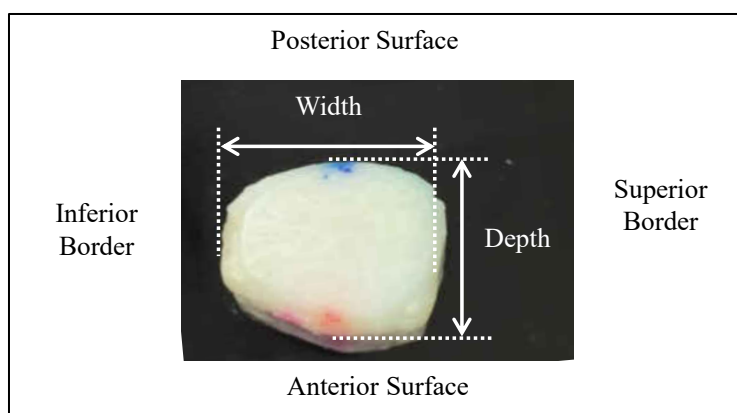
All the CC samples were harvested from right lower ribcage of an 18-month-old female pig by a local slaughtering house (Pendulum Fine Meats, Norfolk, VA) within 48 hours of slaughter. The samples were stored frozen at -20°C until testing at which point, they were thawed in Ringer solution at 4°C for 2 hours first and then soaked in a bath of PBS at room temperature for 30 minutes before mechanical testing. The whole CC segments from the 5th to 12th ribs were dissected at room temperature. All muscles, fat, and perichondrium were removed from the ribs, leaving only the cartilage tissue. The samples were stored in PBS throughout the sample preparation at room temperature and kept moist throughout the measurement via PBS spray. (b)

Figure 4.1(a) shows the whole 5th ~ 12th CC segments, where the measured locations were marked in red or blue. Along the length of a whole CC segment, the locations for measurement were 10mm apart for all the CC segments. The anterior surface and posterior surface at each location for measurement were tested, since a tissue in vitro loses the capability

of full recovery and further testing at the same location gives rise to results quite different from the first testing [47].



(a)



(b)

Figure 4.1 Pictures of (a) the whole porcine 5th ~ 12th CC segments of right ribcage from an 18-month-old female pig with the locations for measurement being marked in blue or red at their exterior surface and with dash lines in the pictures (b) CC transverse cross-sections (5th CC: Location 3) with the definition of depth and width.

The geometries of the CC segments were assessed after being soaked in PBS for two hours after conformal indentation testing. The transverse cross-section geometry of the CC segments at each measured location was assessed as the depth (measured from the anterior

surface to posterior surface) and the width (measured from superior border and inferior border), as shown in (b)

Figure 4.1(b). Table 4.1a summarizes the length of the CC segments (from the first measured location to the last measured location) and their average width and average depth from all the measured locations, and their average depth/width ratio for quantifying their flatness and roundness. Table 4.1 (b) shows the depth, width, and the relative depth/width ratio at each location for measurement along the length of the CC segments.

Table 4.1 The geometrical parameters and their values of the whole porcine 5th ~12th CC.

(a)

CC segment #	Length (mm)	Width (mm)	Depth (mm)	Depth/Width ratio (%)
5 th CC	65.8	14.72±0.49	12.42±1.92	84.4
6 th CC	103.9	12.30±4.63	11.03±0.54	89.7
7 th CC	79.3	12.62±0.70	8.78±0.75	69.6
8 th CC	80.7	12.20±1.23	11.41±2.18	93.5
9 th CC	79.8	9.67±1.20	5.79±0.28	59.9
10 th CC	82.2	8.23±0.79	5.30±1.02	64.4
11 th CC	96.6	6.30±1.03	5.23±0.62	83.0
12 th CC	58.5	6.82±0.49	4.52±0.14	66.3

(b)

CC segment #	Geometrical Parameters	L#1	L# 2	L# 3	L# 4	L# 5	L# 6	L# 7	L# 8	L# 9
5 th CC	Width (mm)	15.1	15.2	15.2	14.8	14.3	13.7	--	--	--
	Depth (mm)	14.3	12.8	12.4	11.8	11.7	11.4	--	--	--
	Depth/Width ratio (%)	94.7	84.1	81.3	80.0	82.2	83.5	--	--	--
6 th CC	Width (mm)	12.3	10.5	12.5	10.3	10.7	16.9	14.0	12.0	9.9
	Depth (mm)	15.1	13.6	12.7	11.6	11.4	11.4	10.6	10.1	11.2
	Depth/Width ratio (%)	108.8	84.0	79.2	66.5	65.4	67.1	75.6	84.2	113.2
7 th CC	Width (mm)	11.9	12.3	12.5	12.7	13.3	13.1	11.8	--	--
	Depth (mm)	8.3	9.3	9.5	9.5	8.6	8.3	7.5	--	--
	Depth/Width ratio (%)	69.5	75.5	76.0	74.8	64.9	63.1	63.7	--	--
8 th CC	Width (mm)	13.1	12.6	12.7	12.2	13.4	13.1	9.3	--	--
	Depth (mm)	9.5	13.5	136	11.6	11.0	9.9	8.8	--	--
	Depth/Width ratio (%)	73.1	107.1	107.3	95.3	82.1	76.0	95.2	--	--
9 th CC	Width (mm)	9.3	10.5	10.7	10.9	10.1	8.7	7.1	--	--
	Depth (mm)	6.0	5.8	5.8	5.7	5.8	6.1	5.6	--	--
	Depth/Width ratio (%)	64.4	55.3	54.6	52.3	57.1	69.8	78.1	--	--
10 th CC	Width (mm)	8.3	8.1	8.7	9.0	8.8	7.9	6.9	--	--
	Depth (mm)	6.3	6.0	6.3	5.7	5.1	4.5	4.1	--	--
	Depth/Width ratio (%)	76.1	74.3	73.0	63.3	58.5	57.1	59.5	--	--
11 th CC	Width (mm)	6.7	7.7	7.2	7.3	7.2	6.6	4.9	4.5	--
	Depth (mm)	5.5	5.9	5.8	5.6	4.8	5.3	5.9	3.9	--
	Depth/Width ratio (%)	81.6	77.1	80.8	76.8	66.8	80.9	118.8	86.9	--
12 th CC	Width (mm)	6.8	7.3	7.3	6.7	6.0	--	--	--	--
	Depth (mm)	4.6	4.7	4.6	4.5	4.2	--	--	--	--
	Depth/Width ratio (%)	68.1	64.3	63.4	66.7	69.7	--	--	--	--

4.2. Experiment Method

The experiment setup is exactly the same as the one used in Section 3.3.2. In brief, a custom experimental setup was built to conduct conformal indentation testing on the exterior surface of the porcine CC segments via a tactile sensor with a 5mm×0.5mm built-in probe. A CC segment was fixed by grips at its two ends, after rotating it until its anterior surface or posterior surface faced upward. A micropositioner was connected to the sensor for controlling its motion.

The associated accessories were used to operate the sensor and record its outputs. After visually aligning the built-in probe of the sensor with the exterior surface of a CC segment, the position and orientation of the sensor were further manually adjusted for improved alignment of the built-in probe surface with the CC exterior surface, by monitoring the outputs of the sensor. After alignment, a cycle of multiple indentation-relaxation steps was exerted on the CC exterior surface, and its time-dependent response was captured by the sensor as the time-varying sensor deflection, $z_s(t)$. A Lab-VIEW program was written to carry out the measurements and record the data at a sampling rate of 500Hz. In the indentation pattern of the testing protocol as elaborated in Figure 2.10, the ramp speed, incremental step depth and hold time were $\dot{z}=0.2\text{mm}\cdot\text{s}^{-1}$, $z_{\text{step}}=80\mu\text{m}$, and $t_{\text{hold}}=40\text{s}$, respectively. As such, each indentation step was followed by a 40s period of stress relaxation until the final indentation depth of 1.28mm was reached.

4.3. Data Analysis

According to the Section 3.3.3 and 3.3.4, instant indentation modulus and normalized relaxation of CC can be calculated from Equation 3.23 and 3.20, respectively. In the low indentation range, the built-in probe achieved full contact with the tissue region underneath, and in the high indentation range, the sensor operated beyond its linear range and caused non-linearity. As such, only the collected data in the middle indentation range was utilized to derive the mechanical properties of the CC segments, as detailed in our previous chapter. Accordingly, compressive stress-relaxation curves, in response to the multi-step indentation-relaxation testing protocol is presented in Figure 4.2 and indicates the feasibility of using the normalized relaxation to quantify the viscosity of CC.

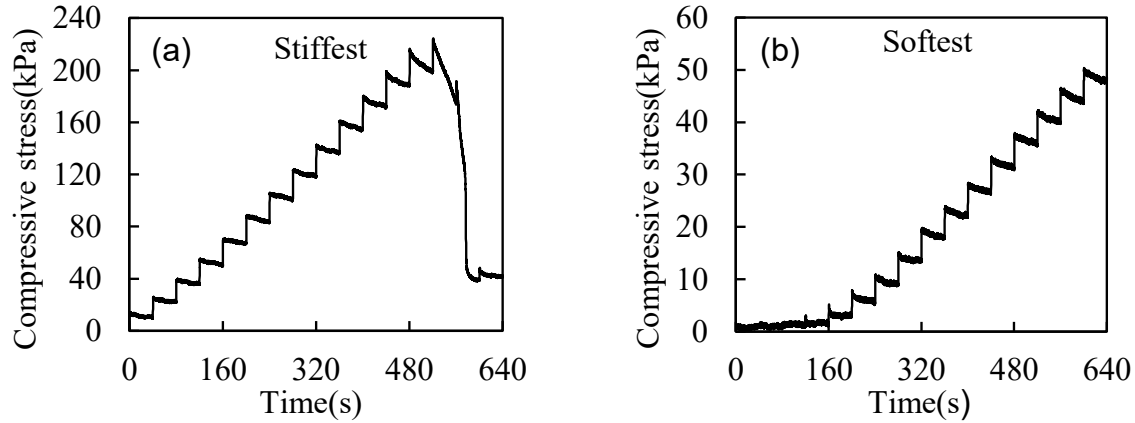


Figure 4.2 The measured compressive stress of CC as a function of time, in response to the multi-step indentation-relaxation testing protocol with $z=80\mu\text{m}$, $\dot{x}=0.2\text{mm}\cdot\text{s}^{-1}$ and $t_{\text{hold}}=40\text{s}$ (a) posterior surface of the 5th CC segment at Location 1 (the stiffest location) (b) anterior surface the 9th CC at Location 3 (the softest location).

4.4. Results

4.4.1. Geometries

As illustrated in Figure 4.1(a), because of the large, abrupt curvature at the costochondral joint of these segments, the measurements were conducted at the locations away from the costochondral joint, except the 5th segment with a straight costochondral joint. The 5th ~7th CC segments are connected to the true ribs. The 5th CC has a larger transverse cross-section than the 6th and 7th segments. As compared with the 5th and 6th CC, the 7th CC is relatively flat along its length. The 5th and 7th CC exhibit some twist along their length, and the 6th CC is relatively straight. The 6th CC is longer than the 5th and 7thCC. The 8th ~ 10th CC tissues are connected to the false ribs. The 8th CC has a transverse cross-section size similar to the 6th CC. There is a sudden geometrical drop in the transverse cross-section from the 8th CC to the 9th CC. Note that the 8th CC is the most twisted and roundest one. The 9th CC is the flattest one, followed by the 10th segment. Meanwhile, the 9th and 10th CC segments are relatively straight, as compared with the rest. As floating ribs, the 11th and 12th CC both contain a smooth, slight curvature without many twists along their length. The 11th CC is much longer but less flat than

the 12th CC. Except for the 5th CC, all the rest of the CC, no matter how they are connected with true ribs, false ribs, and float ribs all show a flat trend with a decrease of CC segment number, respectively. Except for the 8th CC, the transverse cross-section geometry shows a decreasing trend with increasing CC number (from the 5th CC to the 12th CC). In addition, within the same CC segment, the 6th CC exhibits the large variation in width, and the 5th CC reveals also a large variation in depth. The 8th CC reveals large variations in both width and depth. Overall, the variation in depth/width ratio is random along the cartilage length for all the CC segments.

4.4.2. Instant indentation modulus and normalized relaxation

As shown in Figure 4.3, the first measured location of the 5th CC is close to the costochondral joint and exhibits the highest instant indentation modulus at the posterior surface. The instant indentation modulus at the posterior surface of the 5th CC varies dramatically along the cartilage length and is well above that at its counterpart at the anterior surface, which varies slightly along the cartilage length. The instant indentation modulus at both the anterior surface and the posterior surface of the 7th CC varies significantly along the cartilage length. The instant indentation modulus at the two surfaces of the 8th and 12th CC varies moderately along their length. In contrast, the instant indentation modulus at both surfaces of the 6th, 9th ~11th CC varies slightly along the cartilage length. By comparison with Table 4.1(b), the observed variation in instant indentation modulus along the cartilage length does not show any correlation with the transverse cross-section geometries. Furthermore, the average instant indentation modulus from the two surfaces at the measured locations does not show any trend along the cartilage length.

Figure 4.4 shows how the normalized relaxation varies with the indentation depth, where the measured locations and the CC segments are both arbitrarily chosen for illustration. In the low indentation range of 80 μ m~220 μ m, the normalized relaxation drops with the indentation

depth. In the indentation range of $220\mu\text{m}\sim 640\mu\text{m}$, the normalized relaxation at the two surfaces becomes stabilized. While the normalized relaxation at the anterior surface is higher than that at the posterior surface for the chosen locations of the 7th, 9th, and 10th CC, the normalized relaxation at the two surfaces at the chosen location of the 8th CC is similar.

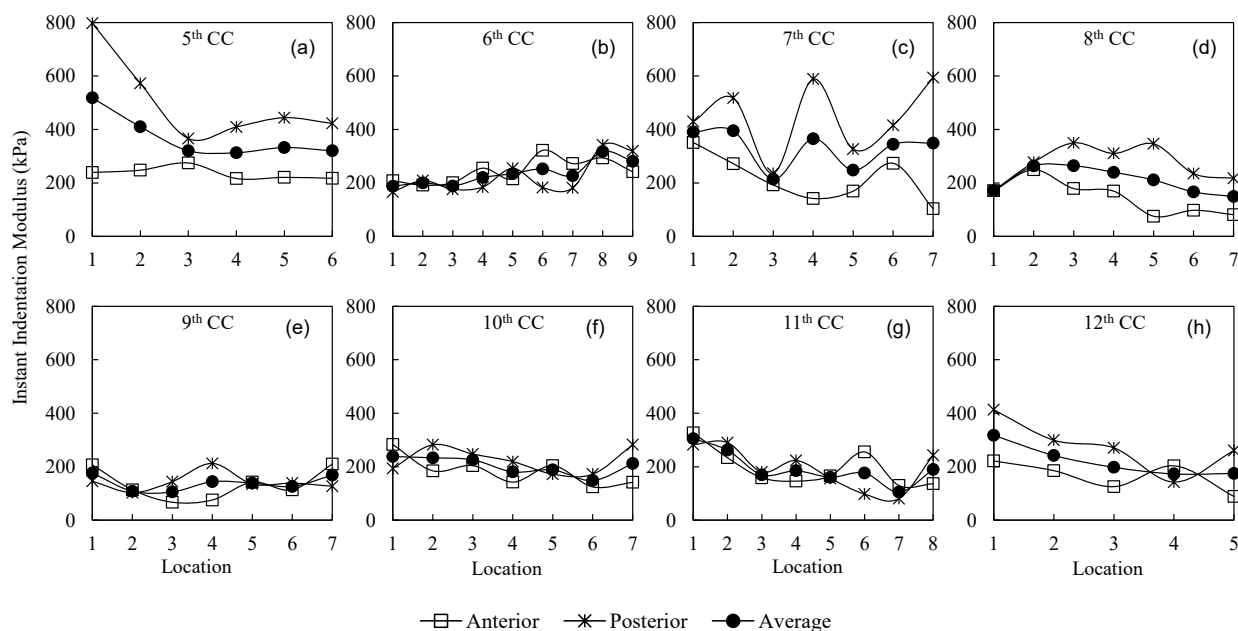


Figure 4.3 Measured instant indentation modulus at the anterior and posterior surfaces and their average at different locations along the cartilage length (from rib to sternum) of the CC segments (a) 5th CC (b) 6th CC (c) 7th CC (d) 8th CC (e) 9th CC (f) 10th CC (g) 11th CC (h) 12th CC.

We further calculate the average normalized relaxation from the two surfaces at each measured location at different indentation depths. Figure 4.5 shows how the average normalized relaxation at different measured locations varies with the indentation depth, revealing a changing trend of the normalized relaxation with the indentation depth similar to the one in Figure 4.4. Only the average normalized relaxation at location 7 of 7th CC does not show a decreasing trend with the indentation depth in the low indentation range. Because, before the measurement, the sensor is deformed by the CC already at location 7 of 7th CC. In the 5th, 9th, 11th and 12th CC, the decreasing trend of normalized relaxation with the indentation depth varies among the measured locations in the low indentation range. In contrast, in the 6th, 7th, 8th and 10th CC, this decreasing

trend is similar among the measured locations. The normalized relaxation of the 10th and 11th CC exhibits the fastest decreasing trend with the indentation depth, as compared with the others. Unlike the average instant indentation modulus, the normalized relaxation does not show a trend along the cartilage length.

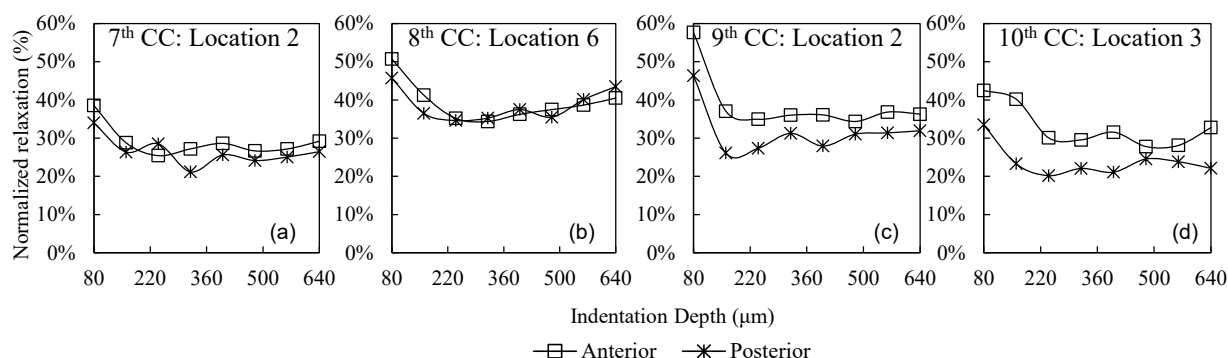


Figure 4.4 Measured normalized relaxation as a function of the indentation depth (a) 7th CC: Location 2 (b) 8th CC: Location 6 (c) 9th CC: Location 2 (d) 10th CC: Location 3.

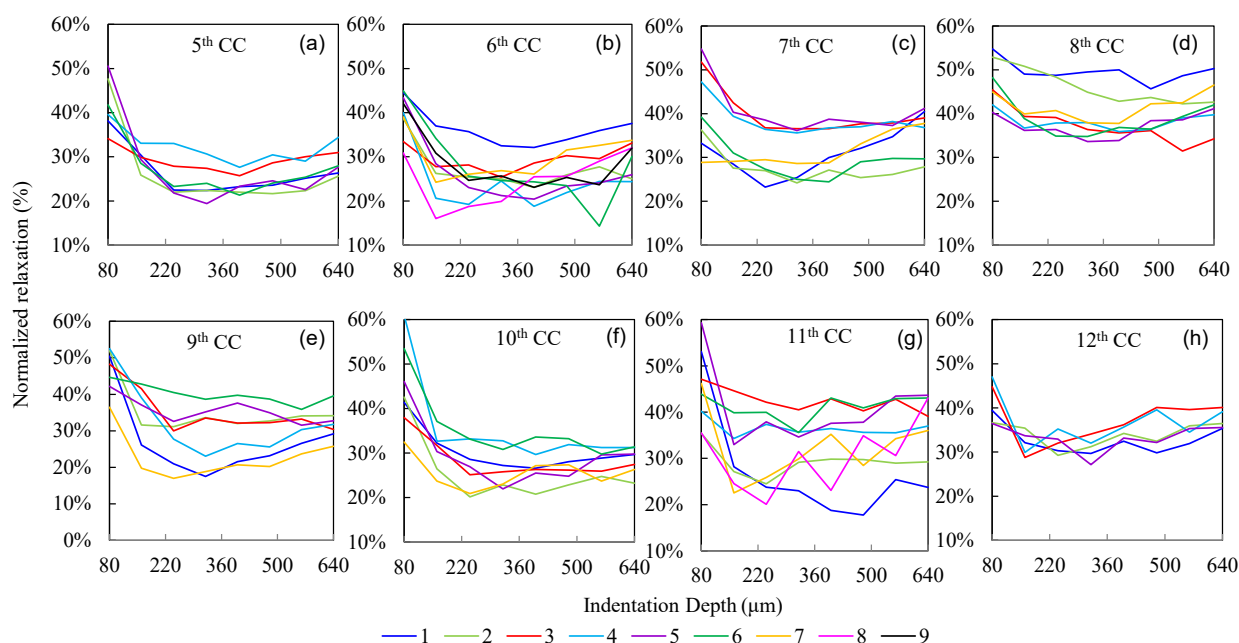


Figure 4.5 Average normalized relaxation of the anterior and posterior surface at each measured location as a function of the indentation depth (a) 5th CC (b) 6th CC (c) 7th CC (d) 8th CC (e) 9th CC (f) 10th CC (g) 11th CC (h) 12th CC.

Since the normalized relaxation becomes stabilized in the indentation range of 220 μ m~640 μ m, the average normalized relaxation from this indentation range is quantified as

the normalized relaxation of CC. Figure 4.6 illustrates how the normalized relaxation at the anterior and posterior surfaces varies along the cartilage length for the CC segments. Particularly, the normalized relaxation at the two surfaces of the 8th ~11th CC fluctuates significantly along the cartilage length. The average normalized relaxation from the two surfaces does not show any trend along the cartilage length.

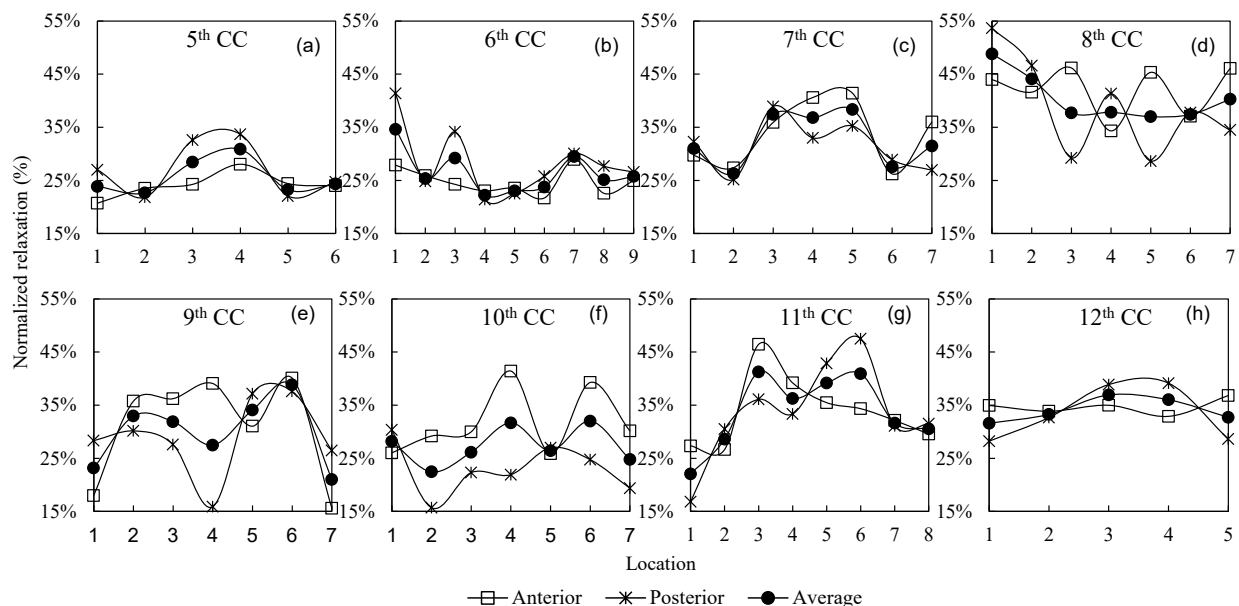


Figure 4.6 Measured normalized relaxation along the cartilage length (from rib to sternum) of the CC segments (a) 5th CC (b) 6th CC (c) 7th CC (d) 8th CC (e) 9th CC (f) 10th CC (g) 11th CC (h) 12th CC.

The instant indentation modulus at the anterior surface of all the measured locations of a CC segment is further averaged to represent the instant indentation modulus at the anterior surface of the whole CC segment. The same is calculated for the instant indentation modulus at the posterior surface of the whole CC segment. Then, the instant indentation modulus of the whole CC segment is the average of the two surfaces. As illustrated in Figure 4.7(a), the instant indentation modulus at the anterior and posterior surfaces of a whole CC segment and the instant indentation modulus of a whole CC segment vary among the CC segments. The same calculation is carried out on the normalized relaxation. As shown in Figure 4.7(b), the normalized relaxation

at the two surfaces of a whole CC segment and the normalized relaxation of a whole CC segment also vary among the CC segments.

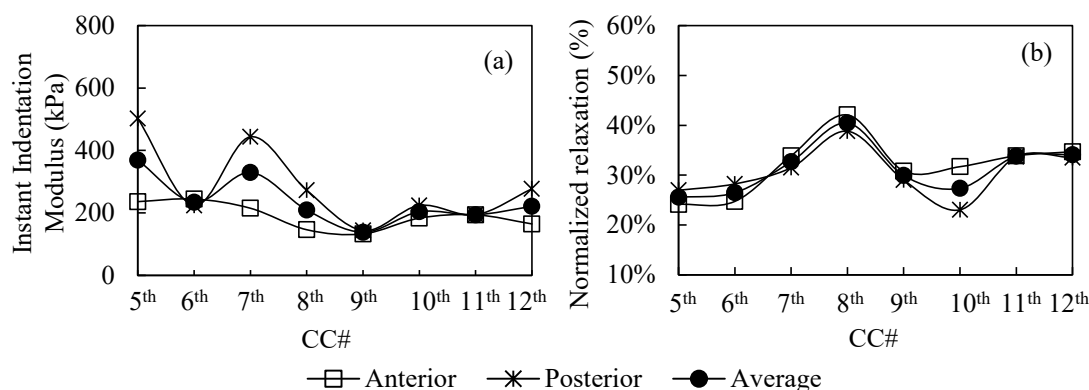


Figure 4.7. (a) Instant indentation modulus at the anterior and posterior surfaces and their average of a whole CC segment (b) normalized relaxation at the anterior and posterior surfaces and their average of a whole CC segment.

Table 4.2 summarizes the instant indentation modulus and normalized relaxation at the anterior and posterior surfaces and the average of the two surfaces of each whole CC segment. Overall, the instant indentation modulus at the posterior surface is higher than that at the anterior surface, possibly because of gravitational forces acting on porcine CC.

Table 4.2 Summary of the measured average instant indentation modulus and average normalized relaxation (a) among the atomically sites and (b) along the cartilage length of the CC segments at their exterior surface.

(a)

CC segment	Instant indentation modulus(kPa)			Normalized relaxation (%)		
	Anterior	Posterior	Average	Anterior	Posterior	Average
5 th CC	236.1	502.0	369.1	24.2	27.0	25.6
6 th CC	244.6	224.1	234.3	24.7	28.3	26.5
7 th CC	215.0	443.8	329.4	33.9	31.5	32.7
8 th CC	146.2	272.6	209.4	42.1	38.8	40.5
9 th CC	132.7	143.6	138.2	30.8	29.0	29.9
10 th CC	183.3	224.0	203.7	31.7	23.1	27.4
11 th CC	193.9	194.1	194.0	33.9	33.7	33.8
12 th CC	164.7	277.1	220.9	34.7	33.5	34.1

(b)

	CC#	5 th CC	6 th CC	7 th CC	8 th CC	9 th CC	10 th CC	11 th CC	12 th CC
$E_{instant}$ (kPa)	1	518.3	187.5	390.3	171.1	176.2	238.0	304.7	317.2
	2	410.2	200.3	394.9	263.4	108.3	233.3	261.9	242.1
	3	320.5	188.4	214.1	264.5	105.6	225.7	169.3	197.8
	4	312.9	219.9	365.2	240.0	143.9	180.7	184.8	172.9
	5	332.5	234.8	247.9	211.0	138.8	187.9	160.7	174.6
	6	320.1	252.6	344.3	166.4	126.1	148.2	176.3	--
	7	--	226.9	349.0	149.2	168.4	211.8	105.1	--
	8	--	317.7	--	--	--	--	189.5	--
	9	--	280.7	--	--	--	--	--	--
	Average	369.1	234.3	329.4	209.4	138.2	203.6	194.0	220.9
$\Delta E(\%)$	1	23.9	34.6	31.0	48.8	23.2	28.2	22.1	31.6
	2	22.7	25.4	26.3	44.1	33.0	22.4	28.6	33.3
	3	28.4	29.2	37.4	37.7	31.9	26.1	41.3	36.9
	4	30.9	22.2	36.8	37.8	27.5	31.7	36.3	36.0
	5	23.2	23.0	38.3	37.0	34.1	26.4	39.2	32.7
	6	24.3	23.7	27.5	37.4	38.8	32.0	40.9	--
	7	--	29.5	31.5	40.3	21.0	24.8	31.6	--
	8	--	25.1	--	--	--	--	30.5	--
	9	--	25.7	--	--	--	--	--	--
	Average	25.6	26.5	32.7	40.5	29.9	27.4	33.8	34.1

In Table 4.2, the three true ribs: the 5th ~ 7th CC, are stiffer than the false and floating ribs, but the 5th CC is the stiffest and least viscous CC. The 6th CC is much weaker than the 5th and 7th CC. The false ribs and the floating ribs exhibit very similar instant indentation modulus, except the 9th CC that registers as the softest CC segment. Overall, the anterior surface and the posterior surface have similar normalized relaxation, except the 10th CC that exhibits a larger difference between the normalized relaxation at its anterior and posterior surfaces. There is no significant difference in normalized relaxation among the CC segments. The 8th CC registers as the most viscous segment.

4.5. Discussion

The aim of the present study was to determine the mechanical properties of porcine CC at their exterior surface and examine how they vary with their anatomical locations. Owing to their curved exterior surface, the conformal indentation was implemented on a whole porcine CC segment via a tactile sensor with a built-in probe. As compared with CC strips and CC disks,

the structural integrity of CC was retained in our measurements for obtaining their true mechanical behavior. To alleviate misalignment errors associated with contact-point uncertainty, a multi-step indentation-relaxation testing protocol was used to obtain the time-dependent response of CC at multiple indentation depths. Then, the instant indentation modulus and normalized relaxation are immune to misalignment errors from contact-point uncertainty and can be used for comparison of mechanical properties among different anatomical sites of CC.

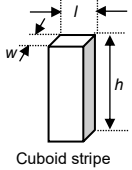
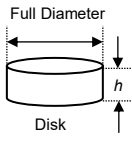
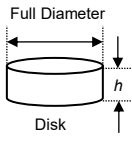
4.5.1. Comparison with the measured mechanical properties of CC in the literature

Since CC are viscoelastic, the absolute value of their instant indentation modulus varies with the ramp speed, hold time and incremental step depth. Therefore, we can only qualitatively compare our results with the related data in the literature. Our results are much higher than the elasticity of $\sim 53.7\text{kPa}$ at the exterior surface of whole embryonic CC from wild-type mice measured using unconfined compression [53]. This discrepancy can be explained by the facts that immature embryonic CC contain about twice the cellularity of mature cartilage and the elasticity of CC is species-dependent. Additionally, the embryo is suspended in a sac of amniotic fluid and not yet subjected to the rigors of gravity.

Table 4.3 summarizes the measured elasticity on porcine CC disks and strips, which quantify the mechanical properties at the CC interior region along the cartilage length. Note that rigid spherical indenters of different diameters and different testing protocols were used for CC disk measurements. Overall, the measured elasticity on the CC disks is above 1MPa and is much higher than the measured elasticity at the exterior surface of porcine CC in this work. The measured tissue-level mechanical properties of porcine CC depend on their structural constituents. In CC, chondrocytes occupy $\sim 10\%$ of the volume. Their ECM mainly consists of collagen fibril network, negatively charged proteoglycan (mostly aggrecan) and interstitial fluid.

Owing to negatively charged proteins associated with aggrecan, osmotic pressure is created in the interstitial fluid, putting collagen fibril matrix in tensile load. While collagen fibril network primarily provides tensile strength, negatively charged aggrecan provides compressive strength. While the measured results on CC disks are dictated by the interior region and are associated with low tensile loading *in vivo* along the cartilage length, our results mainly arise from the peripheral region and manifest the biomechanical environments for CC growth and assembly *in vivo* via oxygenation, nutrient, and waste exchange. Higher level aggrecan in the interior region is more resistive to compressive loading and thus gives rise to a high measured elasticity. The peripheral region near the exterior surface of CC contains lower-level aggrecan and translates to a low measured elasticity.

Table 4.3 Measured mechanical properties of porcine CC reported in the literature.

Specimen sources	Sample location	Sample shape	Sample dimension (mm)	Testing techniques	Controlled parameters	Mechanical Modulus
4-8 Weeks Porcine [25]	--	 Cuboid stripe	h=20 l=4 w=1	Three-point bending flexural test	--	$E_{\text{Bending}}=7.06\text{MPa}$
28-132 day-old female porcine (not sexual matured)[28]	--	 Disk	h=5	Indentation testing (Spherical indenter diameter:3.15mm)	Peak displacement: 0.225/0.325/0.425mm (4.5%/6.5%/8.5% of h) Ramp time: 1.84 ± 0.1s Hold time: 120s	$E_{\text{indentation}}=5.3\text{MPa}$
Young porcine [37]	3 rd , 4 th	 Disk	h=3	Nanoindentation testing (Spherical indenter diameter:100μm)	Peak displacement: 2.0 or 3.1 μm (6.7% or 10.3% of h) Ramp speed: 0.2μm/s or 2μm/s Hold time: 150s	$E_{\text{indentation}}=1-2.4\text{MPa}$ Total relaxation: 15.8%-32.1% (17.3% at 0.2μm·s ⁻¹ with in 30s hold time for an indentation depth 2.0 μm, 29.5% at 2μm·s ⁻¹ within 20s of the hold time for an indentation depth of 3.1μm)

As shown in Figure 4.2, the highest compressive stress of ~240kPa and the lowest compressive stress of ~60kPa of the porcine CC segments are experienced at the posterior surface of the 5th CC at location 1 and the anterior surface of the 9th CC at Location 3, respectively. This level of stress is well below the average stress of 1-1.5MPa experienced by AC during walking [54]. The physiological compressive loading on the exterior surface of CC is the pressure in the ribcage and is well below the body weight carried by AC. Thus, low compressive stress acting on the exterior surface of CC is expected. Taken together, low compressive properties at the exterior surface is sufficient for CC growth and assembly, but high compressive properties at the interior region are necessary for providing structural strength for the ribcage.

4.5.2. Comparison with the measured mechanical properties of CC in the literature

The peripheral region contains lower-level aggrecan but more interstitial fluid than the interior region. Upon low compressive loading, both interstitial fluid and ECM contribute to the viscosity. As compressive loading goes up, interstitial fluid flows out, only ECM contributes to the viscosity. This explains why the normalized relaxation drops at low indentation depth and becomes stabilized at high indentation depth. Shikha Gupta et al.'s study [37] conducted stress relaxation measurements of 3mm-thick CC disks from porcine 3rd and 4th ribs with one single step depth. In their study, the normalized relaxation is 17.3% at $0.2\mu\text{m}\cdot\text{s}^{-1}$ within 30s of the hold time of an indentation depth of $2.0\mu\text{m}$; and the normalized relaxation is 29.5% at $22\mu\text{m}\cdot\text{s}^{-1}$ within 20s of the hold time for an indentation depth of $3.1\mu\text{m}$. A high loading rate translates to a higher normalized relaxation. Under the same loading rate, a low indentation depth gives rise to a low normalized relaxation. Our measured normalized relaxation is about 25%~40% for porcine 5th ~ 12th CC segments. Since the testing parameters used in this study are quite different from the

above-mentioned study, a quantitative comparison in viscosity cannot be made between the exterior surface and the transverse cross-section of porcine CC.

4.5.3. Variation in measured mechanical properties among the CC segments

The elasticity of human CC was found to show a decreasing trend along the cartilage length from the costochondral joint to the chondrosternal joint [4]. A CC segment can be treated as a flexural beam, with its costochondral joint being fixed and its chondrosternal joint being guided by the sternum. During thoracic expansion, a CC segment experiences high tensile stress but small deformation toward the costochondral joint, but a low tensile stress but large deformation toward the chondrosternal joint. Thus, the decreasing trend of the elasticity of CC along the cartilage length accommodates respiration. Our measured elasticity of porcine CC along the cartilage length at their exterior surface does not capture this trend. CC segments are connected to different muscle groups, and different portions of a CC segment along the length are exposed to different organs [55]. The connecting muscles and organs along the cartilage length expose the CC to different compressive loading. Then, the compressive loading on the exterior surface fluctuates along the cartilage length, which explains the relatively random variation of measured elasticity at the exterior surface along the cartilage length.

Overall, our results demonstrate that the posterior surface is stiffer than the anterior surface in porcine CC, possibly because gravitational forces of the internal organs acting on the posterior surface in quadrupeds. The 9th CC is the softest and the 8th CC is the most viscous among the measured CC segments. This is likely because the 8th CC and 9th CC are at the chest-abdomen transition. As the true ribs, the 5th ~7th CC segments are overall stiffer than the false ribs, 8th~10th segments, and the floating ribs, 11th and 12th segments. The false ribs and the floating ribs have similar elasticity. The anterior and posterior surfaces of the true ribs are

connected to the pectoralis major and the transversus thoracic muscles, respectively. In contrast, the anterior surface of the false and floating ribs is connected to the flat muscles of the anterior abdominal wall, while their posterior surface is connected to the transversus abdominis and the diaphragm muscles. Such difference among connecting muscles may explain the variation in measured elasticity between the true ribs and the false and floating ribs. Furthermore, a study on the ribs of four cadavers [56] found that the mechanical strength varies along the length of the ribs and the mechanical strength of the ribs increases from 2nd to 6th and then decreases from 7th to 12th. The changing trend in the ribs is similar to the changing trend in the measured elasticity of the porcine CC segments.

To the best knowledge of the authors, this study is the first of its kind systematic study on mechanical properties across different porcine CC segments from the same pig. The observed relative difference in measured mechanical properties among different anatomical sites of porcine CC is believed to carry physiological implications. The obtained values will vary with the testing parameters used in the testing protocol, but are not expected to alter the observations on measured mechanical properties of porcine CC of this study. Finally, the authors acknowledge that conclusions based on the porcine CC segments from one pig cannot be generalized, as individual variability is highly expected and the absolute values are likely to vary among a large pool of samples.

4.6. Conclusions

Taken together, in this chapter, a conformal indentation was conducted was to determine the mechanical properties at the exterior surface of porcine CC and examine how they vary with the anatomical sites of porcine CC in the ribcage. Via a tactile sensor with a 5mm×0.5mm×3mm built-in probe, a total of 56 conformal indentation measurements were

conducted at the anterior and posterior surfaces of whole porcine 5th -12th CC segments along the cartilage length to record their time-dependent response to a multi-step indentation-relaxation testing protocol. The instant indentation modulus and normalized relaxation of the CC segments were derived from the recorded data to quantify their elasticity and viscosity, respectively.

Overall, the measured mechanical properties of porcine CC vary with their anatomical sites and thus indicate the adaptation of porcine CC to their local biomechanical environment in the ribcage. The instant indentation modulus at the CC exterior surface is in the range of 130kPa~500kPa, well below that at the CC transverse cross-section which arises from higher levels of aggrecan in the interior region over the peripheral region. The normalized relaxation at the CC exterior surface is relatively high at low applied stress, but becomes constant at high applied stress. The constant normalized relaxation at the CC exterior surface is in the range of 25%~40%. The 5th CC is the stiffest and the least viscous among the 5th ~12th segments. As true ribs, the 5th ~7th CC are stiffer than the 8th ~12th CC, the false and floating ribs. However, the false ribs and the floating ribs have similar elasticity. The 8th CC and the 9th CC are the softest and the most viscous, respectively, likely because they are located at the chest-abdomen transition. Overall, the posterior surface is stiffer than the anterior surface, possibly due to gravitational forces acting on porcine CC. Meanwhile, the measured elasticity and viscosity do not show any trend along the cartilage length. The variation in measured mechanical properties of among different anatomical sites of porcine CC indicates their adaptation to the local biomechanical environments in the ribcage.

CHAPTER 5

MEASURED MECHANICAL PROPERTIES OF HUMAN PECTUS CARINATUM COSTAL CARTILAGE

This purpose of this chapter is to measure the mechanical properties at the exterior surface of human PC CC, and determine whether the mechanical properties show a link with the anatomic sites and the cartilage length. This study is also carried out via the same tactile sensor with a built-in probe. The tactile sensors used in this chapter are sensor B and C with identical design. Their equilibrium stiffness with a built-in probe is $960\text{N}\cdot\text{m}^{-1}$ and $720\text{N}\cdot\text{m}^{-1}$, respectively. The experimental setup, pre-defined parameters, and data analysis are the exact same as the ones used in Chapter 4 and will not be further demonstrated in this chapter. The sample preparation, results, and discussions are elaborated in detail.

5.1. Sample Preparation

Five human CC segments were harvested from ribs of the lower thoracic region (7th~10th ribs) of a 15yr-old male patient at Children's Hospital of The King's Daughters (CHKD), Norfolk, VA. The 7th~10th rib cartilages were chosen because those cartilages were usually removed for PC patients during the clinical surgery. The segments were obtained and treated in accordance with all testing and handling procedures approved by the Eastern Virginia Medical School (EVMS) Institutional Review Board (IRB). The CC segments were tested at room temperature right after they were removed in surgery. Note that intercostal muscles, fat and perichondrium were removed from their surface, leaving only the cartilage tissue. The cartilage segments were stored in PBS throughout the sample preparation at room temperature and kept moist throughout the measurement via PBS spray. As shown in Figure 5.1, measurements on a CC segment were conducted on the positions of 6mm apart along its length, with the four locations: the anterior/posterior surfaces and superior/inferior borders being measured at each position.

Table 5.1 summarizes the whole length and the cross-section of the five CC segments. As mentioned in Section 4.1, the cross-section of each measured position is quantified as the width (superior to inferior) and the depth (anterior to posterior). The average width and the average depth are the average from all the measured positions of a CC segment. The width/depth ratio for CC# B-E decreases from rib to sternum along its exterior surface length. As to CC# A, from rib to sternum along its exterior surface length, the width/depth ratio decreases first and slightly increase. In most cases, the CC width is larger than the CC depth.

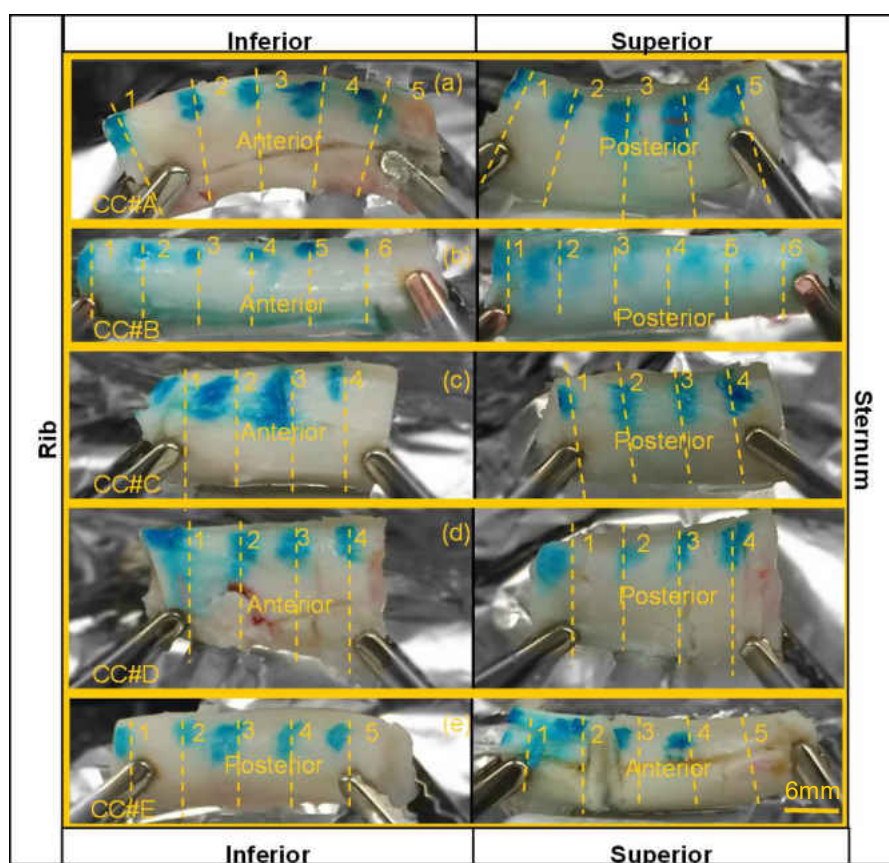


Figure 5.1 Pictures and schematics of human PC costal cartilage segments and the locations for measurement (a) CC #A (b) CC #B (c) CC #C (d) CC #D (e) CC #E.

Table 5.1 Key dimensions of tested human PC costal cartilage segments.

CC segment #	Length (mm)	Width (mm)	Depth (mm)	Width/Depth ratio (%)					
				Whole CC segment	1*	2*	3*	4*	5*
A	33.2	12.0±2.0	6.7±1.3	64.0%	50.0%	55.8%	54.5%	57.1%	--
B	40.1	12.4±1.1	9.6±0.4	86.4%	81.7%	79.2%	76.9%	74.1%	69.2%
C	24.6	13.0±1.0	10.0±1.0	91.7%	80.0%	74.1%	64.3%	--	--
D	24.3	13.4±2.6	7.6±0.4	68.2%	60.0%	53.6%	50.0%	--	--
E	34.8	9.7±0.3	8.5±0.5	94.7%	85.0%	94.4%	85.0%	80.0%	--

1*-6* - Means Location 1- Location 6 and Indicates that the measured location along the coastal cartilage length.

5.2. Results

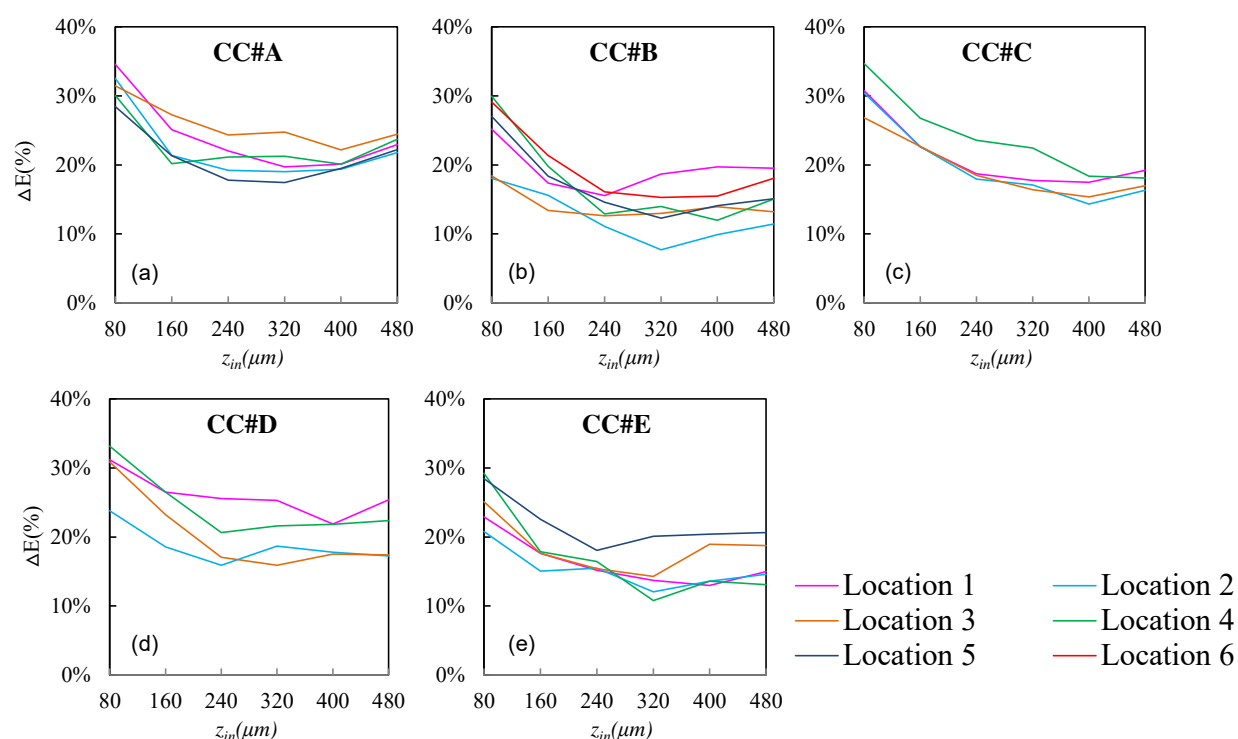


Figure 5.2 Measured normalized relaxation as a function of indentation depth of CC segment (a) CC#A (b) CC#B (c) CC#C (d) CC#D (e) CC#E. (The color coded numbers indicate the measured locations)

As listed in Figure 5.1, CC #E is the roundest and has the smallest cross section; CC #A and #D are the flattest; and CC #B and #C are just in between. Figure 5.2 illustrates how the average normalized relaxation from the four anatomical sites at the same location varies with the indentation depth at the measured locations for the five CC segments. Overall, the average normalized relaxation shows a mild decreasing trend with the indentation depth in the indentation range of 80~240 μ m and then becomes stabilized in the indentation range of

240~480 μ m. Thus, the normalized relaxation is calculated as the average from the indentation range of 240~480 μ m.

5.2.1. Instant indentation modulus shows a link with anatomical sites

Figure 5.3(a) shows how the measured instant indentation modulus at the four anatomical sites and their average value from the four sites at the same location vary along the length of each CC segment. In CC #A, the instant indentation modulus fluctuates slightly at the anterior and posterior surfaces, but swings drastically at the superior and inferior borders. In CC #E, the instant indentation modulus at the anterior surface and inferior borders swing dramatically. Owing to a cross cut from the surgery at location 2, the instant indentation modulus at its inferior border is missing. In CC #B, #C, and #E, the instant indentation modulus swings a lot only at one anatomical site. Overall, the instant indentation modulus at each anatomical site varies randomly along the cartilage length, but interestingly the average instant indentation modulus at the measured locations does not vary much along the cartilage length for all the CC segments. This might indicate that the rest of the anatomical sites at the same location adjust themselves to accommodate any change in one anatomical site.

Figure 5.4 (a) shows how the average instant indentation modulus of each anatomical site along the length of each CC segment varies among the four anatomical sites and their average value varies among the CC segments. Overall, the variation in average instant indentation modulus among the four anatomical sites is significant in all the CC segments. However, the instant indentation modulus at the anterior surface is always higher than that at the posterior surface. Meanwhile the instant indentation modulus at the superior border shows an exact opposite trend as compared with the instant indentation modulus at the anterior/posterior surfaces. The instant indentation modulus at the inferior border fluctuates randomly.

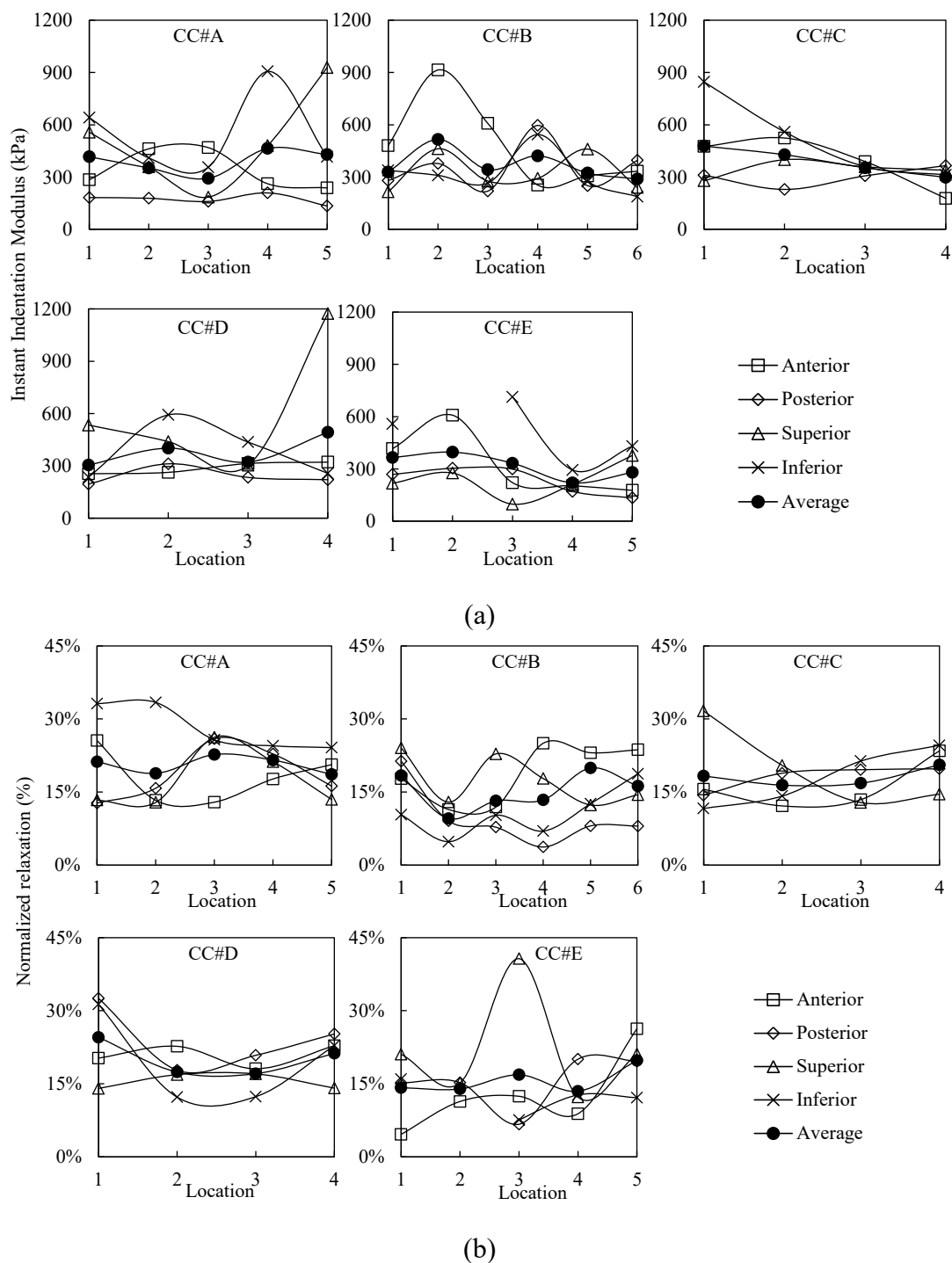


Figure 5.3 Measured mechanical properties along the length (from rib to sternum) of CC at its anterior/posterior surfaces, superior/inferior borders and the average of the four positions (a) instant indentation modulus of CC#A-E (b) normalized relaxation of CC#A-E. (A: Anterior; P: Posterior; S: Superior; I: Inferior; Average: Average values of four surfaces)

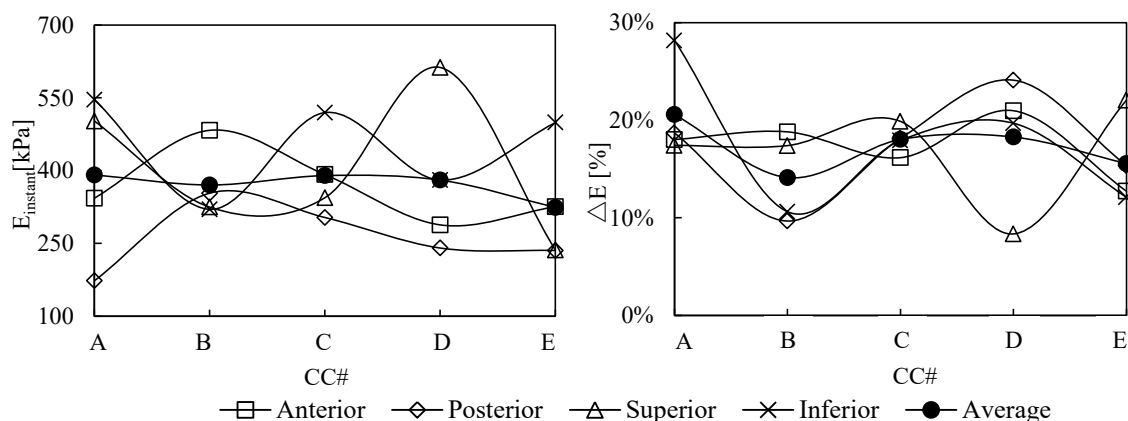


Figure 5.4 Measured average viscoelastic properties of the CC segments at their anterior/posterior surfaces, superior/inferior borders and the average of the four positions (a) average instant indentation modulus (b) average normalized relaxation. (A: Anterior; P: Posterior; S: Superior; I: Inferior; Average: Average values of four surfaces)

Table 5.2(a) summarizes the values of the average instant indentation modulus at the four anatomical sites and their average values of the five CC segments. Overall, the average instant indentation modulus reveals random variations with the four anatomical sites among the CC segments. Interestingly, the average instant indentation modulus from the four anatomical sites is similar among the CC segments, except CC #E being much softer than the rest of the segments.

Table 5.2 Summary of the average instant indentation modulus and average normalized relaxation and their deviation (a) among the atomically sites and (b) along the cartilage length of the CC segments at their exterior surface.

(a)

Parameters	CC#	Anterior	Posterior	Superior	Inferior	Average
$E_{instant}$ (kPa)	A	343.1	172.9	502.0	546.1	391.0
	B	482.9	353.3	324.6	320.1	370.2
	C	391.7	303.2	344.0	519.5	389.6
	D	288.0	240.3	612.4	380.4	380.3
	E	325.5	235.3	236.4	498.9	324.0
ΔE (%)	A	18.0%	18.7%	17.4%	28.2%	20.6%
	B	18.8%	9.7%	17.4%	10.6%	14.1%
	C	16.2%	18.1%	19.9%	17.9%	18.0%
	D	21.0%	24.1%	15.5%	19.7%	20.1%
	E	12.7%	15.4%	22.1%	12.1%	15.6%

(b)

Parameters	CC#	1	2	3	4	5	6	Average
$E_{instant}$ (kPa)	A	416.3	352.4	292.6	464.3	429.5	--	391.0
	B	328.7	516.1	342.6	421.8	323.0	289.2	370.2
	C	477.9	428.2	353.5	298.8	--	--	389.6
	D	304.9	401.6	321.6	493.1	--	--	380.3
	E	365.3	396.3	332.9	220.1	279.8	--	318.9
ΔE (%)	A	21.2	18.8	5.7	21.5	18.6	--	20.6
	B	18.4	9.6	13.2	13.4	14.0	16.2	15.1
	C	18.3	16.4	16.8	20.6	--	--	18.0
	D	24.5	17.4	17.1	21.2	--	--	20.1
	E	14.2	13.9	16.8	13.5	19.8	--	15.6

Table 5.2(b) summarizes the values of the average instant indentation modulus at all the measured locations for the five CC segments. The instant indentation modulus varies randomly along the cartilage length for all the CC segments, except CC #C revealing a decreasing trend along the cartilage length.

5.2.2. Normalized relaxation varies randomly with anatomical locations

Figure 5.3(b) shows how the normalized relaxation at the four anatomical sites and their average from the four anatomical sites varies along the cartilage length in the five PC CC segments. Similar to the instant indentation modulus, the normalized relaxation varies randomly among the four anatomical sites, and swings drastically at least at one anatomical site. Interestingly, the average normalized relaxation from the four anatomical sites does not fluctuate much in all the CC segments, except CC #B and #E, indicating that compensation might exist among the four anatomical sites at the same location. Figure 5.4(b) shows how the average normalized relaxation of each anatomical site varies among the four anatomical sites and among the CC segments. Similar to instant indentation modulus, the normalized relaxation varies randomly among the four anatomical sites and also among the CC segments. Interestingly, CC#B and #E shows a relatively lower value of normalized relaxation as well.

Table 5.2 (a) summarizes the normalized relaxation averaged over the cartilage length at the four anatomical sites for the five CC segments. The normalized relaxation varies randomly among the four anatomical sites. Overall, CC #A, #C and #D exhibit similar viscosity, and CC #B and #E reveal a lower viscosity. Table 5.2 (b) summarizes the average normalized relaxation at all the measured locations for the five segments. The normalized relaxation does not show any trend along the cartilage length for all the segments. Finally, it must be emphasized that there is no correlation between the instant indentation modulus and the normalized relaxation.

Table 5.3 (a) quantitatively compares the variation in instant indentation modulus and normalized relaxation modulus among the four anatomical sites. There is a significant variation in instant indentation modulus among the four sites in CC #A, #D and #E, and a significant variation in normalized relaxation among the four sites in CC #B and #E. Note that CC #B and #E exhibit low viscosity, but suffer higher viscosity variation across the transverse section. Since the significant variation in elasticity and viscosity vary among the CC segments, we might conclude that the structure in charge of elasticity is different from the structure in charge of viscosity. Table 5.3 (b) quantitatively compares the variation in instant indentation modulus and normalized relaxation modulus along the cartilage length. There is a significant variation in instant indentation modulus along the cartilage length in CC #B and #E, but this variation is much lower than that among the four sites. There is a significant variation in the normalized relaxation along the cartilage length in CC #A and #B, and this variation is comparable to that among the four sites. Interestingly, CC #A and CC #B are the segments with the highest viscosity and the lowest viscosity, respectively. This observation validates the above conclusion that the structure in charge of elasticity is different from the structure in charge of viscosity.

Taken together, CC #A demonstrates the highest stiffness variation among the four sites and the highest viscosity variation along the cartilage length. Finally, CC #C is the only CC segment showing no significant variation in elasticity and viscosity among the four sites and along the cartilage length. Meanwhile, only CC #C shows a trend of elasticity along the cartilage length.

Table 5.3 Comparison (a) among the atomically sites and (b) along the cartilage length of the CC segments at their exterior surface

(a)

Parameters	A	B	C	D	E
stiffness variation	373.2	162.8	216.3	372.1	263.6
absolute stiffness	391.0	370.2	389.6	380.3	324.0
stiffness variation%	10.80%	9.10%	1.90%	8.60%	10.00%
viscosity variation	20.6%	14.1%	18.0%	20.1%	15.6%
absolute viscosity	95.4%	44.0%	55.5%	97.8%	81.4%
viscosity variation%	52.4%	64.5%	10.6%	42.8%	64.1%

(b)

Parameters	A	B	C	D	E
stiffness variation	171.7	226.9	179.1	188.2	176.2
absolute stiffness	391.0	370.2	389.6	380.3	318.9
stiffness variation%	15.8%	8.8%	4.2%	7.4%	6.3%
viscosity variation	20.6%	14.1%	18.0%	20.1%	15.6%
absolute viscosity	43.9%	61.3%	46.0%	49.5%	55.3%
viscosity variation%	76.7%	62.4%	23.3%	36.8%	40.4%

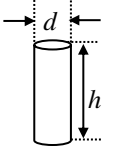
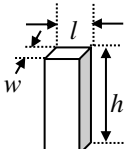
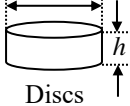
5.3. Discussion

Table 5.4 summarizes the measured values on the mechanical properties of human healthy CC and PE CC in the literature. Evidently, the measured values vary with the testing parameters and instrument used, other than the ribs and the age of the human subjects. Nevertheless, the measured indentation modulus is well above 1MPa. The instant indentation modulus we measured here is well below 1MPa. Although the testing parameters, instruments, and samples may play a role, the main cause of this difference is believed to be the structural difference between the interior region and the peripheral region. As mentioned earlier, the

interior region has a high level of aggrecan, which is negatively charged and carries a high osmotic pressure. As such, a high compressive strength is expected from the interior region. The indentation measurements on CC disks and the compression measurements on CC strips are focused just on the interior region. In this work, the indentation measurement was conducted at the exterior surface, which has a low level of aggrecan and thus carries a low osmotic pressure. Then, the exterior surface exhibits a low compressive strength. Additionally, the literature mentioned that the biomechanical stability of PE CC is weaker than those of healthy CC, which also provide another cause of the relatively smaller indentation modulus we obtained.

In the low indentation range, the normalized relaxation shows a decreasing trend with the indentation depth, indicating that the viscosity decreases with the prestress. This is reasonable in the sense that, due to prestress, the interstitial fluid in the peripheral region can easily flow out of the exterior surface, and thus the viscosity drops. As the indentation depth increases, the structure underneath the peripheral region starts to affect the viscosity of the peripheral region and then the viscosity becomes stabilized. The measured compressive stress is below 0.4MPa, which is well below the average stress of 1-1.5MPa in the knees during walking. The physiological compressive loading acting on the exterior surface is the pressure in the thoracic cage and is much smaller than the body weight carried by the knees. Then, low compressive stress acting on the exterior surface of CC is expected.

Table 5.4 Measured mechanical properties of human CC reported in the literature.

CC	Age (Years)	Sample location	Sample shape	Sample dimension (mm)	Testing techniques	Controlled parameters	Measured Mechanical Properties (MPa)
PE	C:3-6 [17]	6 th	 Cylinder stripe	h=30 d=8	Tensile	--	Strength: 1.5±0.4
					Compression	--	Strength: 1.3±0.2
					Flexural	--	Strength: 4.1±1.2
					Tensile	--	Strength: 2.3±0.2
					Compression	--	Strength: 8.3±1.0
					Flexural	--	Strength: 7.6±1.9
Healthy	A:37-86 [22]	6 th -9 th	 Cuboid stripe	h=6 d=6	Compression	--	Modulus: 103.4±30.1 Strength: 7.6±1.8
				h=50 l=10 w=7	Three-point bending flexural	--	Modulus: 8.8±2.9 Strength:
	C:5-10; Ad:11-17; A:18-25 [3]	--	Cuboid stripe	h=10-15 l=1.5-2 w=1.5-2	Tensile	--	5.8±2.1
	A:37-86 [22]	6 th -9 th		--	Mirco-hardness	--	38-62
	A:23-77 [1]	2 nd ,3 rd , 4 th ,6 th	 Discs	h=6	Indentation D=3.15mm	$z_{in_max}=0.425\text{mm}$ (7% of h) $t_{ramp}=2.125\text{s}$ $t_{hold}=2\text{min}$	5.2
	A:47,49,53,54,57 [27]	4 th		h=7	Indentation D= 2mm	$z_{in_max}= 0.25\text{mm}$ (4% of h) Ramp speed:0.5mm·s ⁻¹	11.0/10.5/ 12.6/9.5/ 8.7
	A:32,71 [29]	5 th		h=5	Indentation D=3.15mm	$z_{in_max}=0.5\text{mm}$ $t_{ramp}=2.1\text{s}$, $t_{hold}=2\text{min}$	10
	A:54,62,31 [4]	3 rd		h=7-10	Nanoindentation D=1/5/10μm	$z_{in_max}< 10\%$ of h $t_{ramp}=10\text{s}, 25\text{s}$, $t_{hold}=100-125\text{s}$	2.2±1.3 4.1±1.9 5.5±2.4

C- Child; Ad-Adolescent; A-Adult; D-diameter of spherical indenter; z_{in_max} -Peak displacement; t_{ramp} -Ramp time; t_{hold} -Hold time;

In Chapter 4, there is no dependence between the measured properties with the transverse cross-section geometries and curved shapes of the CC segments. As compared with the values in

Table 5.1 and Table 5.3, the same conclusion can be made. The compressive loading at the exterior surface helps to press oxygen and nutrients in the perichondrium into the peripheral region. Along the cartilage length, CC take the large tubular structures (from straw-like structures) running through the cartilage length and thus can bear the tensile loading from the thoracic expansion. When it is stretched along the cartilage length, the gap among the straw-like structures is reduced and then, oxygen and nutrients can get diffused deep into the straw-like structures in the interior region. Furthermore, the straw-like structures also help to diffuse oxygen and nutrients along the cartilage length. Therefore, no abrupt structural change can be expected along the cartilage length. This will be confirmed in future studies along with proteomic analysis to determine any changes in protein composition that may account for observed differences measured in this paper. Of particular interest will be the small leucine rich proteoglycans that act to ‘zipper’ the collagen strands together. Abnormal ‘zippers’ may account for differential structural integrity resulting in different force measurements.

5.4. Conclusions

The results of this chapter provide novel data for the mechanical properties at the exterior surface of human PC CC. The data shows that the mechanical properties vary significantly among the four anatomical sites at the same location. This study reveals significant variation in mechanical properties by PC. Five CC segments from the 7th ~10th ribs are obtained from a 15yr-old PC patient. Using a tactile sensor via a testing protocol of multiple indentation-relaxation steps, four anatomical sites: anterior/posterior surfaces and superior/inferior borders are measured at locations of 6mm apart along the length of each CC segment. The instant indentation modulus and normalized relaxation are derived from the recorded mechanical response to quantify the elasticity and viscosity at each measured site of the CC segments,

respectively. The instant indentation modulus and normalized relaxation at the PC CC exterior surface are respectively in the range of 98kPa~1173kPa and 5%~25%, well below that at the CC transverse cross-section. These human PC CC samples are found to be stiffer and less viscous than healthy porcine CC. The normalized relaxation reveals a decreasing trend with the indentation depth in the range of 80 μ m~240 μ m, but becomes stabilized in the indentation range of 240 μ m~480 μ m for all the CC segments. Overall, the anterior surface is stiffer than the posterior surface, which is opposite to porcine CC and is possibly due to different gravitational forces acting on them. For all the CC segments, the instant indentation modulus and normalized relaxation both reveal a large, random variation among the four anatomical sites at the same location. However, the average instant indentation modulus and average normalized relaxation from the four sites at the same location both do not change much along the cartilage length, indicating that the rest of the anatomical sites might adjust to accommodate the change at one anatomical site. Only the segment #C shows a decreasing trend of instant indentation modulus along the cartilage length and exhibits mild variation in elasticity and viscosity among the four sites and along the cartilage length.

CHAPTER 6

CONCLUSIONS AND RECOMMENDATIONS

In this chapter, the highlights and conclusive remarks of this dissertation are presented, and recommendations for the future work are proposed based on the current achievement.

6.1. Major Findings and Important Conclusions

This dissertation investigated the mechanical properties of CC at their exterior surface via conformal indentation testing which is built upon a tactile sensor with a built-in probe for distributed-deflection detection. The specific aims were (i) to design a tactile sensor with a built-in probe for measuring the mechanical properties of CC at their curved surface, (ii) to determine the mechanical properties at the exterior surface of porcine CC and examine how they vary with the anatomical sites of CC in the ribcage, and (iii) to measure mechanical properties of different anatomical sites at the exterior surface of human PC CC, and determine whether the mechanical properties vary with the anatomic sites and along the cartilage length. Three separate sets of studies were performed to accomplish the specific aims, including (i) a set of sensor performance studies, (ii) an experimental study on porcine CC, and (iii) an experimental study on human PC CC. From these studies, we have validated the feasibility of a tactile sensor with a built-in probe for mechanical measurements of CC at their curved exterior surface and determined mechanical properties of porcine CC and human PC CC, including the instant indentation modulus and the normalized relaxation. Both mechanical properties will serve as important parameters for learning the structure-function relation of the CC tissues and analyzing the pathology of PC.

6.1.1. A Set of Sensor Performance Studies

First of all, before adding a built-in probe to the sensor design, we performed two sets of experimental studies on the sensor performance, including sensor characterization study via a rigid probe and sensor performance study via a CC measurement. According to the test results, the sensor is able to detect distributed normal loads and has the robust feature. However, it fails to capture the mechanical behavior of CC with a curved exterior surface and suffers from probe misalignment issues. As such, a series of studies, including qualitative analysis, numerical simulation and experimental study, are performed on the tactile sensor with a built-in probe to find out a solution for capturing the inherent mechanical properties of CC with curved exterior surface and reduce the effect of probe misalignment.

In qualitative analysis, a simple one dimension theoretical model is established to derive the tissue stiffness from the known key parameters of the sensor and probe. As a result, the relation between the probe, sensor, and tissue is clearer. In summary, The sensor stiffness, k_s , must be lower than the tissue stiffness, k_t ($k_s < k_t$), so that the maximum sensor deflection, z_{s_max} , can be tailored to be a little lower than its adjusted maximum linear deflection range, $z_{s_linear} - \delta_s$, for keeping the collected data to cover the full linear deflection range of the sensor. The probe height, h_p , is a tradeoff between accommodation of the highest thickness, δ_t , on a curved tissue surface and avoidance of buckling ($\delta_p < h_p < h_{p_buckling}$). As to CC tissues with their elasticity range of 1MPa-7MPa, the highest tissue stiffness is seven times the lowest tissue stiffness. The sensor stiffness targeted for the CC in the higher elasticity end will cause the collected data on the CC in the lower elasticity end to be located in the lower linear deflection range of the sensor, which translates a larger amount of experimental errors. However, the sensor and probe stiffness in the lower end will fail to capture the mechanical properties of CC with its elasticity in the

higher end.

Then a numerical simulation is established to provide a feasible method to examine the effects of CC parameters on the simulated CC elasticity (equivalent to the measured CC elasticity in the measurement) via this tactile sensor of a built-in probe. The FEM analysis results show that the effects of CC parameters on the measured CC elasticity are more significant for the CC with a small diameter and a low pre-set CC elasticity. Thus, the numerical results suggest that the indentation-relaxation testing is more reliable in measuring CC with larger CC diameter and pre-set CC elasticity. The FEM analysis results also reveal the relative linear relationship between the CC diameter and the compensation coefficient, which is used for improving the measured indentation modulus in the experimental measurement. Please note that this compensation coefficient is only suitable for this tactile sensor with a 0.5mm×5mm×3mm built-in probe.

Finally, a proof-of-concept experimental study is carried out on two human PC CC samples. As compared with the measured results of the PC CC by the sensor without a built-in probe, the measurements on two human PC CC samples validate the feasibility of a tactile sensor with a built-in probe for conformal mechanical measurements of CC at its exterior surface. Based on the recorded relation of sensor deflection to indentation depth of the two samples measured using the sensor with a built-in probe, the CC instant indentation modulus and normalized relaxation of the two samples are derived and found to vary significantly among the anterior/posterior surfaces and superior/inferior borders at the same position of each sample.

6.1.2. Experimental Study on porcine CC

By using the tactile sensor with a built-in probe, an indentation-relaxation test was conducted at the anterior and posterior surfaces of whole porcine 5th -12th CC segments along the

cartilage length to record their time-dependent response to a multi-step indentation-relaxation testing protocol. The instant indentation modulus and normalized relaxation of the CC segments were derived from the recorded data to quantify their elasticity and viscosity, respectively. In sum, the measured mechanical properties of porcine CC vary with their anatomical sites and thus indicate the adaptation of porcine CC to their local biomechanical environment in the ribcage. The instant indentation modulus at the CC exterior surface is in the range of 130kPa~500kPa, well below that at the CC transverse cross-section which arises from higher levels of aggrecan in the interior region over the peripheral region. The normalized relaxation at the CC exterior surface is relatively high at low applied stress, but becomes constant at high applied stress. The constant normalized relaxation at the CC exterior surface is in the range of 25%~40%. The 5th CC is the stiffest and the least viscous among the 5th ~12th segments. As true ribs, the 5th ~7th CC are stiffer than the 8th ~12th CC, the false and floating ribs. However, the false ribs and the floating ribs have similar elasticity. The 8th CC and the 9th CC are the softest and the most viscous, respectively, likely because they are located at the chest-abdomen transition. The posterior surface is stiffer than the anterior surface, possibly due to gravitational forces acting on porcine CC. Meanwhile, the measured elasticity and viscosity do not show any trend along the cartilage length. The variation in measured mechanical properties of among different anatomical sites of porcine CC indicates their adaptation to the local biomechanical environments in the ribcage.

6.1.3. Experimental Study on Human PC CC

By using the tactile sensor with a built-in probe, we also performed the same indentation-relaxation test at the exterior surface of human PC CC for their mechanical properties. The results reveal significant variation in mechanical properties of PC CC. Five CC

segments from the 7th ~10th ribs are obtained from a 15yr-old PC patient. The instant indentation modulus and normalized relaxation are still derived from the recorded mechanical response to quantify the elasticity and viscosity at each measured site of the CC segments, respectively. The instant indentation modulus and normalized relaxation at the PC CC exterior surface are in the range of 98kPa~1173kPa and 5%~25%, respectively. The instant indentation modulus at the CC exterior surface is well below that at the CC transverse cross-section. These human PC CC samples are found to be stiffer and less viscous than healthy porcine CC. The normalized relaxation reveals a decreasing trend with the indentation depth in the range of 80 μ m~240 μ m, but becomes stabilized in the indentation range of 240 μ m~480 μ m for all the CC segments. Overall, the anterior surface is stiffer than the posterior surface, which is opposite to porcine CC and is possibly due to different gravitational forces acting on them. For all the CC segments, both the instant indentation modulus and normalized relaxation reveal a large, random variation among the four anatomical sites at the same location. However, the average instant indentation modulus and average normalized relaxation from the four sites at the same location both do not change much along the cartilage length, indicating that the rest of the anatomical sites might adjust to accommodate the change at one anatomical site. Only the segment #C shows a decreasing trend of instant indentation modulus along the cartilage length and exhibits mild variation in elasticity and viscosity among the four sites and along the cartilage length.

To the best knowledge of the author, this dissertation is the first of its kind systematic study on mechanical properties across different porcine CC segments from the same pig and different human PC CC samples from the one patient. The observed relative difference in measured mechanical properties among different anatomical sites of porcine and human CC is believed to carry physiological implications. The obtained values will vary with the testing

parameters used in the testing protocol, but are not expected to alter the observations on measured mechanical properties of porcine and human CC of this dissertation. Finally, the author acknowledged that conclusions based on the porcine CC segments from one pig and human PC CC samples from one patient cannot be generalized, as individual variability is highly expected and the absolute values are likely to vary among a large pool of samples.

6.2. Future Work

6.2.1. The Mechanical Properties of Costal Cartilage Transverse Cross-sections

The measured mechanical properties in this dissertation are from the exterior surface of CC, while the mechanical properties discussed in the literature are mainly from the CC cross-sections. Meanwhile, different testing methods will lead to the variation in the measured results. Thus, it is difficult to compare the measured mechanical properties at CC exterior surface via the tactile sensor in this dissertation with the measured mechanical properties at CC cross-section via micro/nano indentation tests in the literature. If the mechanical properties of CC cross-section can also be tested after the measurement on the CC exterior, a better comparison can be made among the mechanical properties measured at exterior surface and cross-section via a tactile sensor with a built-in probe and the mechanical properties discussed in the literature.

6.2.2. Numbers of Costal Cartilage Samples

Since the conclusions based on the porcine CC segments from one pig and human PC CC samples from one patient cannot be generalized, as individual variability is highly expected and the absolute values are likely to vary among a large pool of samples.

6.2.3. Biochemical study on Costal Cartilage

As discussed in Section 5.3, a biochemical study, such as proteomic analysis can be added to determine any changes in protein composition that may account for observed differences measured in this dissertation. Of particular interest will be the small leucine rich proteoglycans that act to ‘zipper’ the collagen strands together. Abnormal ‘zippers’ may account for differential structural integrity resulting in different force measurements and providing a better understanding of the CC structure-function relation.

6.2.4. Future applications of this sensor

This dissertation validates a new methodology to capture the mechanical properties of CC. This testing method can be used to measure the mechanical properties of other materials, including both viscoelastic and elastic material, such as biological soft tissues, polymers and plastics. Please note the material stiffness is required to be slightly higher than the sensor stiffness which can be adjusted by changing the sensor stiffness, such as probe height and probe elasticity.

REFERENCES

- [1] A. Lau, M. L. Oyen, R. W. Kent, D. Murakami, and T. Torigaki, "Indentation stiffness of aging human costal cartilage," *Acta biomaterialia*, vol. 4, pp. 97-103, 2008.
- [2] O. Rejtarová, P. Hejna, T. Soukup, and M. Kuchař, "Age and sexually dimorphic changes in costal cartilages. A preliminary microscopic study," *Forensic science international*, vol. 193, pp. 72-78, 2009.
- [3] B.-y. Guo, D.-h. Liao, X.-y. Li, Y.-j. Zeng, and Q.-h. Yang, "Age and gender related changes in biomechanical properties of healthy human costal cartilage," *Clinical Biomechanics*, vol. 22, pp. 292-297, 2007.
- [4] S. Tripathy and E. Berger, "Quasi-linear viscoelastic properties of costal cartilage using atomic force microscopy," *Computer methods in biomechanics and biomedical engineering*, vol. 15, pp. 475-486, 2012.
- [5] L. Nimeskern, M. M. Pleumeekers, D. J. Pawson, W. L. Koevoet, I. Lehtoviita, M. B. Soyka, *et al.*, "Mechanical and biochemical mapping of human auricular cartilage for reliable assessment of tissue-engineered constructs," *Journal of biomechanics*, vol. 48, pp. 1721-1729, 2015.
- [6] V. C. Mow, S. Kuei, W. M. Lai, and C. G. Armstrong, "Biphasic creep and stress relaxation of articular cartilage in compression: theory and experiments," *Journal of biomechanical engineering*, vol. 102, pp. 73-84, 1980.
- [7] L. Han, E. H. Frank, J. J. Greene, H.-Y. Lee, H.-H. K. Hung, A. J. Grodzinsky, *et al.*, "Time-dependent nanomechanics of cartilage," *Biophysical journal*, vol. 100, pp. 1846-1854, 2011.
- [8] P. O'Connor, C. Orford, and D. L. Gardner, "Differential response to compressive loads of zones of canine hyaline articular cartilage: micromechanical, light and electron microscopic studies," *Annals of the rheumatic diseases*, vol. 47, pp. 414-420, 1988.
- [9] T. Aigner, S. Söder, P. M. Gebhard, A. McAlinden, and J. Haag, "Mechanisms of disease: role of chondrocytes in the pathogenesis of osteoarthritis—structure, chaos and senescence," *Nature Clinical Practice Rheumatology*, vol. 3, pp. 391-399, 2007.
- [10] M. R. Buckley, L. J. Bonassar, and I. Cohen, "Localization of viscous behavior and shear energy dissipation in articular cartilage under dynamic shear loading," *Journal of biomechanical engineering*, vol. 135, p. 031002, 2013.
- [11] B. Lee, L. Han, E. H. Frank, S. Chubinskaya, C. Ortiz, and A. J. Grodzinsky, "Dynamic mechanical properties of the tissue-engineered matrix associated with individual chondrocytes," *Journal of biomechanics*, vol. 43, pp. 469-476, 2010.
- [12] (2017, November 27). *FETAL PIG A STUDY PIG ANATOMY QUIZ*. Available: <http://paydayloans-mo.com/pig-anatomy-quiz/fetal-pig-a-study-pig-anatomy-quiz/>
- [13] A. Medicine. (2017, November 27). *The costal cartilage*. Available: <http://anatomy-medicine.com/musculoskeletal-system/63-the-costal-cartilage.html>
- [14] M. d. S. Coelho and P. d. S. F. Guimarães, "Pectus carinatum," *Jornal Brasileiro de Pneumologia*, vol. 33, pp. 463-474, 2007.
- [15] F. Tocchioni, M. Ghionzoli, L. Calosi, D. Guasti, P. Romagnoli, and A. Messineo, "Rib Cartilage Characterization in Patients Affected by Pectus Excavatum," *The Anatomical Record*, vol. 296, pp. 1813-1820, 2013.
- [16] Y. Wang, G. Chen, L. Xie, J. Tang, X. Ben, D. Zhang, *et al.*, "Mechanical factors play an important role in pectus excavatum with thoracic scoliosis," 2012.

- [17] J. Feng, T. Hu, W. Liu, S. Zhang, Y. Tang, R. Chen, *et al.*, "The biomechanical, morphologic, and histochemical properties of the costal cartilages in children with pectus excavatum," *Journal of pediatric surgery*, vol. 36, pp. 1770-1776, 2001.
- [18] R. H. Sweet, "Pectus excavatum: Report of two cases successfully operated upon," *Annals of surgery*, vol. 119, p. 922, 1944.
- [19] C. Brochhausen, S. Turial, F. K. Müller, V. H. Schmitt, W. Coerd, J.-M. Wihlm, *et al.*, "Pectus excavatum: history, hypotheses and treatment options," *Interactive cardiovascular and thoracic surgery*, vol. 14, pp. 801-806, 2012.
- [20] A. Hebra. (2016, November 27). *Nuss Procedure for Pectus Excavatum Technique*. Available: <https://emedicine.medscape.com/article/1970203-technique>
- [21] A. Chen, W. Bae, R. Schinagl, and R. Sah, "Depth-and strain-dependent mechanical and electromechanical properties of full-thickness bovine articular cartilage in confined compression," *Journal of biomechanics*, vol. 34, pp. 1-12, 2001.
- [22] W. Grellmann, A. Berghaus, E. J. Haberland, Y. Jamali, K. Holweg, K. Reincke, *et al.*, "Determination of strength and deformation behavior of human cartilage for the definition of significant parameters," *Journal of Biomedical Materials Research Part A*, vol. 78, pp. 168-174, 2006.
- [23] H. Sadeghi, D. Espino, and D. Shepherd, "Fatigue strength of bovine articular cartilage-on-bone under three-point bending: the effect of loading frequency," *BMC musculoskeletal disorders*, vol. 18, p. 142, 2017.
- [24] M. M. Kaiser, G. Zachert, R. Wendlandt, M. Rapp, R. Eggert, C. Stratmann, *et al.*, "Biomechanical analysis of a synthetic femoral spiral fracture model: Do end caps improve retrograde flexible intramedullary nail fixation?," *Journal of orthopaedic surgery and research*, vol. 6, p. 46, 2011.
- [25] R. Roy, S. S. Kohles, V. Zaporojan, G. M. Peretti, M. A. Randolph, J. Xu, *et al.*, "Analysis of bending behavior of native and engineered auricular and costal cartilage," *Journal of Biomedical Materials Research Part A*, vol. 68, pp. 597-602, 2004.
- [26] A. C. Chen, S. M. Klisch, W. C. Bae, M. M. Temple, K. B. McGowan, K. R. Gratz, *et al.*, "Mechanical characterization of native and tissue-engineered cartilage," *Cartilage and Osteoarthritis: Volume 2: Structure and In Vivo Analysis*, pp. 157-190, 2004.
- [27] J. L. Forman and R. W. Kent, "Modeling costal cartilage using local material properties with consideration for gross heterogeneities," *Journal of biomechanics*, vol. 44, pp. 910-916, 2011.
- [28] J. M. Mattice, A. G. Lau, M. L. Oyen, and R. W. Kent, "Spherical indentation load-relaxation of soft biological tissues," *Journal of Materials Research*, vol. 21, pp. 2003-2010, 2006.
- [29] M. Oyen, D. Murakami, and R. Kent, "Mechanical characterization of costal cartilage," in *33rd Proceedings, International Workshop on Human Subjects for Biomechanical Research*, 2005.
- [30] D. M. Ebenstein and L. A. Pruitt, "Nanoindentation of biological materials," *Nano Today*, vol. 1, pp. 26-33, 2006.
- [31] M. A. McLeod, R. E. Wilusz, and F. Guilak, "Depth-dependent anisotropy of the micromechanical properties of the extracellular and pericellular matrices of articular cartilage evaluated via atomic force microscopy," *Journal of biomechanics*, vol. 46, pp. 586-592, 2013.

- [32] W. C. Oliver and G. M. Pharr, "An improved technique for determining hardness and elastic modulus using load and displacement sensing indentation experiments," *Journal of materials research*, vol. 7, pp. 1564-1583, 1992.
- [33] M. Stolz, R. Raiteri, A. Daniels, M. R. VanLandingham, W. Baschong, and U. Aebi, "Dynamic elastic modulus of porcine articular cartilage determined at two different levels of tissue organization by indentation-type atomic force microscopy," *Biophysical journal*, vol. 86, pp. 3269-3283, 2004.
- [34] S. Park, K. D. Costa, and G. A. Ateshian, "Microscale frictional response of bovine articular cartilage from atomic force microscopy," *Journal of biomechanics*, vol. 37, pp. 1679-1687, 2004.
- [35] K. Costa and F. Yin, "Analysis of indentation: implications for measuring mechanical properties with atomic force microscopy," *Journal of biomechanical engineering*, vol. 121, pp. 462-471, 1999.
- [36] K. Hu, P. Radhakrishnan, R. V. Patel, and J. J. Mao, "Regional structural and viscoelastic properties of fibrocartilage upon dynamic nanoindentation of the articular condyle," *Journal of structural biology*, vol. 136, pp. 46-52, 2001.
- [37] S. Gupta, J. Lin, P. Ashby, and L. Pruitt, "A fiber reinforced poroelastic model of nanoindentation of porcine costal cartilage: a combined experimental and finite element approach," *Journal of the mechanical behavior of biomedical materials*, vol. 2, pp. 326-338, 2009.
- [38] M. J. A. Latif, N. H. Hashim, R. Ramlan, J. Mahmud, A. Jumahat, and M. R. A. Kadir, "The effects of surface curvature on cartilage behaviour in indentation test: a finite element study," *Procedia Engineering*, vol. 68, pp. 109-115, 2013.
- [39] N. H. Hashim, M. J. A. Latif, and Y. L. Jaafar, "The effects of contact area and surface curvature on biomechanical behavior of articular cartilage," in *Biomedical Engineering (ICoBE), 2015 2nd International Conference on*, 2015, pp. 1-4.
- [40] P. Cheng, W. Gu, J. Shen, A. Ghosh, A. Beskok, and Z. Hao, "Performance study of a PDMS-based microfluidic device for the detection of continuous distributed static and dynamic loads," *Journal of Micromechanics and Microengineering*, vol. 23, p. 085007, 2013.
- [41] W. Gu, P. Cheng, A. Ghosh, Y. Liao, B. Liao, A. Beskok, *et al.*, "A Polymer-based microfluidic resistive sensor for detecting distributed loads," in *ASME 2012 International Mechanical Engineering Congress and Exposition*, 2012, pp. 539-548.
- [42] W. Gu, P. Cheng, A. Ghosh, Y. Liao, B. Liao, A. Beskok, *et al.*, "Detection of distributed static and dynamic loads with electrolyte-enabled distributed transducers in a polymer-based microfluidic device," *Journal of Micromechanics and Microengineering*, vol. 23, p. 035015, 2013.
- [43] A. V. Jagtiani, J. Carletta, and J. Zhe, "An impedimetric approach for accurate particle sizing using a microfluidic Coulter counter," *Journal of Micromechanics and Microengineering*, vol. 21, p. 045036, 2011.
- [44] A. V. Jagtiani, J. Carletta, and J. Zhe, "A microfluidic multichannel resistive pulse sensor using frequency division multiplexing for high throughput counting of micro particles," *Journal of Micromechanics and Microengineering*, vol. 21, p. 065004, 2011.
- [45] Z. Zou, J. Kai, M. J. Rust, J. Han, and C. H. Ahn, "Functionalized nano interdigitated electrodes arrays on polymer with integrated microfluidics for direct bio-affinity sensing

- using impedimetric measurement," *Sensors and Actuators A: Physical*, vol. 136, pp. 518-526, 2007.
- [46] J. Shen, P. Cheng, W. Gu, and Z. Hao, "Stress relaxation measurement of viscoelastic materials using a polymer-based microfluidic device," *Sensors and Actuators A: Physical*, vol. 203, pp. 119-130, 2013.
- [47] X. Wang, J. A. Schoen, and M. E. Rentschler, "A quantitative comparison of soft tissue compressive viscoelastic model accuracy," *Journal of the mechanical behavior of biomedical materials*, vol. 20, pp. 126-136, 2013.
- [48] W. Gu, J. Shen, Y. Yang, and Z. Hao, "Dynamic characterization of a polymer-based microfluidic device for distributed-load detection," *Sensors and Actuators A: Physical*, vol. 222, pp. 102-113, 2015.
- [49] D.-H. Kim, J. Viventi, J. J. Amsden, J. Xiao, L. Vigeland, Y.-S. Kim, *et al.*, "Dissolvable films of silk fibroin for ultrathin, conformal bio-integrated electronics," *Nature materials*, vol. 9, p. 511, 2010.
- [50] D.-H. Kim, N. Lu, R. Ma, Y.-S. Kim, R.-H. Kim, S. Wang, *et al.*, "Epidermal electronics," *science*, vol. 333, pp. 838-843, 2011.
- [51] V. Fabrikant, "Flat punch of arbitrary shape on an elastic half-space," *International journal of engineering science*, vol. 24, pp. 1731-1740, 1986.
- [52] M. W. Stacey, J. Grubbs, A. Asmar, J. Pryor, H. Elsayed-Ali, W. Cao, *et al.*, "Decorin expression, straw-like structure, and differentiation of human costal cartilage," *Connective tissue research*, vol. 53, pp. 415-421, 2012.
- [53] C. Bougault, L. Cueru, J. Bariller, M. Malbouyres, A. Paumier, A. Aszodi, *et al.*, "Alteration of cartilage mechanical properties in absence of $\beta 1$ integrins revealed by rheometry and FRAP analyses," *Journal of biomechanics*, vol. 46, pp. 1633-1640, 2013.
- [54] M. Barker and B. Seedhom, "The relationship of the compressive modulus of articular cartilage with its deformation response to cyclic loading: does cartilage optimize its modulus so as to minimize the strains arising in it due to the prevalent loading regime?," *Rheumatology*, vol. 40, pp. 274-284, 2001.
- [55] A. D. Troyer and D. Leduc, "Effects of inflation on the coupling between the ribs and the lung in dogs," *The Journal of physiology*, vol. 555, pp. 481-488, 2004.
- [56] J. M. Cormier, J. D. Stitzel, S. M. Duma, and F. Matsuoka, "Regional variation in the structural response and geometrical properties of human ribs," in *Annual Proceedings/Association for the Advancement of Automotive Medicine*, 2005, p. 153.

APPENDICES A

LABVIEW PROGRAM FOR INSTRUMENT CONTROL AND DATA ACQUISITION

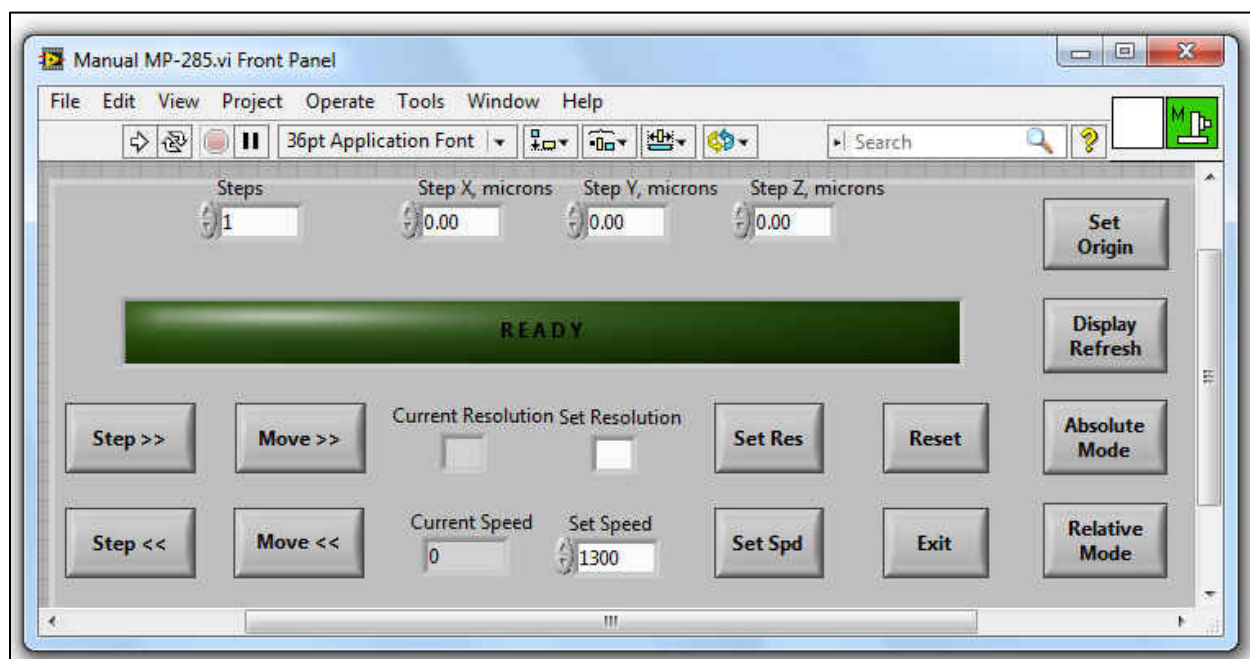


Figure A.1 LabVIEW front panel for manually control the micromanipular to apply x-direction, y-direction, z-direction displacement with a different ramp speed.

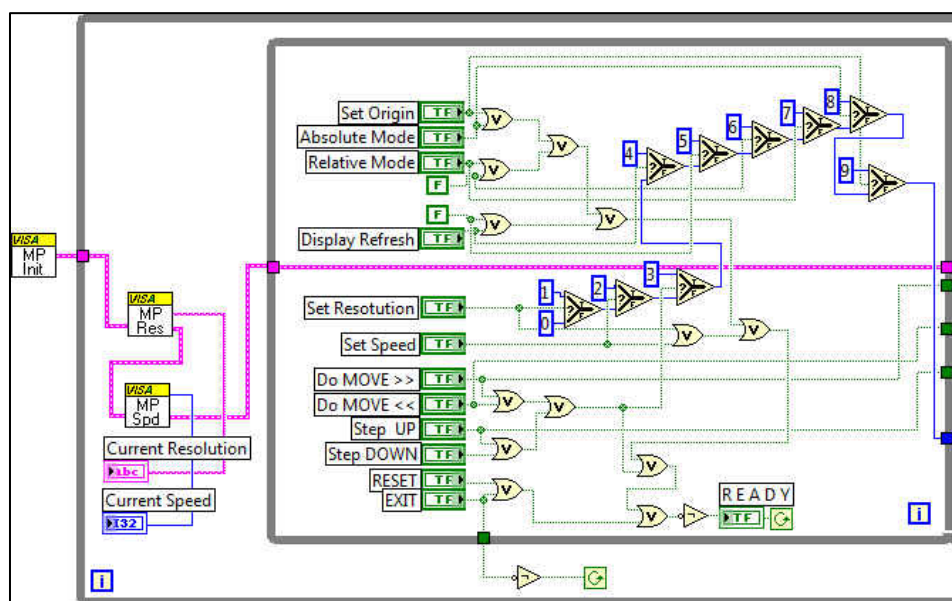


Figure A.2 (continue)

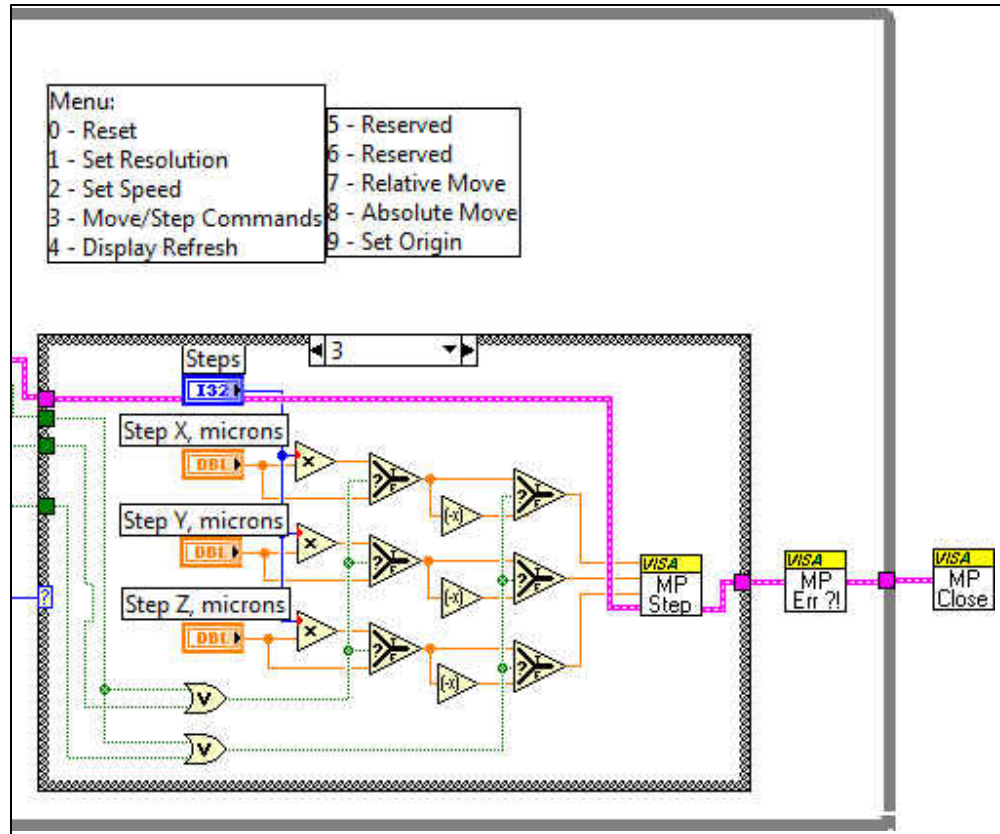
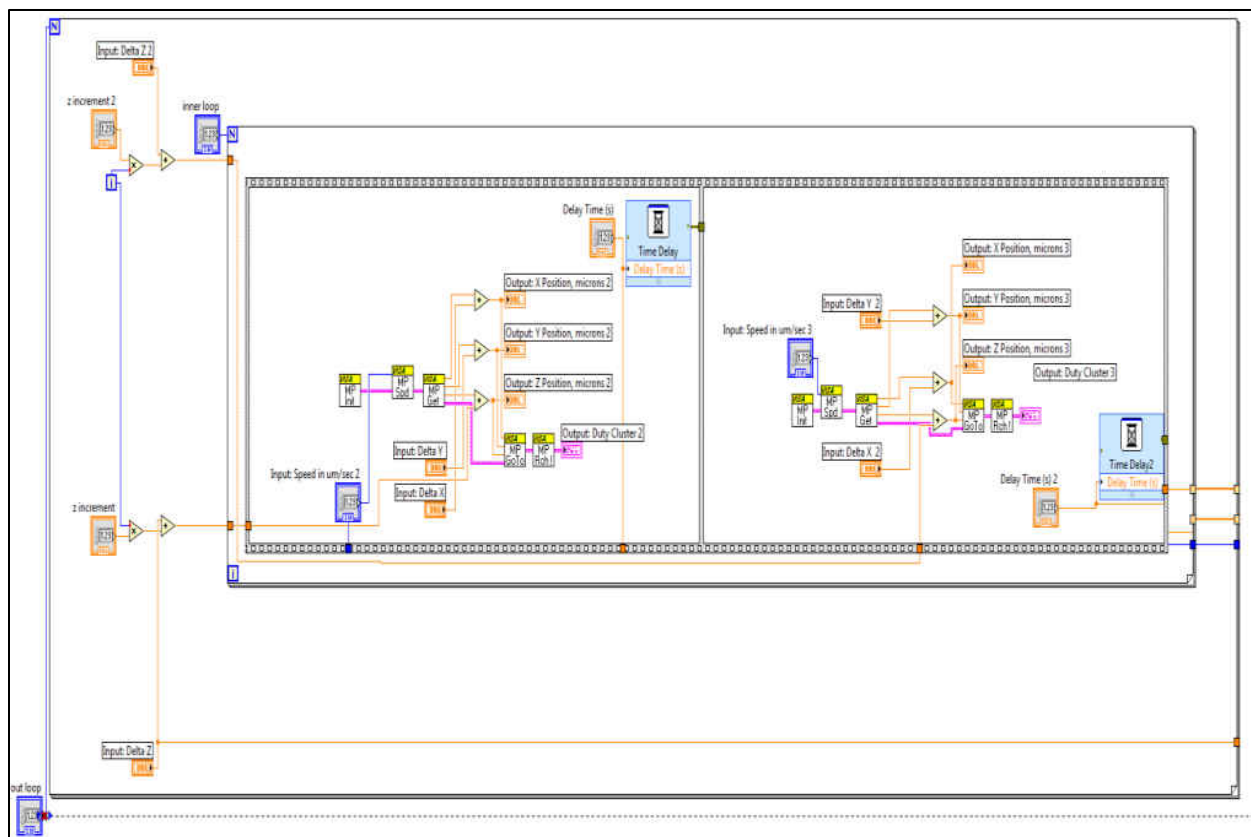
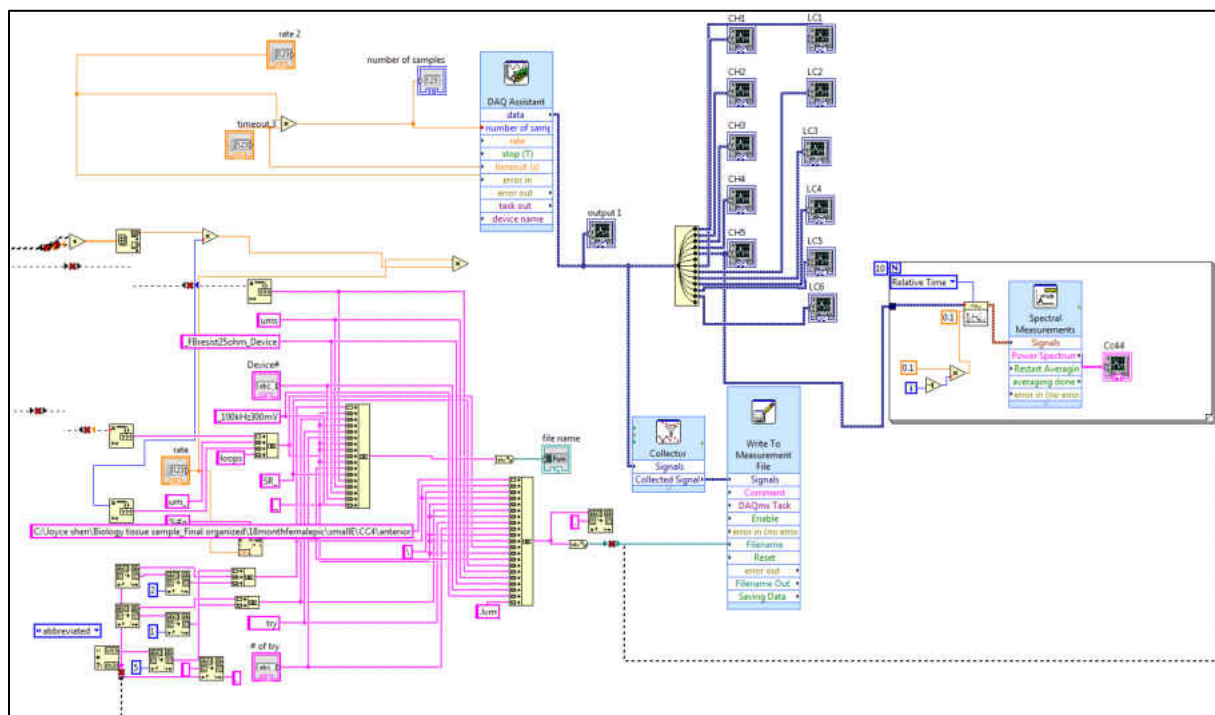


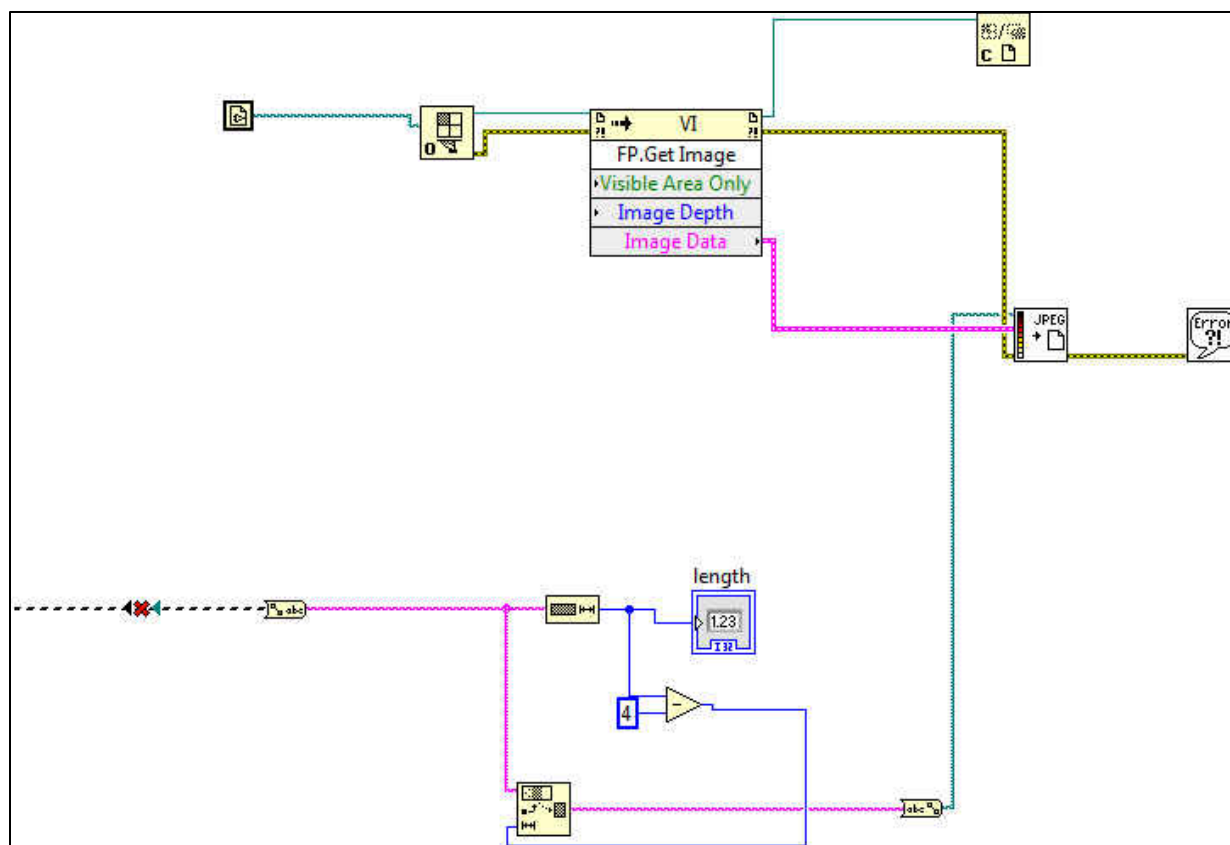
Figure A.2 LabVIEW block diagram for manually control the micromanipular to apply x-direction, y-direction, z-direction displacement with a different ramp speed.



(a)



(b)



(c)

Figure A.3 LabVIEW block diagram for (a) automatically control the micromanipular to apply x-direction, y-direction, z-direction displacement with a different ramp speed, (b) data collection, and (c) automatically screenshot the front panel after data collection.

APPENDICES B

MEASURED MECHANICAL PROPERTIES OF FIVE HUMAN PC CC

SEGMENTS AT FOUR ANATOMICAL SITES OF ALL MEASURED

LOCATIONS

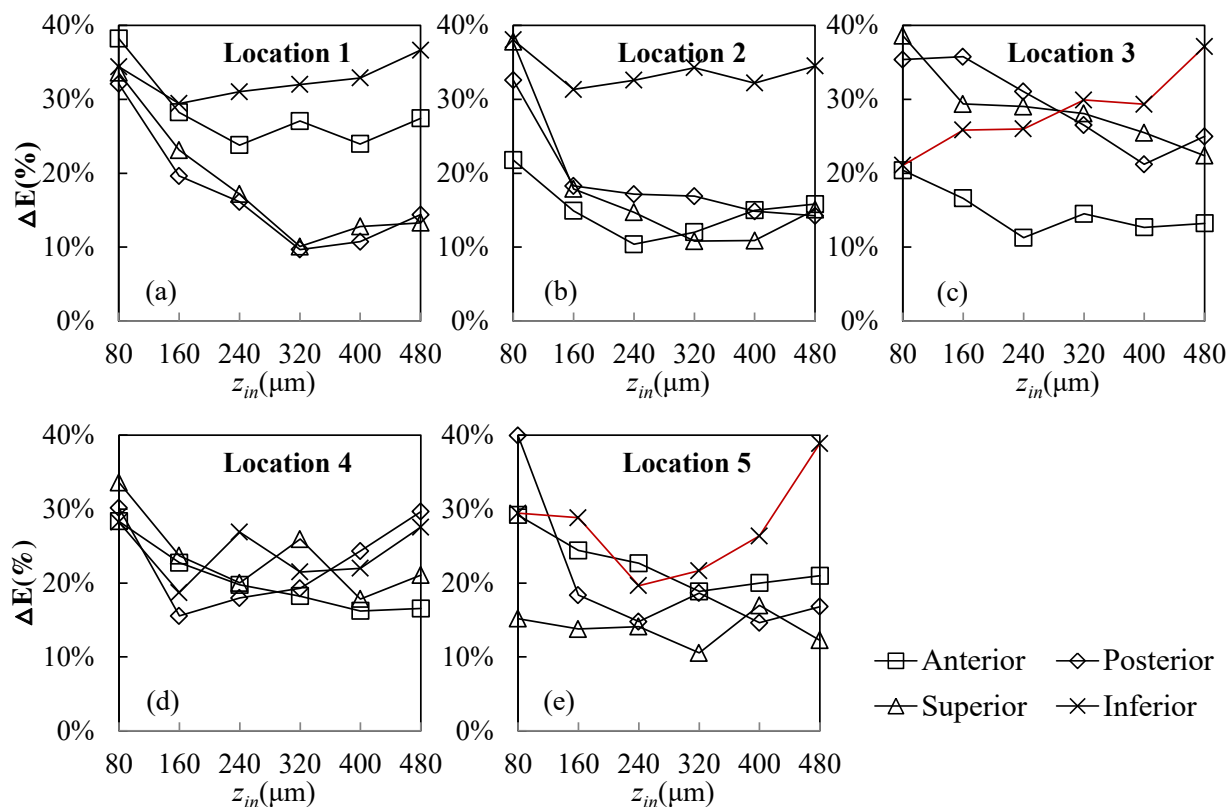


Figure B.1 Measured normalized relaxation as a function of indentation depth of CC #A at (a) location 1 (b) location 2 (c) location 3 (d) location 4 (e) location 5. (Red line: sensor was deformed before the measurements)

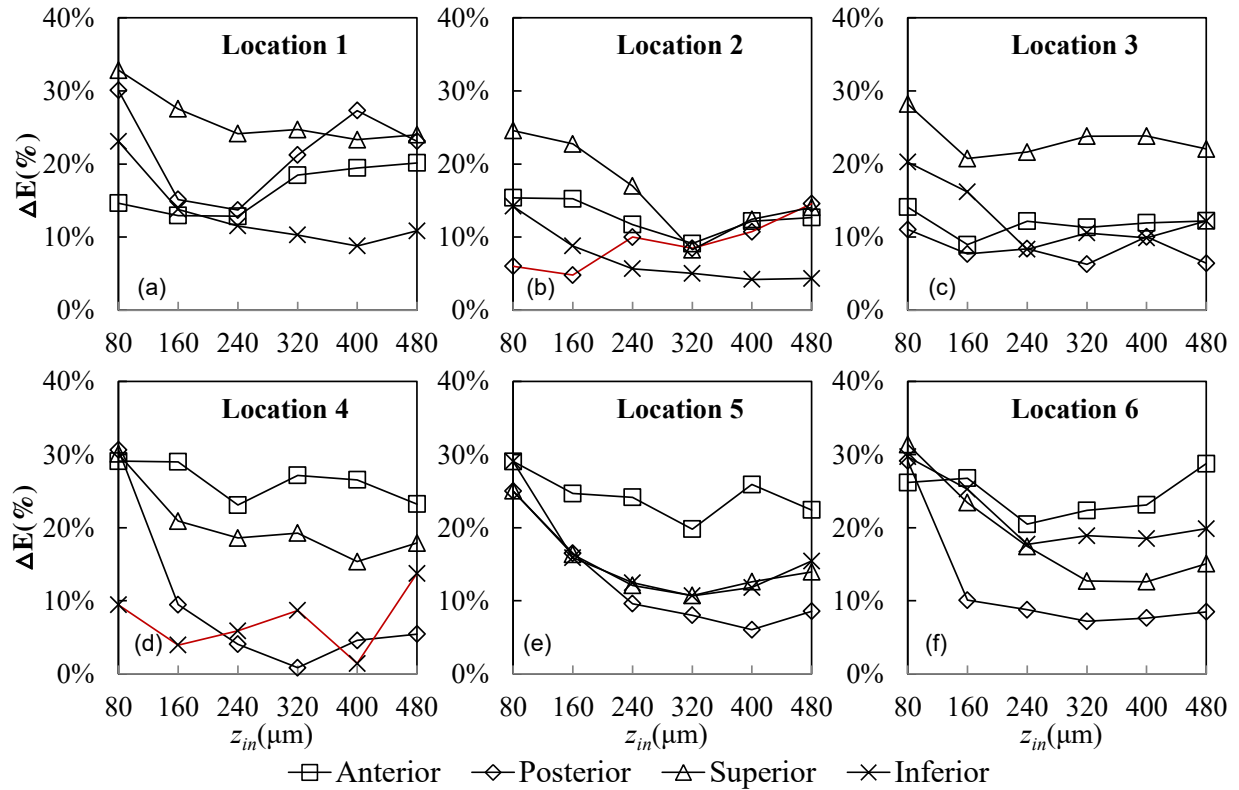


Figure B.2 Measured normalized relaxation as a function of indentation depth of CC #B at (a) location 1 (b) location 2 (c) location 3 (d) location 4 (e) location 5 (f) location 6. (Red line: sensor was deformed before the measurements)

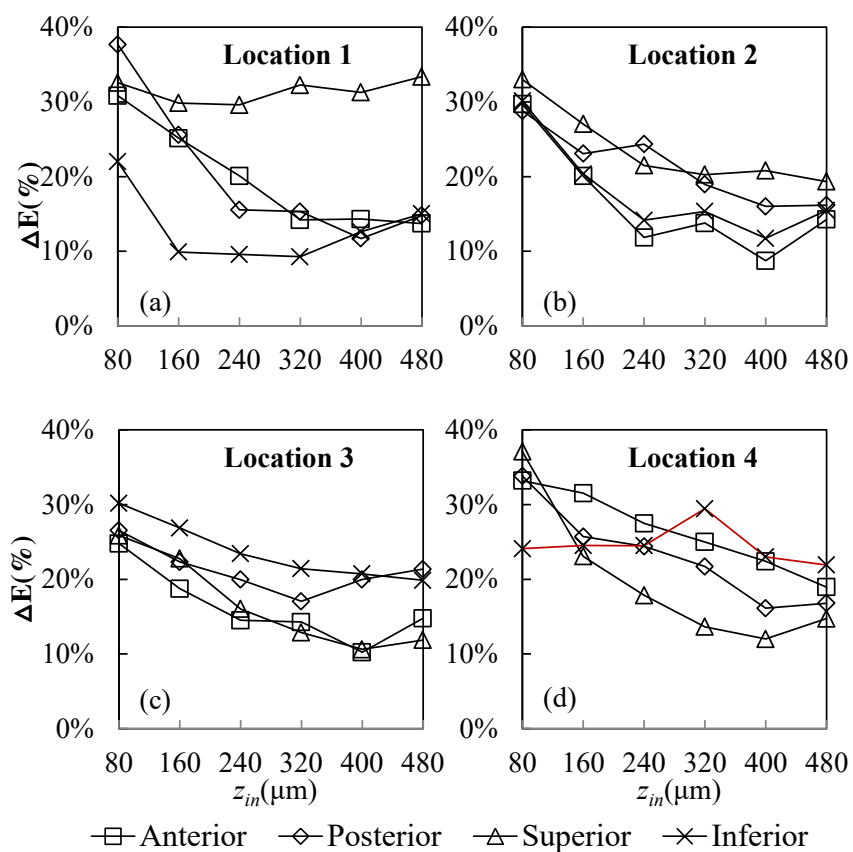


Figure B.3 Measured normalized relaxation as a function of indentation depth of CC #C at (a) location 1 (b) location 2 (c) location 3 (d) location 4. (Red line: sensor was deformed before the measurements)

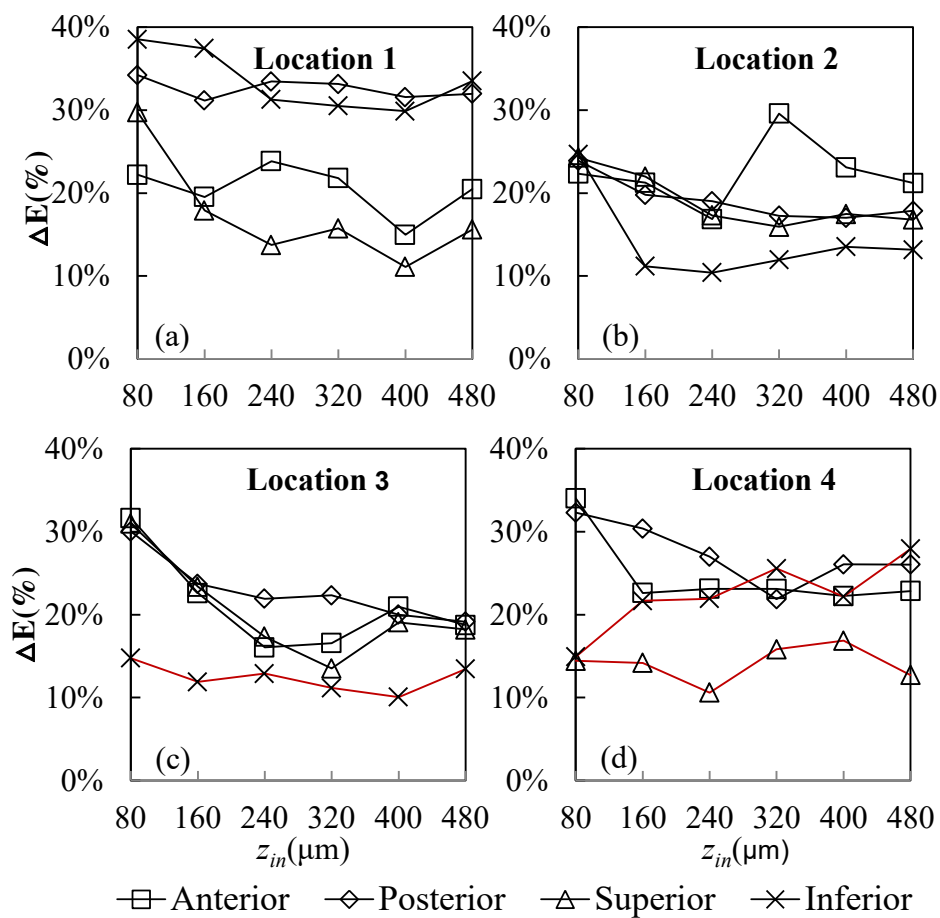


Figure B.4 Measured normalized relaxation as a function of indentation depth of CC #D at (a) location 1 (b) location 2 (c) location 3 (d) location 4. (Red line: sensor was deformed before the measurements)

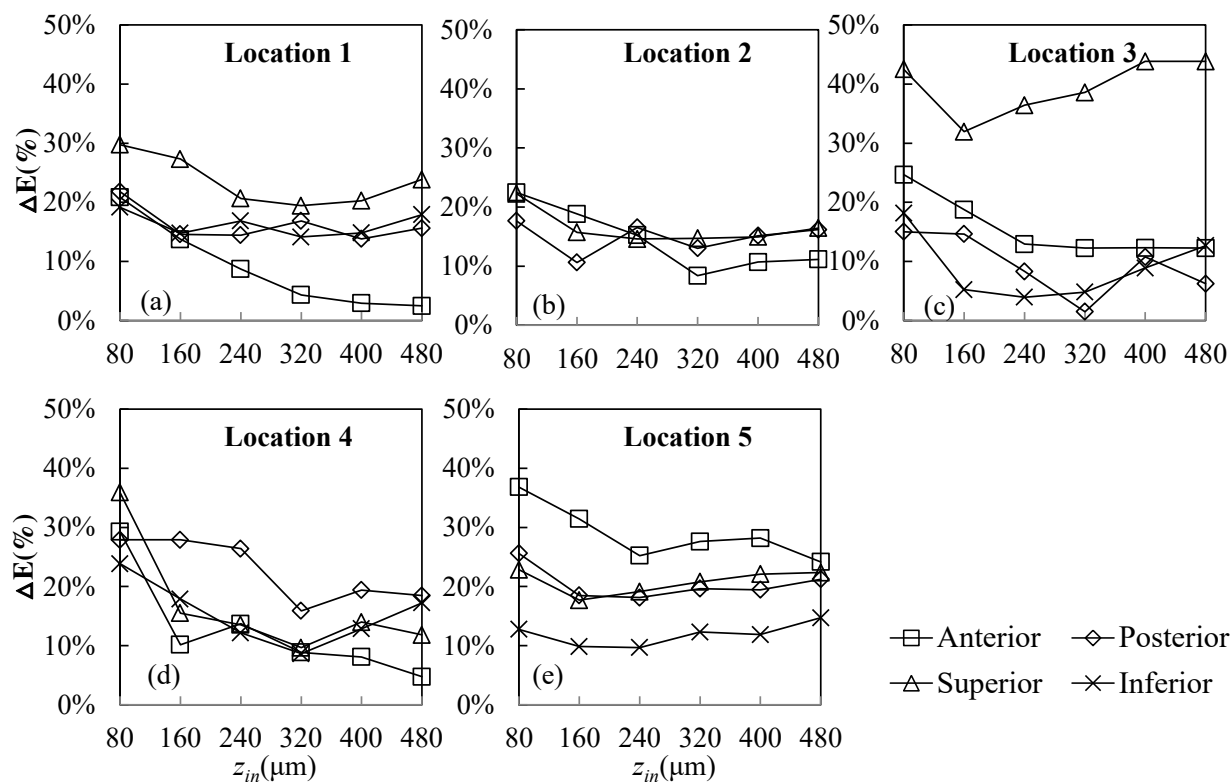


Figure B.5 Measured normalized relaxation as a function of indentation depth of CC #E at (a) location 1 (b) location 2 (c) location 3 (d) location 4 (e) location 5.

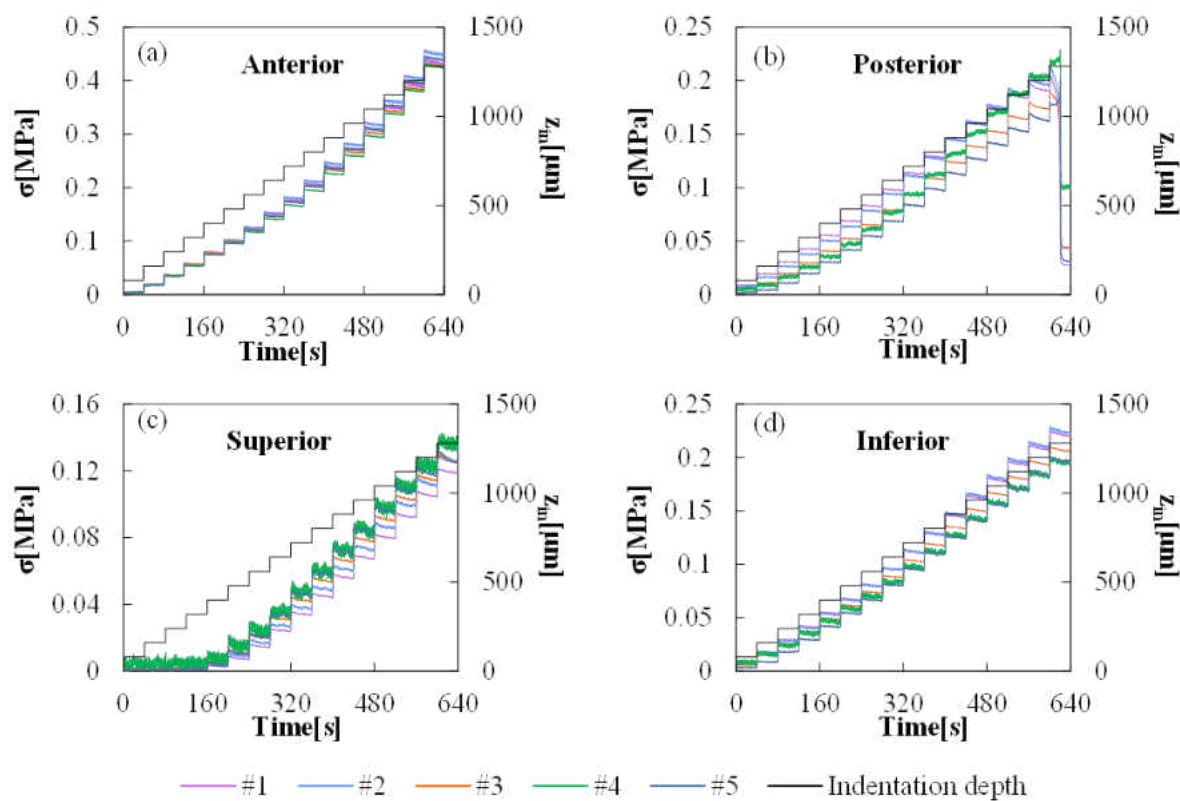


Figure B.6 Compressive stress as a function of time of CC # B at Location 3 (a) anterior surface (b) posterior surface (c) Superior border (d) inferior border.

Table B.1 Summary of the measured instant indentation modulus and normalized relaxation modulus and their measurement errors along the length of the CC samples at their anterior/posterior surfaces, superior/inferior borders and the average of the four positions (a) CC #A (b) CC #B (c) CC #C (d) CC #D (e) CC #E.

(a)

CC#A	Atomically sites	1	2	3	4	5
Instant indentation modulus (Mpa)	Anterior	284.5±12.9	462.2±32.2	469.2±29.4	261.7±21.9	237.9±17.6
	Posterior	182.4±12.5	178.5±6.5	160.2±9.9	209.3±4.5	134.2±4.9
	Superior	557.4±66.9	359.2±34.7	184.8±9.8	480.1±24.9	928.7±113.1
	Inferior	641.0±34.1	409.7±19.2	356.1±23.2	906.2±91.4	417.2±13.4
	Average	416.3±12.5	352.4±6.5	292.6±9.9	464.3±4.5	429.5±4.9
Normalized relaxation (%)	Anterior	25.6%	13.3%	12.9%	17.7%	20.6%
	Posterior	12.7%	15.8%	25.9%	22.8%	16.2%
	Superior	13.3%	12.9%	26.2%	21.2%	13.5%
	Inferior	33.1%	33.4%	25.7%	24.5%	24.1%
	Average	21.2%±8.6%	18.8%±8.5%	5.7%±3.5%	21.5%±2.5%	18.6%±4.1%

(b)

CC#B	Atomically sites	1	2	3	4	5	6
Instant indentation modulus (Mpa)	Anterior	480.8±10.0	914.4±102.7	607.7±50.2	254.1±11.2	306.7±17.2	333.6±14.3
	Posterior	279.8±7.7	377.6±10.3	219.7±17.2	596.3±70.9	250.7±16.1	395.8±26.2
	Superior	215.4±9.2	462.4±27.9	277.2±5.2	292.5±14.4	460.6±24.3	239.8±9.4
	Inferior	338.7±12.6	310.0±26.1	265.9±16.1	544.4±33.4	274.0±13.7	187.6±7.6
	Average	328.7±7.7	516.1±10.3	342.6±17.2	421.8±70.9	323.0±16.1	289.2±26.2
Normalized relaxation (%)	Anterior	17.7	11.4	11.9	25.0	23.1	23.7
	Posterior	21.3	9.1	7.8	3.7	8.0	8.0
	Superior	24.0	12.9	22.8	17.8	12.3	14.4
	Inferior	10.4	4.8	10.2	7.0	12.6	18.7
	Average	18.4±5.1	9.6%±3.1	13.2±5.8	13.4±8.5	14.0±5.5	16.2±5.8

(c)

CC#C	Atomically sites	1	2	3	4
Instant indentation modulus (Mpa)	Anterior	475.6±44.3	524.2±46.1	388.9±28.2	178.0±15.8
	Posterior	310.9±31.3	229.2±21.6	307.2±17.4	365.4±20.6
	Superior	278.7±4.5	399.9±22.4	358.3±26.9	339.2±33.0
	Inferior	846.2±73.1	559.5±51.3	359.5±15.7	312.5±16.1
	Average	477.9±31.3	428.2±21.6	353.5±28.2	298.8±20.6
Normalized relaxation (%)	Anterior	15.6	12.2	13.4	23.5
	Posterior	14.3	18.9	19.6	19.8
	Superior	31.6	20.5	12.8	14.6
	Inferior	11.6	14.2	21.4	24.6
	Average	18.3±7.8	16.4±3.4	16.8±3.7	20.6±3.9

(d)

CC#D	Atomically sites	1	2	3	4
Instant indentation modulus (Mpa)	Anterior	254.7±20.2	262.8±5.6	313.4±16.7	321.3±15.4
	Posterior	195.4±3.1	311.7±16.7	233.6±10.4	220.7±9.1
	Superior	487.1±33.6	404.4±26.7	283.0±15.2	1007.2±80.0
	Inferior	235.6±10.2	592.5±47.2	436.4±27.2	257.1±6.6
	Average	293.2±16.8	392.9±24.0	316.6±17.4	451.6±27.8
Normalized relaxation (%)	Anterior	20.3	22.7	18.1	22.8
	Posterior	32.5	17.8	20.8	25.2
	Superior	14.0	16.9	17.0	14.1
	Inferior	31.3	12.3	12.4	22.8
	Average	24.5±7.7	17.4±3.7	17.1±3.1	21.2±4.2

(e)

CC#E	Atomically sites	1	2	3	4	5
Instant indentation modulus (Mpa)	Anterior	416.7±25.2	608.4±45.1	221.4±13.0	204.0±10.9	177.2±4.5
	Posterior	268.5±8.3	303.7±11.3	299.1±20.1	171.0±5.9	134.2±6.3
	Superior	218.0±7.0	276.7±14.4	98.1±1.9	211.5±17.8	377.5±2.1
	Inferior	557.9±34.7	--	713.0±47.2	294.0±23.9	430.5±22.4
	Average	365.3±18.8	396.3±23.6	332.9±20.6	220.1±14.6	279.8±8.8
Normalized relaxation (%)	Anterior	4.6	11.4	12.4	8.9	26.3
	Posterior	15.2	15.2	6.7	20.1	19.6
	Superior	21.1	15.2	40.7	12.3	21.1
	Inferior	15.9	--	7.6	12.7	12.1
	Average	14.2±6.0	13.9±1.8	16.8±13.9	13.5±4.1	19.8±5.1

VITA

Jiayue Shen received the B.S. in mechanical engineering from the Zhejiang University in 2009, and M.S. from Lanzhou University of Technology in 2012, China. She is currently pursuing the Ph.D. degree in mechanical engineering at Old Dominion University. Her research interests focus on developing microfluidic sensors and microsystems for exploring different biomedical applications, such as diseased soft tissues diagnoses and inertial sensing; and analytical and experimental study of micromechanics critical for the performance of the microfluidic sensors and microsystems.